

1-1-2005

A numerical analysis of hemodynamics for arterial medical procedures

Ross Herbert Miller
Iowa State University

Follow this and additional works at: <https://lib.dr.iastate.edu/rtd>

Recommended Citation

Miller, Ross Herbert, "A numerical analysis of hemodynamics for arterial medical procedures" (2005).
Retrospective Theses and Dissertations. 19185.
<https://lib.dr.iastate.edu/rtd/19185>

This Thesis is brought to you for free and open access by the Iowa State University Capstones, Theses and
Dissertations at Iowa State University Digital Repository. It has been accepted for inclusion in Retrospective Theses
and Dissertations by an authorized administrator of Iowa State University Digital Repository. For more information,
please contact digirep@iastate.edu.

A numerical analysis of hemodynamics for arterial medical procedures

by

Ross Herbert Miller

A thesis submitted to the graduate faculty
in partial fulfillment of the requirements for the degree of
MASTER OF SCIENCE

Major: Mechanical Engineering

Program of Study Committee:
Francine Battaglia, Major Professor
Michael Olsen
John Tannehill

Iowa State University

Ames, Iowa

2005

Copyright © Ross Herbert Miller, 2005. All rights reserved.

Graduate College
Iowa State University

This is to certify that the master's thesis of
Ross Herbert Miller
has met the thesis requirements of Iowa State University

Signatures have been redacted for privacy

Dedicated to my grandpa, Herbert Haas, whose fate inspired me to work in this field. I miss him every day.

TABLE OF CONTENTS

LIST OF TABLES	viii
LIST OF FIGURES	ix
NOMENCLATURE	xiv
ACKNOWLEDGEMENTS	xviii
ABSTRACT	xx
CHAPTER 1. INTRODUCTION	1
1.1 Background Information	1
1.1.1 Intracranial carotid aneurysms	1
1.1.2 Bifurcation stenosis	3
1.2 Advantages of Numerical Simulations	4
1.3 Research Goals	5
CHAPTER 2. LITERATURE REVIEW	7
2.1 Blood Behavior and Hemodynamics Modeling	7
2.2 Intracranial Aneurysms	10
2.2.1 Medical findings	10
2.2.2 In vitro studies	11
2.2.3 CFD studies	12
2.3 Aortic Stent Reconstruction	13
2.3.1 Medical findings	13

2.3.2	In vitro studies	14
2.3.3	CFD studies	16
2.4	Summary	18
CHAPTER 3. NUMERICAL METHODOLOGIES		19
3.1	Governing Equations	19
3.2	Numerical Methodology	20
3.2.1	Spatial discretization	20
3.2.2	Temporal discretization	22
3.2.3	Evaluating gradients	23
3.2.4	Linearization	24
3.3	The Segregated Solver	24
3.3.1	Discretization of the momentum equation	25
3.3.2	Pressure interpolation	25
3.3.3	Discretization of the continuity equation	26
3.3.4	Pressure-velocity coupling	27
3.3.5	Time-dependent calculations	28
3.3.6	Residuals in the segregated solver	28
3.3.7	Solution loop	29
3.4	Mesh Generation	31
CHAPTER 4. SIMULATION OF THE INTRACRANIAL ANEURYSM		36
4.1	Boundary and Initial Conditions	36
4.2	Grid Resolution and Working Fluid	37
4.3	Computational Performance and Post-Processing	38
4.4	Simulation Results	39
4.4.1	Constant inlet velocity	39
4.4.2	Pump flow versus physiological flow	40

4.4.3	Summary of aneurysm results and conclusions	47
CHAPTER 5. SIMULATIONS OF STENT RECONSTRUCTION . .		49
5.1	Boundary and Initial Conditions	49
5.2	Grid Resolution and Working Fluid	54
5.3	Computational Performance and Post-Processing	55
5.4	Simulation Results	56
5.4.1	Unstented simulation	57
5.4.2	Effects of stent presence	60
5.4.3	Effects of stent mismatch	70
5.4.4	Effects of low-permeability stents	74
CHAPTER 6. CONCLUSIONS, IMPACT, LIMITATIONS, AND FU-		
TURE WORK		78
6.1	Conclusions and Impact	79
6.2	Limitations and Future Work	80
APPENDIX A. THE ALGEBRAIC MULTIGRID		83
A.1	The Basic Multigrid Concept	83
A.2	Restriction and Prolongation	84
A.3	Unstructured Multigrid	84
A.3.1	AMG restriction and prolongation operators	85
A.3.2	AMG coarse level operator	86
A.3.3	Residual reduction rate criteria	86
A.3.4	Termination criteria	87
APPENDIX B. MICROPIV EXPERIMENTS OF ANEURYSM FLOW		88
B.1	Introduction to MicroPIV	88
B.2	Experimental Setup	89
B.2.1	Circulatory system	89

B.2.2 Working fluid	90
B.2.3 MicroPIV camera system	90
REFERENCES	93

LIST OF TABLES

Table 4.1	Mesh convergence studies for coarse (3), medium (2), and fine (1) aneurysm meshes. Superscript notation refers to a comparison between two meshes. ϕ_A = pressure at $(x, y, z) = (10.4, 2.4, 0)$ mm. ϕ_B = u -velocity at $(x, y, z) = (17.0, 0, 0)$ mm.	37
Table 5.1	Mesh convergence studies for coarse (3), medium (2), and fine (1) bifurcation meshes. Superscript notation refers to a comparison between two meshes. ϕ_A = velocity magnitude at $(x, y, z) = (0, -30.0, 0)$ mm. ϕ_B = velocity magnitude at $(x, y, z) = (15.6, -59.6, 0)$ mm.	55
Table 5.2	Summary of peak streamwise vorticity and changes in peak streamwise vorticity for unstented, one-stent, and two-stent simulations in the “thru stent inlet” plane at 30° . Percent changes are in relation to the unstented case.	63
Table 5.3	Summary of peak WSS, spanwise vorticity, streamwise vorticity, and changes in these variables for unstented, one-stent, two-stent, and low-permeability simulations at a pulse phase of 30° and in the stent inlet plane, stent outlet plane, and the $x-y$ centerplane. Percent changes are in relation to the unstented case.	77

LIST OF FIGURES

Figure 1.1	Sketch of an artery with an aneurysm. Arrows indicate direction of flow.	2
Figure 1.2	Sketch of an aort-iliac bifurcation. Arrows indicate direction of flow.	3
Figure 2.1	A generic profile of velocity versus pulse phase for arterial blood flow.	8
Figure 3.1	Control volume illustrating discretization and transport.	21
Figure 3.2	The FLUENT segregated solver solution loop.	30
Figure 3.3	Geometry for the carotid artery and aneurysm.	31
Figure 3.4	Mesh for the aneurysm geometry at the $x - y$ centerplane ($z = 0$).	32
Figure 3.5	Geometry for the unstented aorta-iliac bifuraction.	33
Figure 3.6	Wireframe of the stented aorta-iliac bifuraction.	34
Figure 3.7	Mesh for the stented bifurcation geometry at the $x - y$ centerplane ($z = 0$).	34
Figure 4.1	Inlet boundary conditions used in the numerical simulations for the pump flow (dashed line) and the physiological flow (solid line) conditions.	39

Figure 4.2	Velocity vectors superimposed on spanwise vorticity contours (1/s) for aneurysm simulations using the “pump” (left) and “physiological” (right) inlet waveforms at pulse phases of (a) 120° and (b) 130°.	40
Figure 4.3	Velocity vectors superimposed on spanwise vorticity contours (1/s) for simulations (left frames) and microPIV experiments (right frames) at pulse phases of (a) 40°, (b) 60°, (c) 240°, and (d) 360°.	43
Figure 4.4	u -velocity profiles for simulations and experiments downstream of, at the center of, and upstream of the aneurysm at pulse phases of (a) 40°, (b) 60°, (c) 240°, and (d) 360°.	44
Figure 4.5	Contours of wall shear stress (N/m ²) near the distal aneurysm sac wall at pulse phases of (a) 40°, (b) 60°, (c) 240°, and (d) 360°.	47
Figure 4.6	Pressure contours (Pa) at pulse phases of (a) 40°, (b) 60°, (c) 240°, and (d) 360°.	48
Figure 4.7	(a) Pressure profiles and (b) v -velocity profiles across the aneurysm neck at pulse phases of 40°, 60°, 240°, and 360°.	48
Figure 5.1	Inlet boundary condition used in the numerical simulations of blood flow in the bifurcation.	50
Figure 5.2	Profiles of normal velocity across the left iliac diameter at $z = 0$ for the 30 mm (short) and 300 mm (long) iliac length simulations.	52
Figure 5.3	Time-averaged contours of velocity (m/s) normal to the $x - y$ centerplane in the full 3D bifurcation model.	52
Figure 5.4	Geometry for the aorta-iliac bifurcation with symmetry in the $x - y$ centerplane. Created using GAMBIT.	53
Figure 5.5	Sketch of the stent reconstruction geometry with five planes of interest labeled.	57

Figure 5.6	Peak values for (a) WSS and (b) spanwise vorticity, plotted versus the pulse phase. Peak values occurred along the artery wall near the bifurcation.	58
Figure 5.7	Contours of (a) WSS (N/m^2) and (b) spanwise vorticity (s^{-1}) near the bifurcation wall of the left iliac for a pulse phase of 30°	59
Figure 5.8	Sketches of the $x - y$ centerplanes for (a) no stents, (b) one stent, and (c) two stents.	59
Figure 5.9	Peak WSS at four phase locations for the unstented, one-stent, and two-stent cases. Planes shown are (a) stent inlet, (b) stent outlet, (c) thru stent inlet, (d) thru stent base, (e) thru stent outlet, and (f) $x - y$ centerplane.	61
Figure 5.10	Contours of WSS (N/m^2) in the $x - y$ centerplane near the outer right iliac wall for (a) no stents and (b) two stents.	62
Figure 5.11	Peak negative streamwise vorticity in six planes of interest at four important phase locations for the unstented, one-stent, and two-stent simulations. Planes shown are (a) stent inlet, (b) stent outlet, (c) thru stent inlet, (d) thru stent base, (e) thru stent outlet, and (f) $x - y$ centerplane.	64
Figure 5.12	Peak positive streamwise vorticity in six planes of interest at four important phase locations for the unstented, one-stent, and two-stent simulations. Planes shown are (a) stent inlet, (b) stent outlet, (c) thru stent inlet, (d) thru stent base, (e) thru stent outlet, and (f) $x - y$ centerplane.	65
Figure 5.13	Contours of streamwise vorticity (s^{-1}) in the “thru stent inlets” plane at a pulse phase of 30° for (a) unstented, (b) one-stent, and (c) two-stent simulations.	66

Figure 5.14	Contours of streamwise vorticity (s^{-1}) in the plane of the stent inlets at a pulse phase of 30° for (a) unstented, (b) one-stent, and (c) two-stent simulations.	67
Figure 5.15	Contours of streamwise vorticity (s^{-1}) in the plane of a stent outlet at a pulse phase of 30° for (a) unstented, (b) one-stent, and (c) two-stent simulations.	68
Figure 5.16	Velocity streamlines near the bifurcation wall for (a) unstented, (b) one-stent, and (c) two-stent simulations.	69
Figure 5.17	Sketches of the $x - y$ centerplanes for (a) small mismatch and (b) large mismatch.	70
Figure 5.18	Contours of WSS (N/m^2) in the $x - y$ centerplane near the right bifurcation wall, at 30° , for (a) perfect alignment, (b) small mismatch, and (c) large mis-match. All three simulations featured two stents.	71
Figure 5.19	Contours of WSS (N/m^2) in the stent inlet plane ($y = -30.5$ mm) at 30° , for (a) no mis-match, (b) small mis-match, and (c) large mis-match.	72
Figure 5.20	Contours of streamwise vorticity (s^{-1}) in the stent inlet plane ($y = -30.5$ mm) at 30° , for (a) no mis-match, (b) small mis-match, and (c) large mis-match.	73
Figure 5.21	Velocity streamlines near the bifurcation wall for (a) two stents, $\alpha = 10^{-8} m^2$, and (b) two stents, $\alpha = 10^{-9} m^2$	75
Figure 5.22	Contours of spanwise vorticity (s^{-1}) in the $x - y$ centerplane near the left bifurcation wall for (a) two stents, $\alpha = 10^{-8} m^2$, and (b) two stents, $\alpha = 10^{-9} m^2$. Pulse phase = 30°	76

Figure B.1	Schematic of the <i>in vitro</i> circulatory system for the microPIV experiments.	89
Figure B.2	Experimental test section and aneurysm for the microPIV experiments.	90
Figure B.3	Schematic of the laser and optics for the microPIV system. . . .	91

NOMENCLATURE

A	multigrid fine level operator
A^H	multigrid coarse level operator
\vec{A}	surface area vector
B	volume fraction of stent surface material
D	diameter
$F(\phi)$	spatial discretization function
\vec{F}	force vector
I	identity matrix
J	mass flux
M	magnification
N	number
P	multigrid prolongation operator
R	residual; in multigrid, restriction operator
Re	Reynolds number
S	source term
V	cell volume
Z_{corr}	depth of correlation
a	weighting factor; stent fiber diameter in boundary conditions
c	continuity
$c0, c1$	cell centers

d	multigrid defect
d^{new}	multigrid defect when transferring from coarse to fine level
d_f	coefficient in the momentum-weighted averaging formulation
d_p	tracer particle diameter
$f^\#$	focal number of the microPIV lens
\vec{g}	gravitational acceleration
\hat{i}	unit vector in the normal direction
n	discretized time level
p	pressure
\vec{r}	vector direction from the cell centroid to the face centroid
\vec{s}	vector direction from the upstream cell centroid to the face centroid
t	time
u	streamwise velocity component
v	velocity magnitude; in some cases cross-stream velocity component
\vec{v}	velocity vector
w	spanwise velocity component
x	streamwise direction
y	cross-stream direction
z	spanwise direction

Greek Symbols

Γ	diffusion
α	medium permeability; in multigrid, termination criterion
α_p	under-relaxation factor for pressure
β	multigrid relaxation coefficient
ϵ	depth of correlation constant

λ	wavelength of emitted tracer particle light
μ	dynamic viscosity
ρ	density
$\bar{\bar{\tau}}$	stress tensor
ϕ	scalar transport variable
ψ	multigrid corrector
ω	vorticity

Superscripts

*	guessed value
'	corrected value
<i>i</i>	initial time level
<i>T</i>	transpose

Subscripts

<i>CD</i>	central difference
<i>P</i>	a computational cell
<i>UP</i>	upwind
<i>c</i>	coarse level of the multigrid
<i>f</i>	cell face
<i>m</i>	mass
<i>n</i>	normal
<i>nb</i>	neighbor cells
<i>scaled</i>	scaled, for residuals

Other Symbols

Δ	change or displacement
∇	gradient operator
$\nabla \cdot$	divergence operator

Abbreviations

AC	additive correction
AMG	algebraic multigrid
CCW	counter-clockwise
CFD	computational fluid dynamics
CMS	compliance matching stent
CW	clockwise
ESO	endovascular surgical occlusion
GCI	grid convergence index
HPC	high-performance computing
IT	intimal thickening
MRA	magnetic resonance angiography
MRI	magnetic resonance imaging
PISO	pressure-implicit with splitting of operators
PIV	particle image velocimetry
PRESTO	pressure staggering option
SIMPLE	semi-implicit method for pressure-linked equations
WSS	wall shear stress

ACKNOWLEDGEMENTS

A famous old sporting adage states that “there’s no *I* in *TEAM*.” While there is an *I* in *THESIS*, this particular thesis would not have been possible without the help and support of many others. I can’t imagine thanking anyone first besides my inexhaustible major professor, Dr. Francine Battaglia, for taking on a student wasn’t quite sure what CFD stood for when he began his Master’s research. Her invaluable guidance and supervision constantly inspired me to do my best work, and her financial support was greatly appreciated. I am indebted to her always for the opportunities she provided me.

I would like to sincerely thank my parents, Jim and Debby, and my brother, Sam, for their boundless patience, support, and encouragement during my pursuit of higher education. Their love means the world to me.

I wish to thank Dr. Michael Olsen for serving on my advising committee and for his contributions to my research, and Dr. John Tannehill for serving on my committee, teaching me CFD to begin with, and contributing his input to my research. Their guidance and committee service were greatly appreciated.

I would also like to gratefully acknowledge Dr. James Coyle and the High Performance Computing Center at Iowa State University, as well as John Dickerson and Iowa State’s College-Level Unified Environment Network, for their provision of computing resources and technical support, without which this research would not have been possible.

Last but certainly not least, a very heartfelt thank-you goes out to my wonderful friends and colleagues in the Computational Fluid Dynamics Center: Andrew, Anup, Deify, Farshid, Ian, Jin, Nan, Madhu, Ying, Rahul, Sergiy, George, Jay, Joon, Mao,

Wenny, Wen, and Zhaohui for their friendship, support, and encouragement. Their companionship will be dearly missed. Thank you for making my stay in Ames a memorable one.

ABSTRACT

The present research consisted of two investigations using computational fluid dynamics (CFD) to simulate the hemodynamics of arterial systems. In the first investigation, numerical simulations of flow in an intracranial side-wall aneurysm were performed. The resulting velocity vectors and vorticity contours compared very favorably with data from microPIV experiments on an equivalently-sized aneurysm geometry. However, there was evidence to suggest that the elastic walls in the microPIV experiments (which were not modeled in the numerical simulations) played a role in sustaining primary vortex development within the aneurysm, particularly during pulse phases of high velocity. Successful reproduction of the experimental velocity field allowed the simulations to be used to quantify other important variables, such as wall shear and pressure, within the aneurysm. A region of high wall shear stress oscillation and large pressure gradients were found near the distal aneurysm neck.

In the second investigation, stent reconstruction of an aorta-iliac bifurcation was simulated using CFD. The effects of stent presence, alignment, and permeability were investigated. Stent presence lowered wall shear stress along stented artery walls and elevated streamwise vorticity near the stent inlets and outlets. When reconstruction featured two mis-aligned stents, wall shear stress decreased and streamwise vorticity increased, proportional to the degree of mis-alignment. Low permeability stents magnified the flow abnormalities seen in the stent presence simulations. The modeling technique, representing stents by a porous jump boundary condition, is novel and its results agree well with the cited literature on experimental and numerical stent research.

CHAPTER 1 INTRODUCTION

1.1 Background Information

The majority of deaths in developed countries worldwide result from cardiovascular disease. It is the single leading cause of death in the United States, killing over 900,000 people in 2002, a number that accounted for 38% of all deaths that year. In the same year, an estimated 70,100,000 Americans suffered from either high blood pressure, coronary heart disease or stroke [1].

Cardiovascular disease is often caused by irregular blood flow due to the development of abnormalities in the circulatory system. Two dangerous types of abnormalities are stenosis of the aorta-iliac bifurcation and intracranial aneurysms on carotid arteries. These two abnormalities are introduced below.

1.1.1 Intracranial carotid aneurysms

Cardiovascular disease can cause a stroke when the brain does not receive an adequate supply of oxygenated blood. Stroke today is one of the leading causes of death and long-term disability in the United States. A common cause of stroke mortality is subarachnoid hemorrhaging due to the rupture of a small balloon-like sac, known as an aneurysm, that forms on the cerebral arteries at the base of the brain. Figure 1.1 shows a sketch of a typical aneurysm.

One surgical technique to prevent subarachnoid hemorrhaging is endovascular surgical occlusion (ESO) in which platinum coils placed within the aneurysm sac occlude

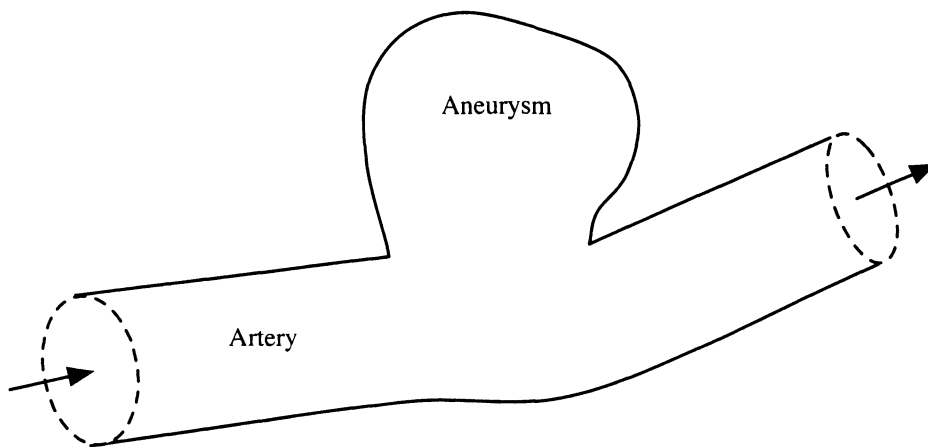


Figure 1.1 Sketch of an artery with an aneurysm. Arrows indicate direction of flow.

blood flow into the region. In the ESO procedure, the surgeon makes a small incision in the patient's groin and guides a small catheter through an artery into the blood vessel containing the aneurysm. The catheter is carefully guided into the aneurysm sac where the coils detach. The coils conform to the sac's shape and pack it tightly to cut off blood flow and prevent rupture. ESO is considerably less invasive than other techniques and has been used successfully in recent years. However achieving complete occlusion can be difficult and the procedure requires considerable care and skill to avoid rupturing the aneurysm sac [11, 12].

Another technique for preventing aneurysm rupture is the application of stent grafts, in which a stent inserted into the diseased artery crosses over the aneurysm neck and occludes blood flow into the sac. The difficulty lies in creating stents with fiber arrangements that are dense enough to prevent flow into the sac yet still porous enough to allow the exchange of nutrients between the artery wall and the blood. Stent treatment of aneurysms has been safe and effective in recent years [13, 14] but long-term patency and success rates have yet to be determined.

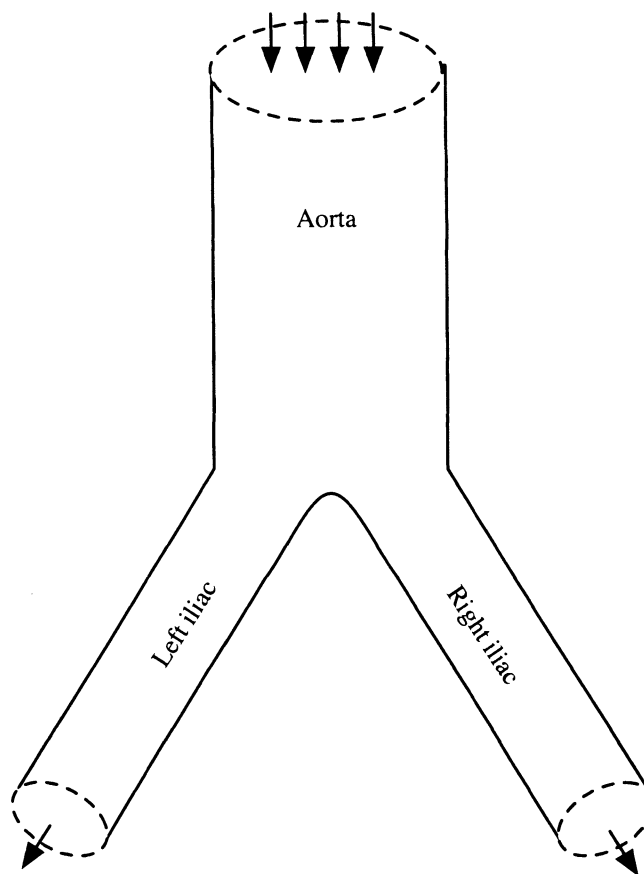


Figure 1.2 Sketch of an aort-iliac bifurcation. Arrows indicate direction of flow.

1.1.2 Bifurcation stenosis

The aorta is the largest artery in the human body. It carries oxygenated blood away from the heart to other organs. Near waist level, the aorta bifurcates into two iliac arteries, the major arteries of the legs. Figure 1.2 shows a sketch of a typical aort-iliac bifurcation. Stenosis occurs when plaque builds up along the artery walls causing a narrowing of the iliacs near the bifurcation. Severe stenosis is a serious medical condition that can be fatal when it results in inadequate blood supply to the heart or brain.

The three most frequent surgical treatments for severe stenosis are bypass grafting, angioplasty, and stent reconstruction. Bypass grafting circumvents the stenosed artery section by transplanting a healthy artery. The process is highly invasive and requires

considerable recovery and hospital care. Angioplasty and stent reconstruction are minimally invasive and are often coupled together to treat stenosis. Stents are small circular tubes made of multiple intersecting metallic fibers. Surgeons collapse a stent and fit it around a small deflated balloon attached to a catheter. Upon insertion into the diseased artery, the catheter inflates and deflates the balloon, stretches the artery wall, and clears it of blockage. During inflation the stent is pressed firmly against the artery wall where it remains as a scaffold to reinforce the weakened artery after the catheter is removed.

Before stenting became popular in the last decade, the balloon expansion angioplasty procedure was used alone. While stenting is currently considered an effective method with acceptable long-term patency rates, even in cases of complete artery occlusion [2, 3, 4], some debate still exists over the ability of stents to reduce rates of restenosis (the re-narrowing of the treated artery within a few months of surgery) versus angioplasty without stenting. While studies on the restenosis-reducing capabilities of stents have been promising [5, 6, 7, 8], stent reconstruction is still a complicated and expensive procedure, and restenosis rates remain as high as 30-40% in patients of particular subgroups [9, 10].

1.2 Advantages of Numerical Simulations

In order for surgical treatments such as bifurcation stenting, stent grafting, and ESO to become more reliable in the long-term, a more complete understanding of blood flow phenomena (commonly termed hemodynamics) within stented bifurcations and intracranial aneurysms is required. The fluid mechanics of blood flow in the human cardiovascular system can be difficult to completely capture *in vitro* or *in vivo* due to restrictively small vessel sizes, difficulties in measuring flow phenomena near vessel walls, and the cost and precision needed to accurately reproduce the system with an *in vitro* model. The term *in vitro* refers to an experiment conducted in artificial environment constructed to

represent the cardiovascular system. *In vivo* refers to an experiment conducted on an actual human cardiovascular system.

Unlike many *in vivo* and *in vitro* methods, numerical simulations can be relatively inexpensive to conduct and allow for detailed observations of system locations where experiments may have difficulty gathering accurate data. Computational fluid dynamics (CFD) allows for the modeling of flow phenomena based on the governing equations of fluid mechanics. Progress in modeling techniques and computational power have provided a promising role for CFD in observing the complex flow regimes in biological systems. CFD simulations also provide a means of comparing and validating experimental work without the often difficult process of observing a real physiological system. Additional knowledge will allow surgeons and medical professionals to predict the responses of individual patients to particular treatments and lead to more individually-optimized treatments, higher long-term success rates, fewer post-operative complications, and lower medical costs.

1.3 Research Goals

The primary goal of this research is to demonstrate the capability of CFD simulations to represent blood flow in the cardiovascular system and acquire detailed information about flow patterns within the system. This goal will be accomplished principally by a comparison between the numerical results from the intracranial aneurysm simulations and the flow fields in an *in vitro* experimental model of equivalent geometry. In addition, simulations of the stented bifurcation will demonstrate the ability to predict flow phenomena seen in the literature on *in vitro* and *in vivo* research.

A secondary goal is to demonstrate the success of the computational modeling technique used to represent the stent geometries, which is unique in comparison to other numerical simulations of flow in stented arteries, as a valid method of capturing the

hemodynamics in such a system. This goal will be accomplished by comparing the flow patterns from stented bifurcation simulations to patterns reported in literature on *in vivo*, *in vitro*, and other numerical models.

Finally, it is desired to conclude on an optimal stent configuration that will lead to reduced restenosis rates. This goal will be accomplished by investigating changes in flow phenomena introduced by the presence of stents of various configurations and permeability within the bifurcation system.

CHAPTER 2 LITERATURE REVIEW

Blood flow in arteries is a complex phenomena dominated by unsteady flow. The cardiovascular system transports nutrients and wastes while the heart delivers blood throughout the body with a network of veins and arteries. Blood flow under normal and diseased conditions is an extensive field of study with many opportunities for problem solving in engineering disciplines.

Research on the fluid dynamics of blood flow, or hemodynamics, has focused on qualitatively describing flow properties using *in vivo* and *in vitro* measurements, as well as numerical simulations. When considering the presence of stents or aneurysms, experimental models have focused on qualitatively observing regions of abnormal flow in comparison to healthy systems. Numerical models have focused on detailed analyses of flow patterns very near stented walls and within aneurysm sacs. This chapter presents relevant research related to blood flow, aneurysms, and stent reconstruction.

2.1 Blood Behavior and Hemodynamics Modeling

Before attempting to simulate blood flow, it is important to understand the composition and behavior of blood within the body. Blood is a complex mixture of plasma, platelets, and cells. Red blood cells typically comprise about 40% of blood by volume. Red blood cells are small, semisolid particles that increase the viscosity of blood from one centipoise (water viscosity) to approximately four centipoise, however the viscosity of blood varies between one and six centipoise depending on the size of the artery

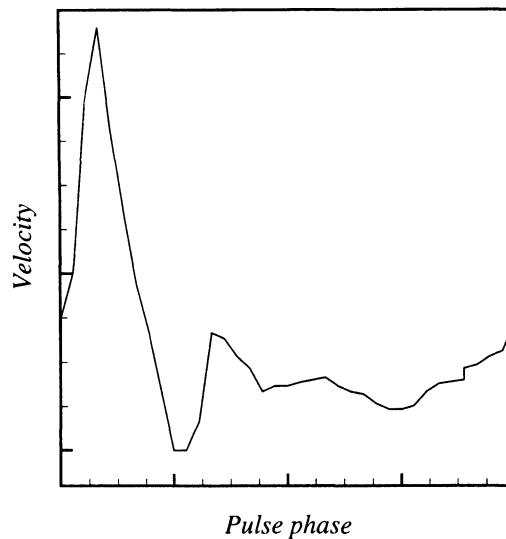


Figure 2.1 A generic profile of velocity versus pulse phase for arterial blood flow.

through which the flow travels [15]. Consequently, blood exhibits non-Newtonian behavior, especially in small arteries where the suspended cells must squeeze through narrow passages.

The non-Newtonian behavior of blood has been investigated extensively. Dutta and Tarbell [16] compared the effects of non-Newtonian blood flow in large elastic arteries using a power law model, a generalized Maxwell model, and a basic Newtonian model. They concluded that if the pressure gradients between Newtonian and non-Newtonian models were matched, the influence of non-Newtonian effects on the flow field were not significant. Most researchers assume Newtonian behavior for blood flow unless the arteries under consideration are very small.

The pulsatile nature of blood flow plays a dominant role in the fluid mechanics of the system. As the heart pumps blood throughout the body, the velocity and pressure of the flow field are unsteady in time. Figure 2.1 shows a generic velocity profile in an artery over the course of one complete pulse cycle. The initial phase of rapid flow acceleration and deceleration, during which the heart's ventricles contract and send blood to the body, is termed "systole." During the later phase, termed "diastole," the

ventricles relax and fill with blood. Taylor et al. [17] investigated the effects of pulsatile flow rate using magnetic resonance imaging to make *in vivo* quantifications of flow rate and wall shear stress (WSS) in the abdominal aorta during lower limb exercise on a stationary bicycle. Results showed that increasing heart rate during exercise reduced flow oscillations linked to the onset of arterial disease.

Wall shear stress is an important variable in artery hemodynamics. Bonert et al. [18] measured WSS in a 3D CAD-generated model of a normal human abdominal aorta to determine the relationship between WSS and intimal thickening (IT). The investigation focused on the infrarenal aorta and the aorto-iliac bifurcation. The model was based on a computer tomography scan of a healthy 35 year-old adult male. For visualization purposes, the model's inlet diameter was scaled up. A metallic replica of the computer model was then constructed using stereolithography. Steady flows of a fluid mimicking the viscosity of blood were pumped through the system under both resting and mild exercise conditions. Flow fields and WSS were measured using laser photochromic dye tracing, and IT was measured at 32 key locations from recent aortic autopsies. Results showed a positive correlation between high IT and low WSS, for both resting and exercise conditions, due to deposition of cells near regions of low WSS. This study was the first to look at patient-specific hemodynamics throughout the entire infrarenal aorta. Medical evidence has shown IT to be a predictor for arterial disease, including stenosis.

It has been suggested that steady flow might be used to depict the average behavior of pulsatile flow. Lee and Chen [19] performed a numerical simulation of steady flow in the abdominal aorta and its peripheral branches. Results were generally consistent with those obtained from pulsatile flows averaged over time. The study also found a link between regions of reversed flow and typical sites of stenosis, particularly in the infrarenal aorta. Experimental models of the abdominal aorta under various pulsatile flows have supported this link, showing flow abnormalities such as separation and vortices in frequently diseased areas. The abnormalities diminished or disappeared under exercise

conditions [20].

Experimental studies using pulsatile flow versus steady flow have revealed significant time-dependent variations in the hemodynamics of the abdominal aorta [21]. Conditions such as low wall shear stress, oscillating shear direction, and high particle residence times have been linked to plaque localization and consequently stenosis. Buchanan et al. [22] used a control-volume numerical model to investigate the effects of varying the pulse rate of a sinusoidal flow in straight axisymmetric arteries. They found that while vortices appeared in the flow regardless of the pulse rate, secondary vortices appeared downstream of the primary vortices for high pulse rates. Marques et al. [23] found similar results when keeping the pulse rate constant but varying the degree of stenosis in a CFD model of straight stenosed arteries. Severely stenosed arteries (70% closure) developed secondary vortices downstream. In light of these findings, it seems wise to include pulsatile flow when modeling the cardiovascular system, as in most modern in-depth numerical studies.

2.2 Intracranial Aneurysms

2.2.1 Medical findings

Surgical occlusion has been shown to be a safe and efficient technique for patients with intracranial aneurysms. Henkes et al. [24] evaluated early angiographic and clinical outcomes for 1811 patients who underwent ESO. Over 90% of the surgeries achieved high rates of occlusion, and over 80% of the patients encountered no complications. However, endovascular occlusion of aneurysms with unfavorable geometries, such as wide sac necks, remains a challenge. Kwon et al. [25] noted success in the treatments of 16 patients with wide-necked aneurysms (neck width $>$ aneurysm height) using a unique ESO procedure involving two microcatheters. All patients but one showed excellent clinical outcomes during the follow-up period. Unfortunately the procedure's effectiveness could not be

compared to other aneurysm treatments due to a lack of angiographic follow-up data.

Stent graft treatment of intracranial aneurysms is currently a fairly immature field. No large-scale or long-term clinical trials have been conducted on human subjects. While early success has been achieved with a variety of stent configurations and vascular geometries, most of this research has dealt with animal trials [26, 27] or case studies of single human subjects [28, 29]. A greater understanding of the general flow phenomena in human subjects will be needed for stent grafting to become a reliable and mature treatment option.

2.2.2 In vitro studies

Intracranial aneurysms typically cause strokes via subarachnoid hemorrhaging, in which the aneurysm sac ruptures and fills the surrounding space with blood, compressing nearby tissue and vessels. As blood flow persists within the diseased artery, a vortex develops within the aneurysm sac during systole and grows in strength as regions of recirculating flow roll back upon themselves after running into the distal (most downstream) sac wall [30].

Gobin et al. [31] constructed an *in vitro* model of an aneurysm to study the effects of vessel flow dynamics and ESO on flow patterns within the aneurysm during pulsatile flow. Vortices formed near the distal neck of the aneurysm during systole and varied in strength and location throughout the pulse cycle. Flow tended to stagnate at the center and along the top wall of the aneurysm. Surgical occlusion greatly increased fluid stagnation along the top wall, however the coils did not fully pack the aneurysm sac. Pressure measurements within the sac did not differ greatly from pressure in the vessel. This study demonstrated the dependency of aneurysm flow patterns on flow pulsatility, as well as the detrimental effects of poor compliance matching in coil occlusion.

2.2.3 CFD studies

Numerical simulations have been used in the last decade to analyze blood flow in aneurysms. Bluestein et al. [32] performed the first numerical simulations of steady flow in an aneurysm model. The aneurysm was modeled as a simple sphere-and-tube geometry. A recirculation region formed within the aneurysm sac, and regions of elevated wall shear stress correlated with regions that promoted blood platelet deposition and sac rupture taken from *in vitro* PIV measurements. The location of the recirculation region varied with the flow rate of the simulation. As the Reynolds number increased to near-turbulent conditions, the recirculation region migrated towards the distal end of the aneurysm sac. While Bluestein et al. demonstrated viable attempts to use CFD, the condition of steady flow is not realistic and the aneurysm geometry was very simple.

More recent numerical simulations have used more physiologically accurate geometries and flow parameters that demonstrate the capability of CFD to represent real blood flow. Fatouraee and Amini [33] combined medical imaging and CFD by using a commercial CFD package (FLUENT) to simulate the geometry and flow patterns found from magnetic resonance angiography (MRA) of an *in vitro* abdominal aortic aneurysm model based on phase contrast MRI. Streamlines constructed from the CFD results agreed well with the MRA results, demonstrating the ability of CFD to reproduce *in vitro* flow patterns. Steinman et al. [34] made a highly realistic carotid aneurysm model by combining CFD and high-resolution medical imaging. They based the numerical geometry on computed rotational angiography scans of a patient with a large internal carotid aneurysm and imposed a pulsatile inlet velocity profile based phase-contrast MRI measurements of another patient. The model predicted pulse cycle-averaged wall shear stress to be highest near the aneurysm neck. Although the study did not make comparisons with *in vivo* or *in vitro* flow fields, it presented the possibility of using CFD to study patient-specific geometries to predict the outcomes of interventional therapies.

2.3 Aortic Stent Reconstruction

2.3.1 Medical findings

Treatment of cardiovascular disease is a major area of research and funding in today's medical community. Erbel et al. [8] conducted a clinical study to determine if stenting reduced rates of restenosis in comparison to angioplasty. Restenosis rates dropped from 32% to 18% when stenting was used. This study was one of the first to demonstrate the effectiveness of stenting in reducing restenosis. A more recent long-term study by Reyes et al. [2] followed up on iliac wallstent placement in 303 legs of elderly patients treated between 1988 and 1998. The study reported complications in 18% of the legs during the follow-up period, with restenosis accounting for the majority of complications.

Restenosis rates remain a serious problem with room for improvement. While the exact causes and mechanics of restenosis are unclear, clinical studies have discovered many predictors. Diabetics and patients with high body mass indices face a particularly elevated risk of restenosis [35]. Stent geometry has also been correlated with restenosis rates. Mauri et al. [36] analyzed angiographic follow-ups on over 1000 patients from bare metal stent trials in coronary arteries. They found that restenosis rates rose when stent length exceeded arterial lesion length and recommended a conservative approach to matching stent and lesion lengths. Lower restenosis rates have been observed when lesions and stents are located remotely from any artery bifurcations. Unfortunately, bifurcations are common sites for plaque build-up and nearby stenting is often unavoidable.

Restenosis has also been linked to the size of the stented artery. Elezi et al. [37] investigated the influence of vessel diameter (D) on long-term clinical and angiographic outcomes after stenting. Patients were divided by stented vessel diameter into small ($D < 2.8$ mm), medium (2.8 mm $< D < 3.2$ mm), and large ($D > 3.2$ mm) groups. Event-free survival rates at the end of one year for the small, medium, and large groups

were 69.5%, 77.5%, and 81.0%, respectively. The small diameter group also had the highest rate of restenosis (38.6%) and the highest rate of major adverse cardiovascular events during the first 30 days after surgery (4.5%).

Two recent advancements in restenosis reduction are drug elution and radiation therapy. Drug-eluting stents today frequently feature sirolimus, a drug with both anti-inflammatory and anti-proliferative properties. A recent study [38] compared the success of sirolimus-eluting stents and standard stents in the treatment of native coronary artery blockage. Results showed a reduction in restenosis from 17% in the standard group to 4% in the sirolimus group.

The second advancement, radiation therapy, usually follows an angioplasty in which a stent is not implanted. The treatment is notable for suppression of neointimal formations following angioplasty. Radiation has the added benefit of not depending on uptake and metabolism by target cells, as is the case with drug elution. However, radiation can result in incomplete healing of arteries and usually requires prolonged anti-platelet therapy [39]. In any case, both radiation and drug elution have shown promising results in reducing restenosis, and the future of stenting treatments likely lies in these two directions.

2.3.2 In vitro studies

The majority of previous studies on flow patterns in stented arteries have been performed on *in vitro* environments. Berry et al. [40] constructed an artery model of elastomeric silicone and visualized flow patterns within the model using dye injection and a pumping system to supply a pulsatile flow. They investigated the disturbances introduced by two types of stents: Palmaz stents (an older design with a lattice network of fibers) and a prototype stent with axial-aligned fibers. Flow visualization for the Palmaz stent revealed flow stagnation between stent fibers and regions of reversed flow during systole. Vortices formed approximately 1.5 vessel diameters upstream from the stent during diastole. Dye washout time between the stent fibers increased from 4-5 pulse

cycles to 14-15 pulse cycles. The prototype stent also produced stagnation and vortex formation, but because it had fewer fibers and stronger diastolic fluid movement, the magnitudes of disturbances were smaller in comparison to the Palmaz stent. A pronounced region of reversed flow occurred with the Palmaz stent, even though the inlet waveform had no negative components.

The Berry et al. study was one of the first to qualitatively examine the fluid mechanical effects of stenting compliant vessels. A follow-up study several years later [41] investigated the dependence of flow disturbances on fiber spacing by inserting either 12-fiber or 18-fiber wallstents into the same silicone artery model with dye injection. The fiber counts refer to the number of fibers present in a set stent length. The 18-fiber stent therefore had a denser fiber configuration, and less inter-fiber spacing, than the 12-fiber stent. Both stent designs showed dye accumulation between fibers immediately upstream and downstream of the stent. The 12-fiber stent allowed for greater radially-inward wall movement during pressure drops in the pulse cycle. This motion may have important clinical implications. Reducing the number of stent fibers and fiber intersections has been linked to reduced restenosis in iliac arteries [42].

Robaina et al. [43] studied the effects of stent fiber spacing on platelet adhesion. The experimental setup was unique for using actual human blood with radioactively labeled platelets as a working fluid. They constructed a parallel plate flow chamber that essentially modeled 2D blood flow over stent fibers near the artery wall. Platelet adhesion both between fibers and on the fibers themselves was lowest when the spacing between stent fibers was smallest. The researchers attributed this finding to constantly recirculating flow and low WSS. While these phenomena may be beneficial to low platelet deposition, they represent deviations from normal physiological flow, and should generally be avoided. Even so, some controversy exists over whether small or large fiber spacings are more appropriate.

The orientation of stents within the arteries also plays a role in flow variations. Walsh

et al. [44] performed an experimental study of blood flow in an abdominal aorta model using dye injection. They created a glass-blown aorta model based on angiographic data that included the renal, iliac, and mesenteric arteries. Two stents with D-shaped cross-sections, similar to SMART stents, filled the infrarenal aorta and projected into the iliac arteries. With no stents present in the model, vortices formed directly beneath the renal arteries during diastole. With stent deployment, the vortices appeared slightly earlier in the diastolic phase, and were smaller in scale, but also more chaotic, in comparison to flow when the stents were absent from the model. The researchers attributed the increased vorticity to the division of the aorta passage by the stents. They also investigated the effects of varying the orientation of the stents within the aorta. Flow disturbances when the stents were aligned to touch the anterior-posterior or medial-lateral aortic walls were not appreciably different. Oblique configurations also failed to produce any detectable differences.

2.3.3 CFD studies

During the last decade, researchers in engineering and medical science have used computational models to study stented arteries. Berry et al. [41] simulated pulsatile flow very near the wall of a stented artery using the CFD-ACE code. Their model was a 2D flat plate with seven stent fibers represented as semicircles along the wall. The fibers greatly reduced the nearby flow velocity. The flow separated from the wall after encountering the first fiber, and re-attached to the wall between fibers when fiber spacing was less than 6 fiber diameters. Otherwise, regions of flow separation were continuous from fiber to fiber, thereby demonstrating the flow field's dependence on fiber spacing.

Early stent simulations suffered from a lack of computational power needed to run more complicated geometries. The great majority of notable CFD simulations on stent design featured only two-dimensional flow and geometries [45]. Previous research has shown it is important to consider full three-dimensional flow when modeling blood flow

over stent fibers. Jou [46] simulated steady 3D flow over stented walls using an artificial compressibility method to solve the Navier-Stokes equations. The model consisted of a flat wall with rounded criss-crossing ridges representing stent fibers. Streamlines near the artery wall showed that fluid particles moved around fibers in the cross-streamwise direction, along with moving perpendicular to the wall, indicating that three dimensions are needed to fully capture the hemodynamics of the flow.

Berry also investigated the effects of newer compliance-matching (CMS) stents [47]. The compliance mismatch between stent ends and the artery wall disturbs hemodynamics and WSS distributions. Compliance matching (CMS) stents smooth the transition between stent and wall. Finite element analysis was used to compare the hemodynamics and wall mechanics in a pigs superficial femoral artery between CMS and Palmaz stenting. Both stents were assigned material properties of 316L stainless steel. Geometric modeling was performed using PATRAN software, and the stress/strain solution was found using the ABAQUS finite element solver. Compliance was quantified as the ratio of change in cross-sectional area to change in pressure at the cross-section. In the rigid region of stent and artery intersection, the CMS reduced compliance by 60% compared to 90% for the Palmaz stent. The CMS also produced a gradual transition in compliance, while the Palmaz transition was more abrupt. Peak circumferential stress was about four times higher in the Palmaz stent than in the CMS. *In vivo* measurements on CMS stenting in pig arteries of similar diameters showed the CMS was effective in compliance matching and did not dampen downstream flow or pressure waveforms.

Schachter and Barakat [48] modeled pulsatile flow in straight and curved stented arteries using FLUENT. Their models represented stents with series of concentric circular rings. Results showed a separation zone downstream of the stent that increased in size when fiber diameter increased. The separation zone oscillated in magnitude as the inlet velocity varied, and produced oscillating WSS gradients.

More recently, LaDisa et al. [49] investigated the effects of stent design on WSS

patterns in a single straight artery. The stented vessels were generated using a custom-built Matlab algorithm. Flow was simulated using the CFD-ACE code. Their results showed that WSS distributions linked to stent failure were reduced when the number of fibers, fiber intersections, and fiber diameters were minimized. The simulations used a steady flow velocity corresponding to the average velocity of blood flow during a pulse cycle.

2.4 Summary

The preceding sections summarized relevant research and previous findings in studies on the hemodynamics of intracranial aneurysms and aortic stent reconstruction. Both systems will benefit from a greater understanding of the flow phenomena present during both healthy and diseased conditions. The next chapter details the numerical methodologies used in the present research to model the fluid mechanics of these two systems.

CHAPTER 3 NUMERICAL METHODOLOGIES

To address the research goals, numerical models of an intracranial aneurysm and a stented aorta-iliac bifurcation were created using GAMBIT version 2.0.4 [50], a commercial CFD preprocessor that creates grids. Flow simulations were conducted using FLUENT version 6.1 [51], a commercial CFD code. The following sections detail the governing equations of fluid flow and how they are discretized in space and time within FLUENT. The numerical formulation and the FLUENT solution loop are also outlined. Finally, the methods of mesh generation and the construction of the numerical geometry are presented.

3.1 Governing Equations

The three-dimensional Navier-Stokes equations for flows without heat and mass transfer are the continuity and momentum equations. The system of equations includes four primitive variables: pressure and three velocity components corresponding to a coordinate system. For laminar flows, the mass conservation (continuity) equation is:

$$\frac{\partial \rho}{\partial t} + \nabla \cdot (\rho \vec{v}) = S_m \quad (3.1)$$

where ρ is the fluid density, \vec{v} is the velocity vector, and S_m is the mass source term.

The momentum conservation equations are:

$$\frac{\partial}{\partial t} (\rho \vec{v} \vec{v}) = -\nabla p + \nabla \cdot (\vec{\tau}) + \rho \vec{g} + \vec{F} \quad (3.2)$$

where p is the static pressure, $\bar{\tau}$ is the stress tensor, $\rho\vec{g}$ is the gravitational body force, and \vec{F} is an external body force. The stress tensor $\bar{\tau}$ is given by:

$$\bar{\tau} = \mu \left[(\nabla\vec{v} + \nabla\vec{v}^T) - \frac{2}{3}\nabla \cdot \vec{v}I \right] \quad (3.3)$$

where μ is the fluid dynamic viscosity and I is the unit tensor. For the research herein, blood flow is assumed incompressible and $S_m = 0$. The hemodynamic analyses do not involve forces, therefore the last two terms of Eq. 3.2 are zero. Furthermore, based on reported literature [15], blood in the arteries investigated for this research can be modeled as a Newtonian fluid, reducing Eq. 3.3 to:

$$\bar{\tau} = \mu\nabla^2\vec{v} \quad (3.4)$$

3.2 Numerical Methodology

3.2.1 Spatial discretization

FLUENT uses a finite-volume technique to discretize Eqs. 3.1 and 3.2 into algebraic equations that can be solved numerically. FLUENT integrates each equation about each cell and yields discrete equations that conserve mass and momentum for each control-volume cell. Discretization of the governing equations is illustrated by considering the conservation equation for transport of a scalar quantity ϕ for an arbitrary control-volume V :

$$\oint \rho\phi\vec{v} \cdot d\vec{A} = \oint \Gamma_\phi\nabla\phi \cdot d\vec{A} + \int_V S_\phi dV \quad (3.5)$$

where \vec{A} is the surface area vector, Γ_ϕ is the diffusion coefficient for ϕ , and S_ϕ is the source of ϕ per unit volume.

Figure 3.1 illustrates an arbitrary control volume for tetrahedral cells for scalar transport. Once discretized, Eq. 3.5 becomes:

$$\sum_f^{N_{faces}} \rho_f\vec{v}_f\phi_f \cdot \vec{A}_f = \sum_f^{N_{faces}} \Gamma_\phi(\nabla\phi)_n \cdot \vec{A}_f + S_\phi V \quad (3.6)$$

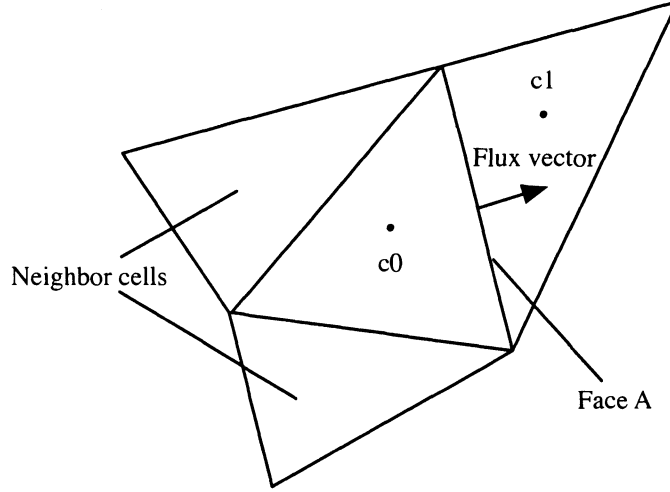


Figure 3.1 Control volume illustrating discretization and transport.

where N_{faces} is the number of faces enclosing the cell, ϕ_f is the value of ϕ convected through face f , \vec{A}_f is the area of face f , $(\nabla\phi)_n$ is the magnitude of $\nabla\phi$ normal to face f , and V is the cell volume. The equations solved by FLUENT take the same general form as Eq. 3.6 and apply readily to the three-dimensional unstructured grids used in this research.

By default, FLUENT stores values for ϕ at cell centers ($c0$ and $c1$ in Fig. 3.1). However, the convection terms in Eq. 3.6 require the face values ϕ_f which must be interpolated from center values. Interpolation is accomplished using an upwind scheme in which values for ϕ_f are derived from quantities in the upstream cell relative to the direction of the normal velocity. For improved accuracy, the simulations used a second-order upwind scheme which achieved higher-order accuracy at cell faces through a Taylor series expansion of the cell-centered solution about the cell centroid. The face value ϕ_f is computed by as:

$$\phi_f = \phi + \nabla\phi \cdot \Delta\vec{s} \quad (3.7)$$

where $\Delta\vec{s}$ is the displacement vector from the upstream cell centroid to the face centroid. Equation 3.7 requires the gradient $\nabla\phi$ which is computed using the discrete form of the

divergence theorem:

$$\nabla\phi = \frac{1}{V} \sum_f^{N_{faces}} \tilde{\phi}_f \vec{A} \quad (3.8)$$

The face value $\tilde{\phi}_f$ is computed by averaging ϕ from the two cells adjacent to the face. The gradient is also limited so that no new minima or maxima are introduced.

The diffusion terms in Eq. 3.6 are discretized using a second-order accurate central-difference scheme that calculates the face values ϕ_f :

$$\phi_{f,CD} = \frac{1}{2} (\phi_0 + \phi_1) + \frac{1}{2} (\nabla\phi_{r,0} \cdot \vec{r}_0 + \nabla\phi_{r,1} \cdot \vec{r}_1) \quad (3.9)$$

where the indices 0 and 1 refer to cells that share the face f , $\nabla\phi_{r,0}$ and $\nabla\phi_{r,1}$ are the reconstructed gradients at cells 0 and 1, respectively, and \vec{r} is the vector directed from the cell centroid to the face centroid.

It is well known that central-differencing schemes can lead to unbounded solutions and non-physical ‘‘wiggles,’’ which can cause numerical stability issues. FLUENT avoids these stability problems by using a deferred approach for central-differencing in which the face value is calculated as follows:

$$\phi_f = \phi_{f,UP} + (\phi_{f,CD} - \phi_{f,UP}) \quad (3.10)$$

where UP stands for upwind and CD stands for central-difference. The UP terms in Eq. 3.10 may appear redundant, however the first term ($\phi_{f,UP}$) is treated implicitly while the second term ($\phi_{f,CD} - \phi_{f,UP}$) is treated explicitly. Provided that the solution converges, the scheme in Eq. 3.10 will lead to pure second-order central-differencing.

3.2.2 Temporal discretization

The simulations in this research model pulsatile flows that vary in intensity over time. To account for this variation, the governing equations are discretized in space as well as time. A general expression for the time evolution of a variable ϕ is given by:

$$\frac{\partial\phi}{\partial t} = F(\phi) \quad (3.11)$$

where the function $F(\phi)$ incorporates any spatial discretization. For this research the time derivative was discretized using a second-order backward difference:

$$\frac{3\phi^{n+1} - 4\phi^n + \phi^{n-1}}{2\Delta t} = F(\phi) \quad (3.12)$$

where n represents the current time level and Δt is the specified time step. Once the time derivative is discretized, a choice remains for what time level of ϕ to use in evaluating F . The method for these simulations uses an implicit time integration to evaluate F at a future time level by initializing ϕ^i to ϕ^n and iterating the second-order equation:

$$\phi^i = \frac{4}{3}\phi^n - \frac{1}{3}\phi^{n-1} + \frac{2}{3}\Delta t F(\phi^i) \quad (3.13)$$

until ϕ^i converges, at which point ϕ^{n+1} is set to ϕ^i .

3.2.3 Evaluating gradients

The gradient $\nabla\phi$ is used to discretize the convection and diffusion terms of the governing equations. The gradient is computed using the Green-Gauss theorem:

$$(\nabla\phi)_{c0} = \frac{1}{V} \sum_f \bar{\phi}_f \bar{A}_f \quad (3.14)$$

By default the face value $\bar{\phi}_f$ is the arithmetic average of the values at the neighboring cell centers. For this research, $\bar{\phi}_f$ is alternatively computed as an arithmetic average of the nodal values on the face:

$$\bar{\phi}_f = \frac{1}{N_f} \sum_n^{N_f} \bar{\phi}_n \quad (3.15)$$

where N_f is the number of nodes on face f . The nodal values $\bar{\phi}_n$ are computed from the weighted average of the cell values surrounding the nodes [52]. The node-based averaging scheme of Eq. 3.15 is known to be more accurate than the cell-based scheme for unstructured meshes, most notably for triangular and tetrahedral meshes.

3.2.4 Linearization

The discretized general transport equation (Eq. 3.6) contains the unknown scalar variable ϕ at the cell center along with the unknown values in surrounding neighbor cells. Equation 3.6 is generally nonlinear with respect to these variables. A linearized form of Eq. 3.6 can be written as:

$$a_p\phi = \sum_{nb} a_{nb}\phi_{nb} + b \quad (3.16)$$

where the subscript nb refers to neighbor cells and a_p and a_{nb} are the linearized coefficients of ϕ and ϕ_{nb} , respectively. The term b is the linearized source term. With the exception of boundary cells, the number of neighbor cells typically equals the number of faces enclosing the cell. Equations similar to Eq. 3.16 can be written for each cell in the domain, resulting in a system of algebraic equations with a sparse coefficient matrix. For scalar equations FLUENT solves this matrix using a point implicit (Gause-Seidel) linear equation solver in conjunction with an algebraic multigrid (AMG) method (Appendix A).

3.3 The Segregated Solver

FLUENT allows the choice of a segregated solver which solves Eqs. 3.1 and 3.2 sequentially, or a coupled solver which solves both equations simultaneously. The coupled solver was designed to solve high-speed compressible flows, and requires much more memory and CPU time than the segregated solver. Since the flows in this research were low-speed and assumed incompressible, the segregated solver was used for all simulations.

In this section, the discretization of the momentum and continuity equations and their solutions by the segregated solver are addressed. Consider the steady-state mo-

momentum and continuity equations in integral form:

$$\oint \rho \vec{v} \cdot \vec{A} = - \oint p I \cdot d\vec{A} + \oint \bar{\tau} \cdot d\vec{A} + \int_V \vec{F} dV \quad (3.17)$$

$$\oint \rho \vec{v} \cdot d\vec{A} = 0 \quad (3.18)$$

where \vec{F} is the force vector.

3.3.1 Discretization of the momentum equation

The discretization scheme described earlier for a scalar transport equation is also used to discretize the momentum equation. For example, the u -momentum equation can be obtained by setting $\phi = u$:

$$a_p u = \sum_{nb} a_{nb} u_{nb} + \sum p_f A \cdot \hat{i} + S \quad (3.19)$$

If the pressure field and face mass fluxes are known, Eq. 3.19 can be solved to obtain a velocity field. However, the pressure field and face mass fluxes are not known beforehand and must be obtained as a part of the solution. FLUENT uses a co-location scheme whereby pressure and velocity are both stored at cell centers. However, Eq. 3.19 requires the pressure value at the face between two cells $c0$ and $c1$ shown in Fig. 3.1. An interpolation scheme is required to compute the face values of pressure from the cell values.

3.3.2 Pressure interpolation

The default scheme in FLUENT interpolates the pressure values at the faces using momentum equation coefficients [53]. The procedure works well as long as the pressure variation between cell centers is smooth. When there are large gradients between cells, the scheme produces inaccurate velocities. An alternate pressure interpolation method, the PREssure STaggering Option (PRESTO!) scheme, uses the discrete continuity balance for a staggered control volume about the face to compute the staggered, or face,

pressure. This procedure is similar to the staggered-grid schemes used with structured meshes [54]. The PRESTO! scheme is particularly beneficial for flows involving porous media that introduce large pressure changes between cells, and was selected for these simulations [51].

3.3.3 Discretization of the continuity equation

Integrating Eq. 3.18 over a control volume yields the following discrete equation:

$$\sum_f^{N_{faces}} J_f A_f = 0 \quad (3.20)$$

where $J_f = \rho v_n$ is the mass flux through face f . As mentioned earlier, the momentum and conservation equations are solved sequentially. The continuity equation is used as an equation for pressure. However, for incompressible flows, pressure does not appear explicitly in Eq. 3.20 since density is not directly related to pressure. The Semi-Implicit Method for Pressure-Linked Equations (SIMPLE) family of algorithms [54] is used to introduce pressure into the continuity equation. This procedure is detailed in the next section.

To proceed further, the face values of velocity \vec{v}_n must be related to the stored velocities at cell centers. To prevent the checker-boarding in the pressure solution when cell-centered velocities are interpolated onto faces, FLUENT uses a procedure similar to that of Rhie and Chow [53]. Momentum-weighted averaging, using weighting factors based on the coefficient a_p from Eq. 3.19 is performed. Using this procedure, the face flux J_f is:

$$J_f = \hat{J}_f + d_f (p_{c0} - p_{c1}) \quad (3.21)$$

where p_{c0} and p_{c1} are the pressures within the two cells on either side of the face. The term \hat{J}_f contains the influence of velocities in the two cells on either side of the face f . The term d_f is a function of the average of the momentum equation coefficient a_p for these cells.

3.3.4 Pressure-velocity coupling

Pressure-velocity coupling is achieved using Eq. 3.21 to derive an equation for pressure from the discrete continuity equation using the SIMPLE family of algorithms. The basic SIMPLE algorithm uses a relationship between velocity and pressure corrections to enforce mass conservation and to obtain the pressure field. If the momentum equation is solved with a guessed pressure field p^* , the resulting face flux J_f^* computed from Eq. 3.21 does not satisfy the continuity equation. Consequently, a correction flux J'_f is added to the face flux J_f^* to obtain the corrected face flux J_f , which satisfies the continuity equation. The SIMPLE algorithm postulates that J'_f may be written as:

$$J'_f = d_f (p'_{c0} - p'_{c1}) \quad (3.22)$$

where p' is the cell pressure correction. The SIMPLE algorithm substitutes Eqs. 3.16 and 3.22 into Eq. 3.20 to obtain a discrete equation for the pressure correction p' in the cell:

$$a_P p' = \sum_{nb} a_{nb} p'_{nb} + b \quad (3.23)$$

where a_P is the cell center coefficient, a_{nb} are the influence coefficients of neighbor cells, the source term b is the net flow rate into the cell:

$$b = \sum_f^{N_{faces}} J_f^* A_f \quad (3.24)$$

Equation 3.23 may be solved using the AMG method. Once a solution is obtained, the cell pressure and face flux are corrected using Eqs. 3.25 and 3.26:

$$p = p^* + \alpha_p p' \quad (3.25)$$

$$J_f = J_f^* + d_f (p'_{c0} - p'_{c1}) \quad (3.26)$$

where α_p is the under-relaxation factor for pressure. The corrected face flux J_f satisfies the discrete continuity equation during each iteration.

Within the SIMPLE family of algorithms, the Pressure-Implicit with Splitting of Operators (PISO) algorithm [55] is highly recommended for transient flows. PISO adds two additional corrections to the basic SIMPLE algorithm: neighbor correction and skewness correction. PISO can dramatically reduce the number of iterations needed for convergence in transient flows, and is also recommended for calculations on highly skewed meshes. Therefore PISO was employed in these simulations.

3.3.5 Time-dependent calculations

For the time-dependent flows seen in these simulations, the discretization of the general transport equations has the following form:

$$\int_V \frac{\partial}{\partial t} (\rho\phi) dV + \oint \rho^{n+1} \phi^{n+1} \vec{v}^{n+1} \cdot d\vec{A} = \oint \Gamma_\phi^{n+1} \nabla \phi^{n+1} \cdot d\vec{A} + \int_V S_\phi^{n+1} dV \quad (3.27)$$

The temporal discretization of the transient derivative in Eq. 3.27 was described in Sect. 3.2.2. The segregated solver uses an implicit discretization of Eq. 3.27, and as a default approach, all convective, diffusive, and source terms are evaluated from the fields for time level $n + 1$.

3.3.6 Residuals in the segregated solver

The discretization using the segregated solver for the conservation equation of a scalar variable ϕ at a cell P can be written as:

$$a_P \phi_P = \sum_{nb} a_{nm} \phi_{nb} + b \quad (3.28)$$

Here the source term b is the contribution of boundary conditions and the constant part of the source term S_c in $S = S_c + S_P \phi$. In Eq. 3.28 the center coefficient a_P is defined as:

$$a_P = \sum_{nb} a_{nb} - S_P \quad (3.29)$$

The residual R^ϕ is the imbalance in the conservation of ϕ that exists and cell P and summed over all computational cells P . This residual is written as:

$$R^\phi = \sum_P \left| \sum_{nb} a_{nb} \phi_{nb} + b - a_P \phi_P \right| \quad (3.30)$$

To scale the residuals in Eq. 3.30, a scaling factor representative of the flow rate of ϕ is introduced:

$$R_{scaled}^\phi = \frac{\sum_P |\sum_{nb} a_{nb} \phi_{nb} + b - a_P \phi_P|}{\sum_P |a_P \phi_P|} \quad (3.31)$$

For the momentum equation the denominator term $a_P \phi_P$ of Eq. 3.31 is replaced by $a_P v_P$, where v_P is the magnitude of velocity in cell P . The unscaled residual for the continuity equation is defined as:

$$R^c = \sum_P |\text{rate of mass creation in cell } P| \quad (3.32)$$

To scale the continuity residual R^c , the right-hand side of Eq. 3.32 is divided by the largest absolute value of the continuity residual in the first five iterations:

$$R_{scaled}^c = \frac{R_N^c}{R_5^c} \quad (3.33)$$

3.3.7 Solution loop

To reach a converged solution for the nonlinear discretized equations, FLUENT performs multiple iterations of a solution loop. A single iteration for the segregated solver consists of the following steps:

1. Fluid properties are updated based on the current solution. If the calculation has just begun, fluid properties are updated based on the initial conditions.
2. The momentum equation is solved using the current values for pressure and cell face mass fluxes to update the velocity field.

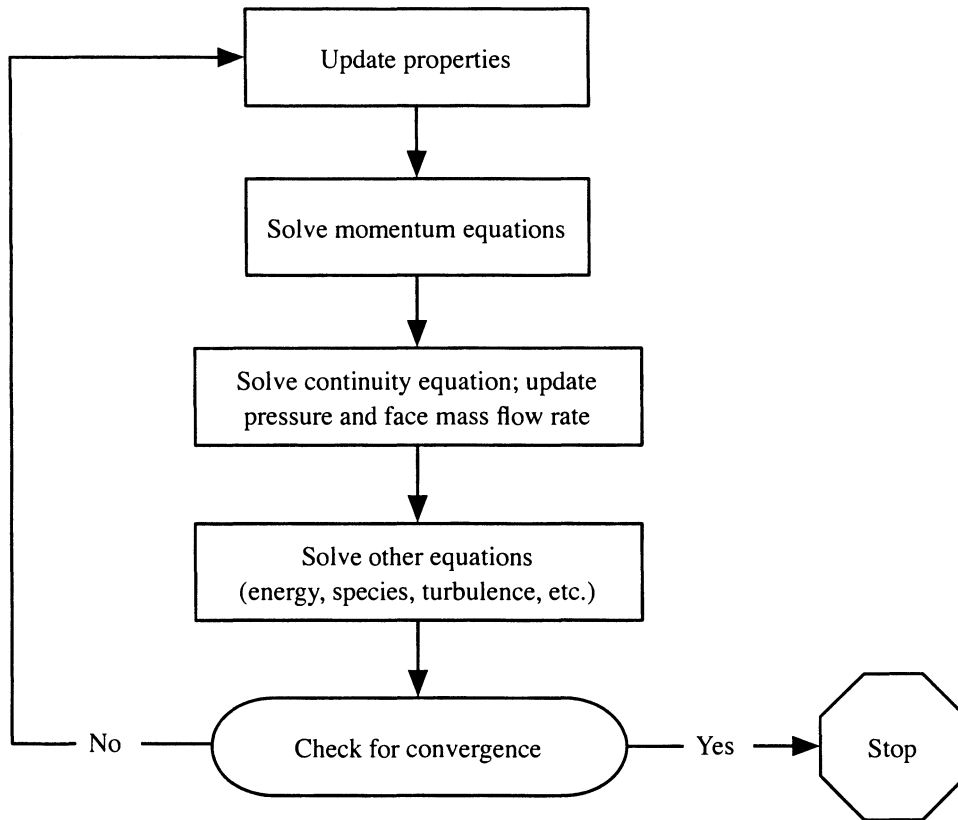


Figure 3.2 The FLUENT segregated solver solution loop.

3. Since the velocities obtained in step 2 may not satisfy the continuity equation locally, a Poisson-type equation for pressure correction is derived from the continuity equation and the linearized momentum equations. This pressure correction equation is solved to obtain the necessary corrections to the pressure and velocity fields and the cell face mass fluxes such that continuity is satisfied.
4. A check for convergence is made. The loop returns to step 1 and continues until convergence criteria are met.

Figure 3.2 summarizes the segregated solver solution loop graphically.

In the segregated solver, Eqs. 3.1 and 3.2 are linearized implicitly with respect to each equation's dependent variable, resulting in a system of linear equations with one

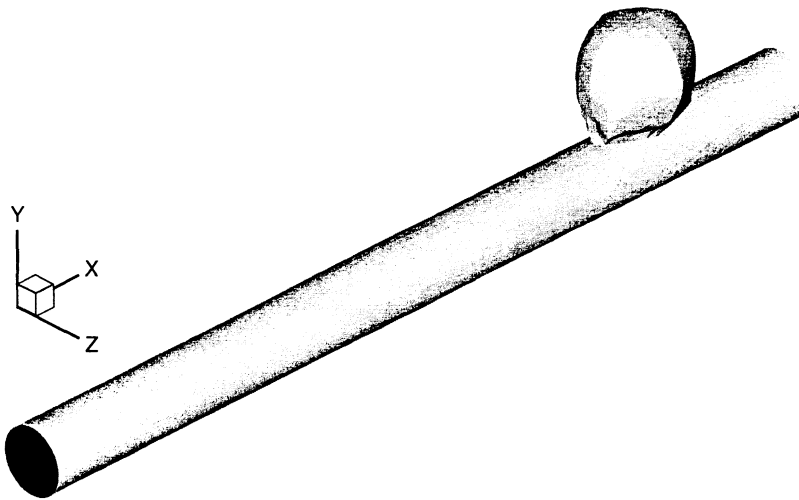


Figure 3.3 Geometry for the carotid artery and aneurysm.

equation in each cell in the domain. A point implicit (Gause-Seidel) linear equation solver is used in conjunction with an AMG method to solve the system of equations for the unknown variable in each cell. The AMG method is detailed in Appendix A.

In summary, the segregated solver computes a single primitive variable, such as p or u , by considering all cells simultaneously. The solver then calculates the next variable field and so on until it has solved for all unknown variables in the domain.

3.4 Mesh Generation

The model geometries are created and meshed using GAMBIT version 2.0.4 [50]. The cylindrical and radial volumes of the aneurysm, bifurcation, and stents require the use of GAMBIT's TGrid scheme for successful meshing. The TGrid scheme specifies that the mesh be composed of primarily tetrahedral mesh elements (cells). The TGrid meshing algorithm first meshes all faces with a Tri-Pave scheme consisting of triangular face elements. The volume is then meshed with tetrahedral elements. The scheme also utilizes hexahedral, pyramidal, and wedge elements where appropriate, however

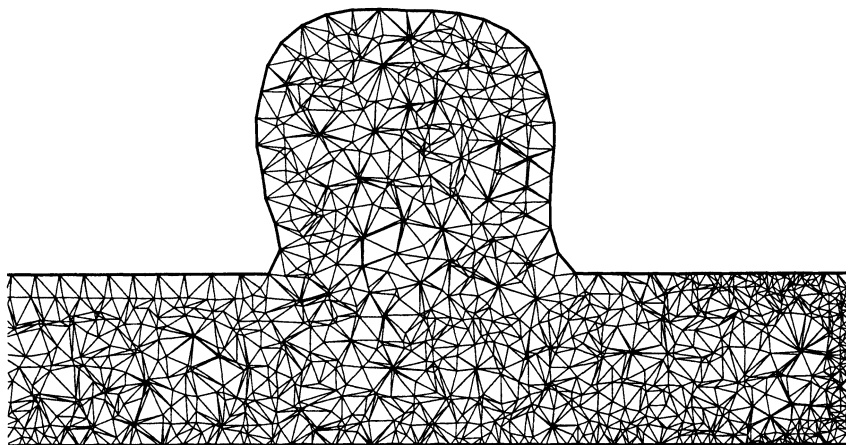


Figure 3.4 Mesh for the aneurysm geometry at the $x - y$ centerplane ($z = 0$).

these elements are only needed in volumes that contain attached boundary layers or quadrilateral face elements. Meshes for this research consist entirely of triangular face elements and tetrahedral volume elements.

The aneurysm geometry was based on a realistically-sized elastic wall model of an intracranial side-wall aneurysm used in microPIV experiments (see Appendix B). Figure 3.3 shows the aneurysm geometry built using GAMBIT. The artery diameter is approximately 5 mm and the aneurysm diameter varies between 7–8 mm. The artery was 60 mm long from entrance to exit. To emphasize the tetrahedral grid cells, Fig. 3.4 illustrates an enlargement of the mesh geometry near the aneurysm at the $x - y$ centerplane ($z = 0$).

The aorta-iliac bifurcation geometry was built by junctioning three cylinders together with a sphere. A large cylinder (diameter = 19 mm, length = 40 mm) representing the aorta runs parallel to the vertical y -axis. A sphere (diameter = 19 mm) was placed at the base of the large cylinder. Two small cylinders (diameter = 9 mm, length = 30 mm) representing the iliacs project at angles of 150° and 210° from the y -axis, which create a bifurcation angle of 60° between the iliac arteries. The intersections of the iliac arteries and the sphere are smoothed using fillets. Figure 3.5 shows the final bifurcation

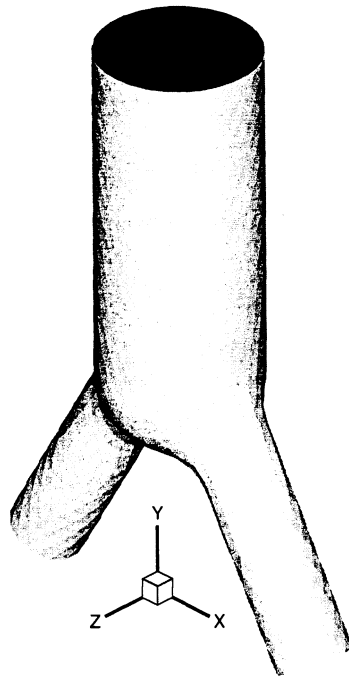


Figure 3.5 Geometry for the unstented aorta-iliac bifurcation.

geometry.

Stent geometries were created by junctioning two cylinders together with a sphere with the same diameter. Figure 3.6 shows a wireframe of the aorta-iliac geometry with two stents inserted. Stents are oriented such that the portion of the stent in the aorta is parallel to the y -axis with a sphere placed at the base. A second stent cylinder projects into the iliac at an angle of either 150° or 210° from the y -axis, dependent on if it is placed in the left or right iliac artery. Initially stents were modeled as having the same 9-mm diameter as the iliac arteries. However, stents and iliac arteries with equivalent diameters imposed two boundary conditions at the diameter faces, thus overspecifying the solution (and FLUENT crashed). To fix this problem, stent diameters were reduced by two cell widths ($\Delta x = 0.4$ mm) and the final stent diameter is 8.2 mm. The total length of every stent modeled in this research is 25 mm. Figure 3.7 illustrates an enlargement of the mesh geometry for the stented bifurcation at the $x - y$ centerplane

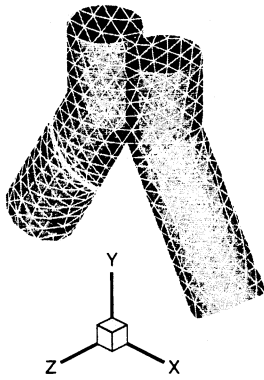


Figure 3.6 Wireframe of the stented aorta-iliac bifurcation.

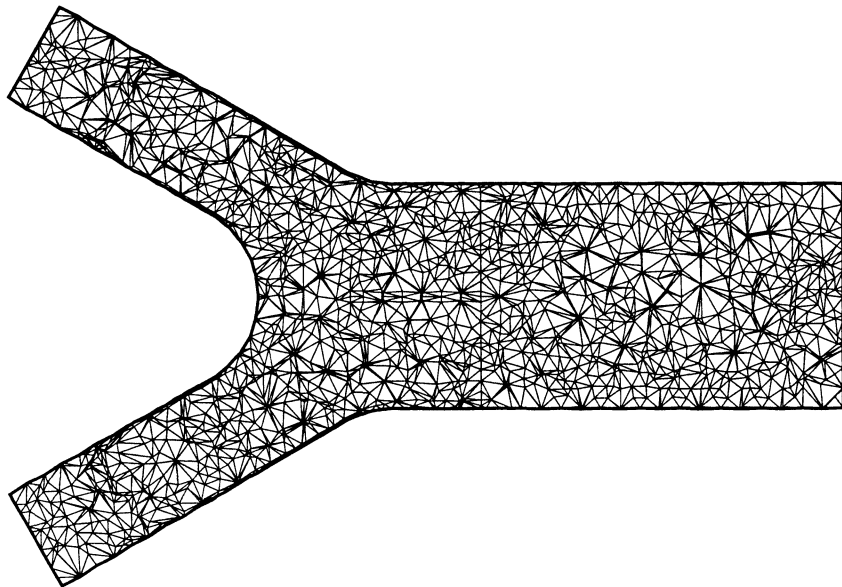


Figure 3.7 Mesh for the stented bifurcation geometry at the $x - y$ centerplane ($z = 0$).

($z = 0$).

The next two chapters detail the boundary conditions, initial conditions, grid resolution tests, and final results of the intracranial aneurysm simulations (Chapter 4) and the stent reconstruction simulations (Chapter 5). Details on the cell size, time step size, working fluid, and computational performance are also included.

CHAPTER 4 SIMULATION OF THE INTRACRANIAL ANEURYSM

In this chapter, aneurysm simulations are compared to experiments performed for flow in an actual-sized flexible-wall model of a human carotid artery with a side-wall aneurysm. A pumping device that supplied approximately the same pressure waveform found in an actual aneurysm over a complete pulse cycle replicated flow through the model. Instantaneous velocity fields within the aneurysm at various phases in the pulse cycle were measured using microscopic particle image velocimetry (microPIV). Details on the microPIV system used in these experiments are given in Appendix B.

4.1 Boundary and Initial Conditions

The aneurysm simulations used three types of boundary conditions. The aneurysm inlet, shown on the far left of Fig. 3.3, specified a velocity field. The artery length was sufficiently long so that the plug flow develops into parabolic flow before reaching the aneurysm. Additional details on the form of the inlet velocity profile will be addressed for specific simulations.

The aneurysm outlet, shown on the far right of Fig. 3.3, specified an outflow condition. Outflow boundaries in FLUENT are used to model flow exits where the details of velocity and pressure are not known prior to the solution of the problem. No properties are defined and FLUENT extrapolates pressure and velocity from nearby interior cells. The radial surface of the artery and the aneurysm sac walls were specified as rigid walls

with a no-slip condition. All aneurysm simulations were initialized to quiescent flow conditions; pressure and all velocity components were initialized to zero.

4.2 Grid Resolution and Working Fluid

The aneurysm geometry was created using GAMBIT as discussed in Sect. 3.4. The model was meshed with approximately 33,000 cells. The mesh was validated using the grid converge index method [56, 57] to quantify discretization error. A comparison for extrapolated errors and grid convergence indices for aneurysm neck pressures and downstream u -velocities on three successively finer meshes is shown in Table 4.1. The GCI results indicate that a 33,000-cell mesh was sufficient for relatively grid-independent solutions, with error less than 0.4%.

Table 4.1 Mesh convergence studies for coarse (3), medium (2), and fine (1) aneurysm meshes. Superscript notation refers to a comparison between two meshes. ϕ_A = pressure at $(x, y, z) = (10.4, 2.4, 0)$ mm. ϕ_B = u -velocity at $(x, y, z) = (17.0, 0, 0)$ mm.

Grid	N_{cells}	ϕ_A (Pa)	ϕ_B (m/s)
Coarse (3)	6682	84.29	0.0448
Medium (2)	16706	90.58	0.0669
Fine (1)	33209	91.37	0.0659
Apparent order (p)		6.43	10.69
Approximate (a) relative error			
e_a^{32}		6.94%	32.93%
e_a^{21}		0.86%	1.44%
Extrapolated (ext) relative error			
e_{ext}^{32}		1.12%	1.29%
e_{ext}^{21}		0.26%	0.14%
Grid convergence index			
GCI_{medium}^{32}		1.41%	1.63%
GCI_{fine}^{21}		0.32%	0.17%

Aneurysm meshes were created running GAMBIT on Iowa State University's College-Level Unified Environment Network on a SunFire V480 with four 900 MHz UltraSparc

III-Cu processors and 16 GB of memory [59]. The system required approximately five minutes to generate the 33,000-cell aneurysm mesh.

The working fluid for the aneurysm simulations was liquid water ($\rho = 1000 \text{ kg/m}^3$, $\mu = 1 \text{ centipoise}$). Blood properties were not used for these simulations in order to match the working fluid used in the microPIV experiments (see Appendix B).

4.3 Computational Performance and Post-Processing

Fluid dynamics simulations were performed on an Intel Xeon cluster at Iowa State University's High Performance Computing Center. The cluster features 44 nodes each with dual 2.8 GHz Intel Xeon processors and 2 GB of memory. Each processor has a 400 MHz front-side bus for a maximum memory bandwidth of 3.2 GB/s [60]. All simulations in this research were performed by running FLUENT in parallel on one node of this cluster. The cluster required approximately three hours of CPU time to reach converged solutions for the aneurysm simulations. Convergence within each time step was attained for all simulations when scaled residuals for pressure and velocity each dropped by at least four orders of magnitude. A time step of $\Delta t = 1/360 \text{ s}$ was used so that one time step represented one degree of a pulse cycle. Note that the stability of the segregated solver is independent of the time step and Δt may be chosen arbitrarily [51].

The output data files for each simulation were re-loaded into FLUENT. Since FLUENT stores a very large amount of information in its data files, the output data was post-processed to include only the pressure, velocity, and wall shear stress in surfaces of interest. Post-processed data files were visualized using Tecplot version 10 (Tecplot Incorporated, Bellevue, WA)

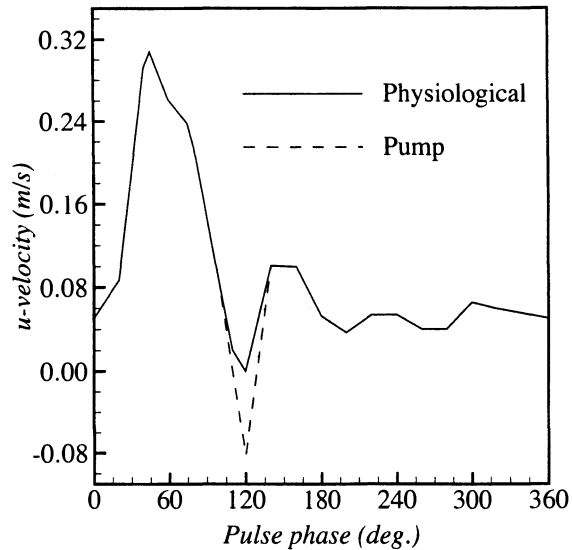


Figure 4.1 Inlet boundary conditions used in the numerical simulations for the pump flow (dashed line) and the physiological flow (solid line) conditions.

4.4 Simulation Results

An important flow phenomenon observed in the microPIV experiments was the formation and decay of a vortex within the aneurysm. The magnitude and position of the vortex varied with the phase of the pulse cycle. Numerical simulations were performed to determine if the CFD aneurysm model accurately predicted the physics observed in the microPIV experiments. In the aneurysm simulation results, the term “vorticity” refers to the spanwise vorticity component in the $x - y$ plane, given by:

$$\omega_z = \frac{\partial v}{\partial x} - \frac{\partial u}{\partial y} \quad (4.1)$$

4.4.1 Constant inlet velocity

The first aneurysm simulation used a fixed velocity of 0.11 m/s at the artery inlet such that a steady flow field developed and persisted over the course of the simulation. A small vortex developed near the center of the aneurysm and remained constant in both magnitude and position. This first simulation demonstrated that variations in

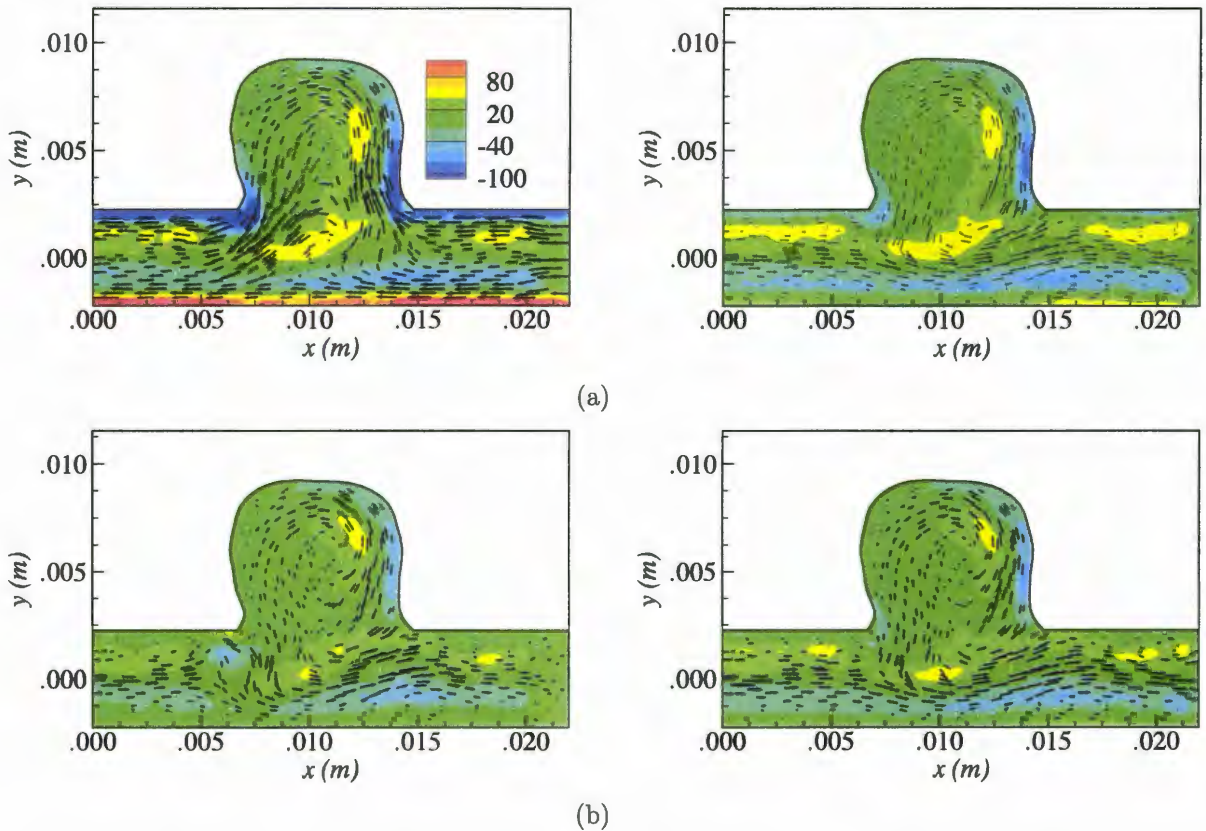


Figure 4.2 Velocity vectors superimposed on spanwise vorticity contours (1/s) for aneurysm simulations using the “pump” (left) and “physiological” (right) inlet waveforms at pulse phases of (a) 120° and (b) 130° .

vortex magnitude and position were not present when the inlet velocity was constant. Furthermore, although the governing equations of flow were discretized in both space and time, the result was a steady-state solution, demonstrating that the pulsatile nature of flow impacts vortex development.

4.4.2 Pump flow versus physiological flow

Experiments were performed for flow in an actual-sized flexible-wall model of a human carotid artery with a side-wall aneurysm (see Appendix B). A pumping device that supplied approximately the same pressure waveform found in an actual aneurysm replicated flow through the artery model. The velocity waveform generated for an entire pulse

cycle is shown in the dashed curve labeled “pump” in Fig. 4.1. Figure 4.1 demonstrates that the velocity waveform varies as a function of the phase of the pulse cycle, where a full pulse cycle is 360° . The slight negative velocity near 120° was due to limitations of the reciprocity pump used to produce the waveforms. In actual physiological systems, velocity should remain at or above zero for the entire pulse cycle.

The following set of aneurysm simulations was conducted to determine if the small negative velocities that occur for a slight duration in the microPIV pump’s waveform (shown in Fig. 4.1 and labeled “pump”) resulted in unrealistic flow patterns compared to actual carotid artery flows, whose velocities remain at or above zero over the entire pulse cycle (shown in Fig. 4.1 and labeled “physiological”). Figure 4.2 compares velocity vectors superimposed over vorticity contours for simulations using the “pump” and “physiological” inlet boundary conditions. At the pulse cycle phase of 130° (Fig. 4.2b), the velocity and vorticity data are nearly equivalent, with a maximum percent difference of less than 1%. The only significant disagreement in the two simulations was for phases ranging from 115° to 125° owing to the fact that the “pump” waveform reversed flow at the inlet during this phase range. Figure 4.2a illustrates the differences between the two simulations at the 120° phase where the reversed flow in the “pump” condition induces fluid to move upstream (from right to left). Otherwise all other phase comparisons showed virtually identical velocity and vorticity irrespective of the imposed inlet condition. Based on the observation that the brief negative velocities in the “pump” waveform did not adversely affect the overall transient flow field, the aneurysm simulation using the “pump” waveform was compared directly to the microPIV results. The Reynolds number for the “pump” waveform was defined as:

$$Re = \frac{\rho u D}{\mu} \quad (4.2)$$

where ρ and μ are the fluid density and viscosity, u is the magnitude of fluid velocity at the artery inlet, and D is the artery diameter. For the “pump” waveform Re varied

between zero and 1585.

Figure 4.3 presents velocity vectors superimposed on vorticity contours at pulse phases of 40° , 60° , 240° , and 360° for the numerical simulations (left frames) and the microPIV experiments (right frames). Each set of frames depicts the flowfield for the $x - y$ centerplane ($z = 0$) of the aneurysm.

During both the numerical simulations and the experiments, vortices formed during the systolic phase of the pulse cycle and were located near the distal aneurysm neck. This finding was consistent with the experimental results of Gobin et al. [31] and the numerical simulation by Blustein et al. [32]. Both of these studies observed vortex migration towards the distal wall during flow acceleration. At 40° (Fig. 4.3a) the velocity is near the maximum in the pulse cycle (refer to Fig. 4.1). The numerical results show a stronger and more clearly developed vortex near the aneurysm neck. At this phase, the flow is primarily through the artery although a small vortex eddy does form within the aneurysm. Figure 4.3b presents results at 60° which corresponds to a phase on the descent of the pulse cycle. The flow tends to travel straight through the artery. It is during this deceleration phase that the strength of the vortex in the aneurysm peaks. A large vortex eddy is present near the distal wall of the aneurysm, and the simulations agree well with the experiments. Figures 4.3c and 4.3d show results during the diastolic phase and at the initial phase of the pulse cycle, respectively. The flow field travels straight through the artery, and there is a small vortex near the center of the aneurysm sac. The experiments and the numerical simulations also agree well for these two phases.

In addition to the velocity vectors and vorticity contours for the entire field in Fig. 4.3, Fig. 4.4 compares local experimental and numerical u -velocity profiles in the $x - y$ centerplane ($z = 0$) at x -locations of 3 mm, 10 mm, and 17 mm, representing locations upstream of, at the center of, and downstream of the aneurysm. Pulse phases of 40° , 60° , 240° , and 360° are shown. All four phases show very good qualitative agreement between the profiles at all three locations and demonstrate the ability of CFD simulations

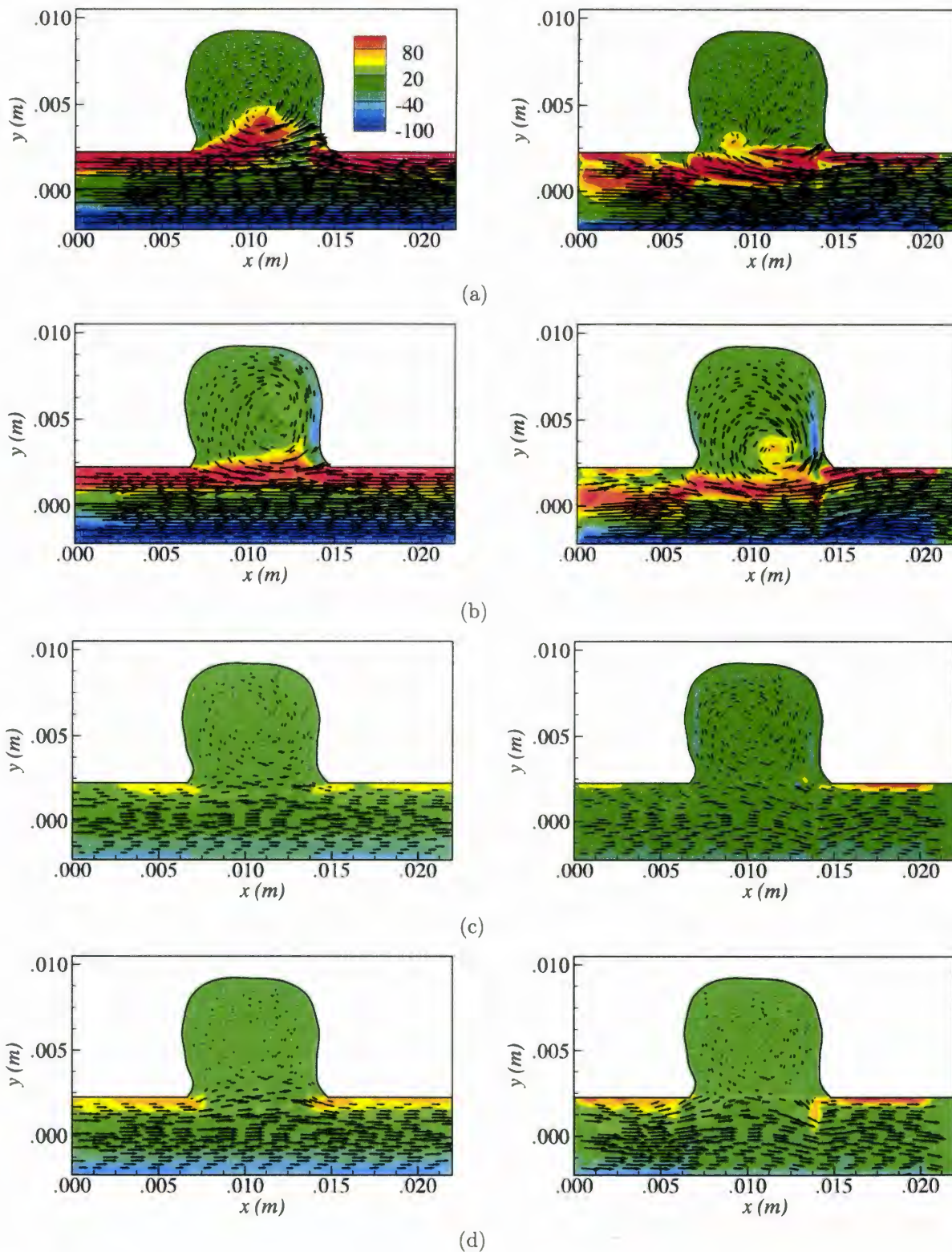


Figure 4.3 Velocity vectors superimposed on spanwise vorticity contours (1/s) for simulations (left frames) and microPIV experiments (right frames) at pulse phases of (a) 40°, (b) 60°, (c) 240°, and (d) 360°.

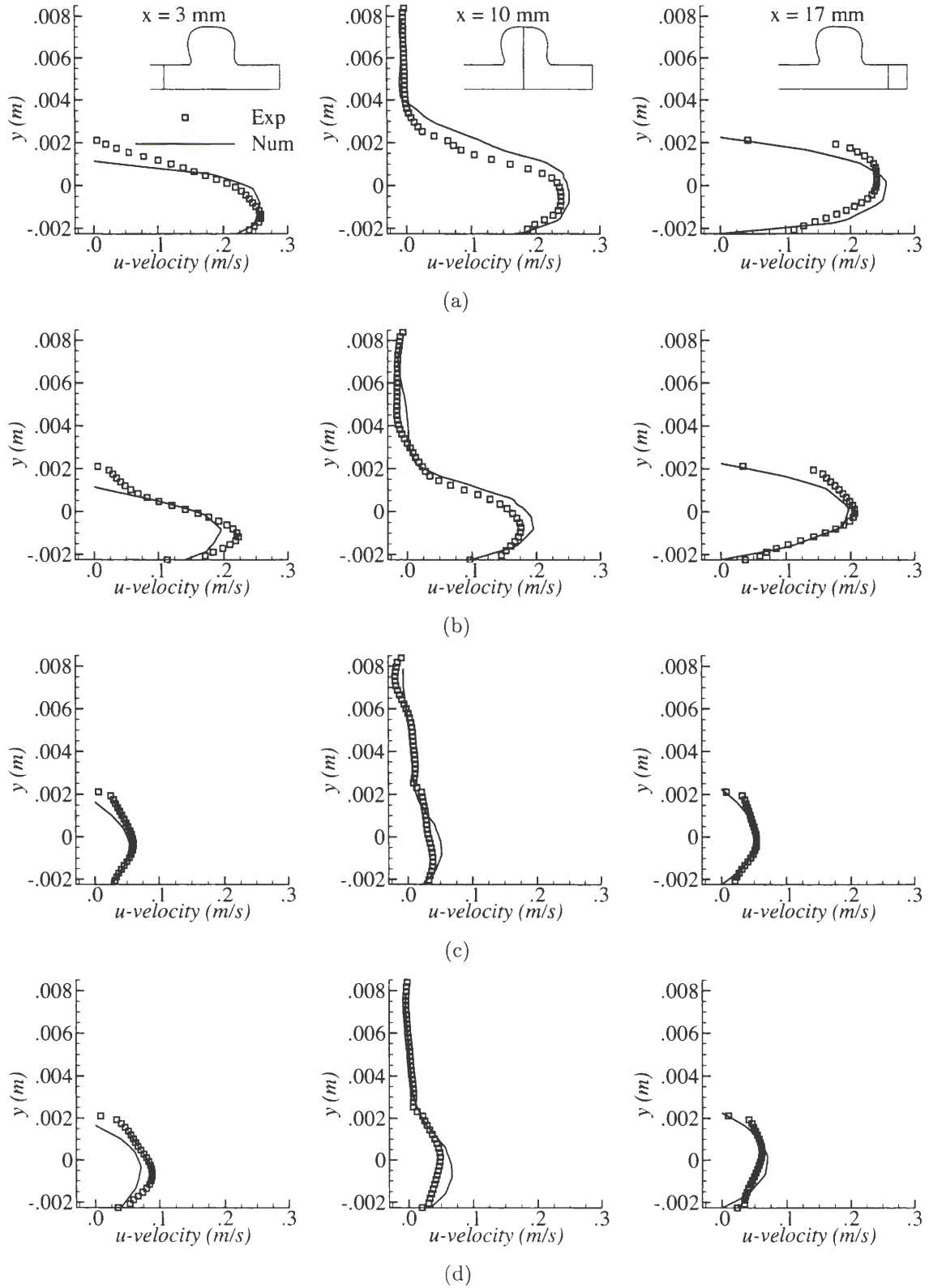


Figure 4.4 u -velocity profiles for simulations and experiments downstream of, at the center of, and upstream of the aneurysm at pulse phases of (a) 40° , (b) 60° , (c) 240° , and (d) 360° .

to accurately reproduce experimental flow.

Small discrepancies between between the experimental and numerical profiles are likely due to difficulties in measuring the experimental velocity data. Even with microPIV it is difficult to accurately measure data near the system's walls. The large curvature of the aneurysm model may have caused optical distortions, and the indices of refraction of the working fluid (water) and the aneurysm model did not match exactly. Additionally, the microPIV data was originally captured in four separate pieces that were later joined together. This process may have introduced some errors in properly aligning the vectors for each piece.

The discrepancy at 40° as shown in Fig. 4.3a is most likely due to a difference in wall conditions between the experiments and the numerical simulations. The experiments featured a model with elastic walls capable of stretching and temporarily deforming. During the experiments, the diameter of the aneurysm sac expanded and contracted by a few percent over the course of the pulse cycle. The numerical simulations were unable to reproduce this conditions because FLUENT constrains boundaries as rigid walls. In spite of the observed discrepancy, the velocities and vorticities are in good agreement at other pulse cycle phases. More importantly, the numerical simulations were able to recreate the motion of the primary vortex seen in the experimental model, leading to the conclusion that the variation in vortex position over time is a function of pulsatile flow conditions, and not the presence of elasticity in the wall material. These findings are in agreement with the results of previous numerical simulations [61, 62, 63, 64] that also showed the development of a vortex that varied in position and intensity during the pulse cycle.

Oscillating wall shear stress is an important phenomenon in intracranial aneurysm flow that correlates with aneurysm rupture [33]. Finol and Amon [63] used a numerical model to show that the temporal evolution of the vortex influenced oscillatory wall shear stress (WSS) and WSS gradients along aneurysm sac walls. The highest levels

of WSS and WSS gradients were obtained along the distal end of the sac wall when the arterial flow velocity was at its peak. Although Finol and Amon's model used a two-aneurysm geometry, other researchers have noted similar results in single-aneurysm geometries. Fukushima, Matsuzawa, and Homma [62] noted that the distal end is the most frequent site of rupture. They supported this conclusion by demonstrating high vorticity-induced WSS along the distal sac wall with a numerical model and suggested that fluctuations in wall shear and pressure may be associated with aneurysm growth in the distal direction. The present research correlates well with Fukushima's conclusions by showing cyclical vortex position and intensity accompanied by a strong vortex near the distal aneurysm sac wall during peak arterial velocity. Figure 4.5 shows WSS contours within the aneurysm and artery at various pulse phases. As the arterial inlet velocity increases, WSS along the distal sac wall rises, reaching a maximum of 0.52 N/m^2 during the pulse cycle's peak inlet velocity at 40° .

The variations in vortex intensity within the aneurysm can be explained by the pressure gradients between the artery and the aneurysm. Figure 4.6 displays pressure contours in the $x - y$ centerplane ($z = 0$) at 40° , 60° , 240° , and 360° . Figure 4.7 shows local pressure profiles and v -velocity profiles across the aneurysm neck for these same four phases. The weaker vortices in the aneurysm at 240° and 360° correspond to small pressure gradients, while the strong vortex at 40° corresponds to a much larger gradient. The profiles in Fig. 4.7 show that the phases with strong vortices have greater neck pressure gradients and elevated v -velocity near the distal aneurysm wall. At low velocities, the pressure gradient is small and flow tends to enter the aneurysm and form a vortex near the center of the sac. At higher velocities, the large pressure gradients between the sac and the artery cause the vortex to move towards the distal sac wall.

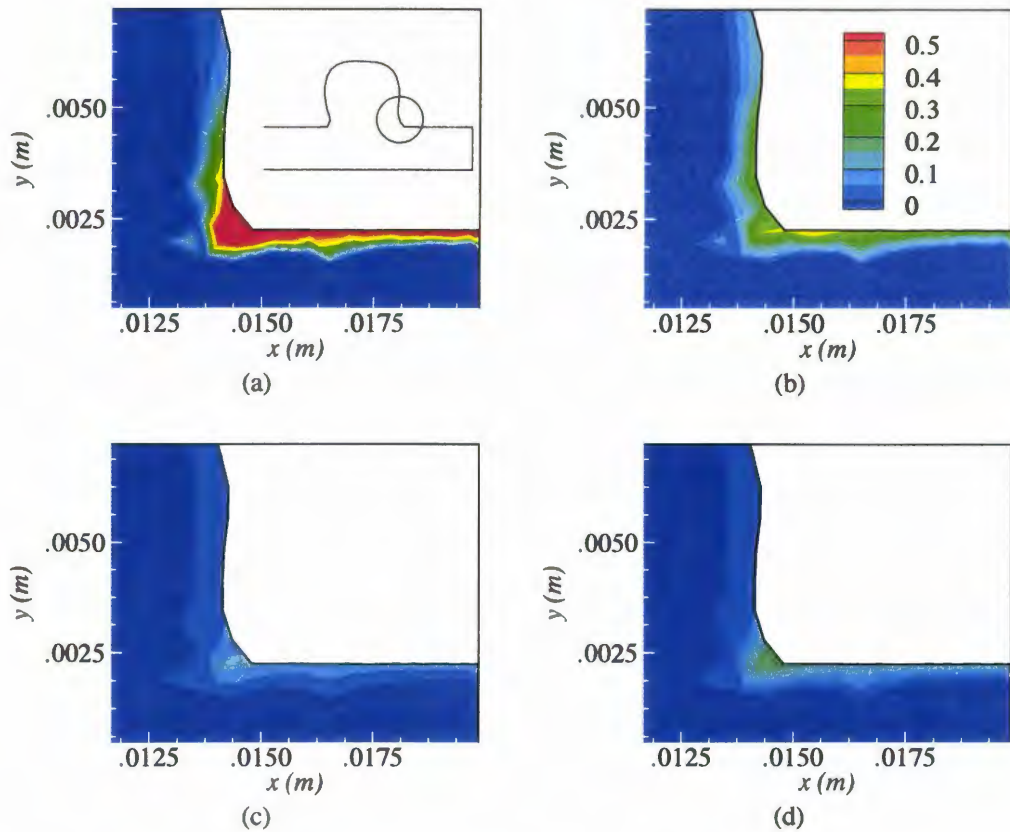


Figure 4.5 Contours of wall shear stress (N/m^2) near the distal aneurysm sac wall at pulse phases of (a) 40° , (b) 60° , (c) 240° , and (d) 360° .

4.4.3 Summary of aneurysm results and conclusions

Overall, the numerical simulations compare well with the microPIV experiments and provide confidence that simulations can be used to further examine flow behavior within intracranial side-wall aneurysms. Of particular interest is the potential use of numerical simulations to predict the success of ESO procedures. The use of simulations is a relatively inexpensive, safe, and noninvasive method that can be used as a diagnostic tool. Furthermore, simulations can provide continuous, detailed flow field information that is often difficult to obtain from *in vitro* experiments. For example, the full three-dimensional velocity and pressure fields can be predicted via numerical simulations, whereas traditional experiments only provide velocity fields in two-dimensional planes.

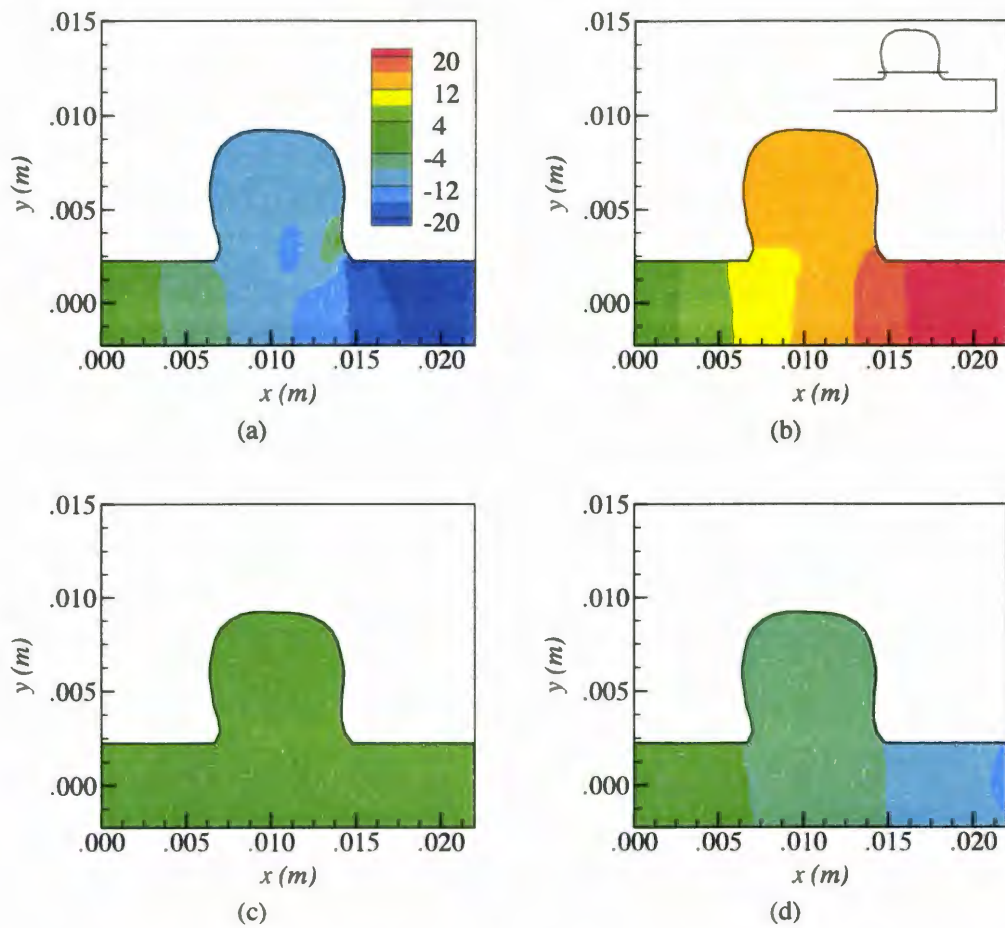


Figure 4.6 Pressure contours (Pa) at pulse phases of (a) 40°, (b) 60°, (c) 240°, and (d) 360°.

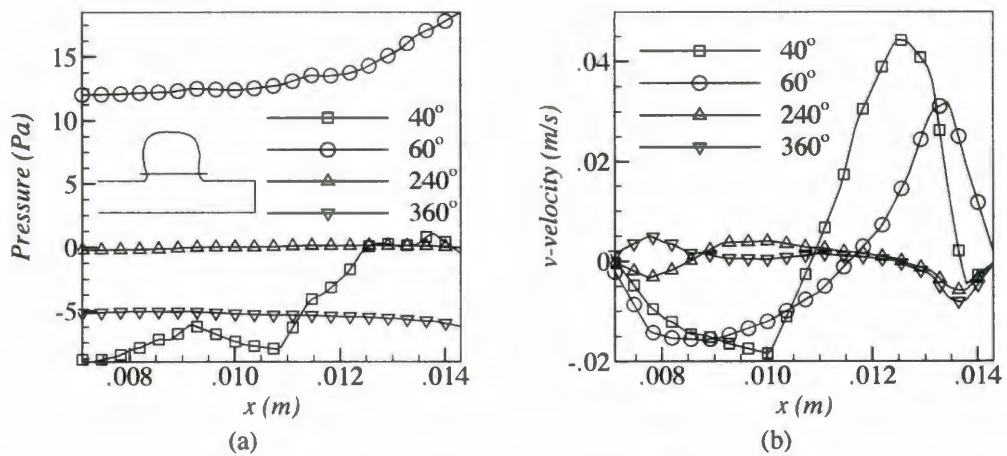


Figure 4.7 (a) Pressure profiles and (b) v -velocity profiles across the aneurysm neck at pulse phases of 40°, 60°, 240°, and 360°.

CHAPTER 5 SIMULATIONS OF STENT RECONSTRUCTION

The following sections detail the boundary conditions, initial conditions, grid resolution tests, and final simulation results of the aorta-iliac bifurcation simulations. Details on the cell size, time step size, working fluid, and computational performance are also included.

To investigate the effects of stent geometry on flow patterns in the aorta-iliac bifurcation, simulations were conducted to examine stent presence (no stents, one stent, or two stents), stent mismatch, and stent permeability. For each of these simulations, pressure and velocity data for the full computational domain were acquired every 10 time steps for one complete pulse cycle.

5.1 Boundary and Initial Conditions

The stent reconstruction simulations used five types of boundary conditions. The aorta inlet, shown at the top of Fig. 3.5, was specified by a velocity inlet. All simulations featured the pulsatile inlet velocity shown in Fig. 5.1. The waveform in Fig. 5.1 was based on data provided by The University of Iowa Hospital (Iowa City, IA). The profile in Fig. 5.1 was constructed from 37 discrete phase-velocity points. The left and right iliac outlets, shown as the outlets of the smaller vessels in Fig. 3.5, were specified as outflow boundaries. The radial aorta and iliac surfaces were specified as stationary walls with a no-slip condition.

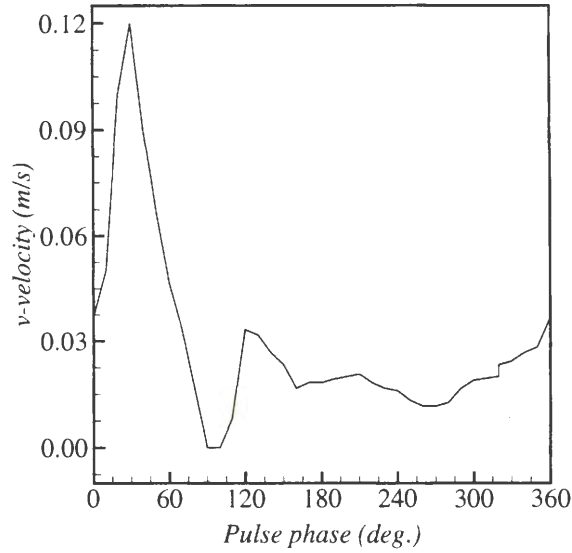


Figure 5.1 Inlet boundary condition used in the numerical simulations of blood flow in the bifurcation.

The Reynolds number for the velocity waveform in Fig. 5.1 was defined as:

$$Re = \frac{\rho v D}{\mu} \quad (5.1)$$

where ρ and μ are the fluid density and viscosity, v is the magnitude of fluid velocity at the aorta inlet, and D is the aortic diameter. For the waveform in Fig. 5.1, Re varied between zero and 602.

Preliminary stent reconstruction simulations using the outflow iliac boundaries revealed that the flow reversed at the iliac outlets beginning near the pulse phase of 30°. Initially the flow only reversed on a few cell faces of the outlets. As the pulse cycle slowed from its peak at 30°, the number of cell faces exhibiting reversed flow increased until the reversal was eliminated when inlet velocity became relatively steady during the last half of the pulse cycle. Altering the inlet velocity profile to include more discrete points failed to eliminate or reduce the reversed flow. Flow reversal also appeared irrespective of the inlet velocity profile being either plug or fully developed flow.

After further investigation, the reversed flow was attributed to the outflow boundary

conditions as they attempted to compensate for instantaneous changes in mass flow rate at the aorta inlet. Post-processing of the preliminary data boundaries revealed that flow reversal occurred only along artery walls. The magnitude of the reversed flow velocity was at least one order of magnitude smaller than the velocity at other outlet faces.

In a real aorta-iliac bifurcation, it is unlikely that the flow would reverse, especially because real iliacs are significantly longer (approximately 700 mm) and diverge into many smaller arteries. To determine if the reversed flow at the iliac outlets would influence flow near the stents, a simulation was run with the iliac lengths extended to 300 mm. Recall that the original iliac length was 30 mm. Figure 5.2 shows velocity profiles across the left iliac exit cross-section at $z = 0$ for the short iliac and long iliac simulations. The velocity profiles in Fig. 5.2 match almost identically (maximum difference is less than 0.1%). It was therefore concluded that the reversed flow at the iliac outlets did not adversely affect upstream flow. The original iliac length (30 mm) was used for all following simulations. Also, because other researchers have also noted reversed flow in stented arteries even when using inlet velocity waveforms that never drop below zero [40], the reversed flow in these simulations may not be entirely unrealistic.

In addition to the presence of reversed flow, preliminary stent reconstruction simulations were very computationally expensive and required nearly a week of real time to converge over an entire pulse cycle. The simulations also required considerable memory for data storage due to the large number of cells present in the model. To reduce computational expense, the presence of symmetric flow was investigated. Figure 5.3 shows contours of velocity normal to the $x - y$ centerplane, time-averaged over a complete pulse cycle.

Figure 5.3 demonstrates that the normal velocity in this plane was very nearly zero. Normal velocity magnitudes were on the order of 10^{-5} m/s. Since flow symmetry requires zero normal velocity in the plane selected for symmetry, the use of symmetry in the 3D model at the $x - y$ centerplane was therefore appropriate and was employed in

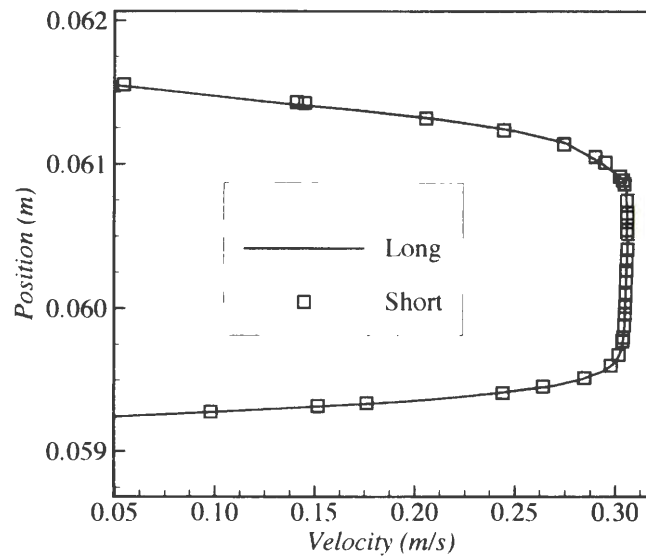


Figure 5.2 Profiles of normal velocity across the left iliac diameter at $z = 0$ for the 30 mm (short) and 300 mm (long) iliac length simulations.

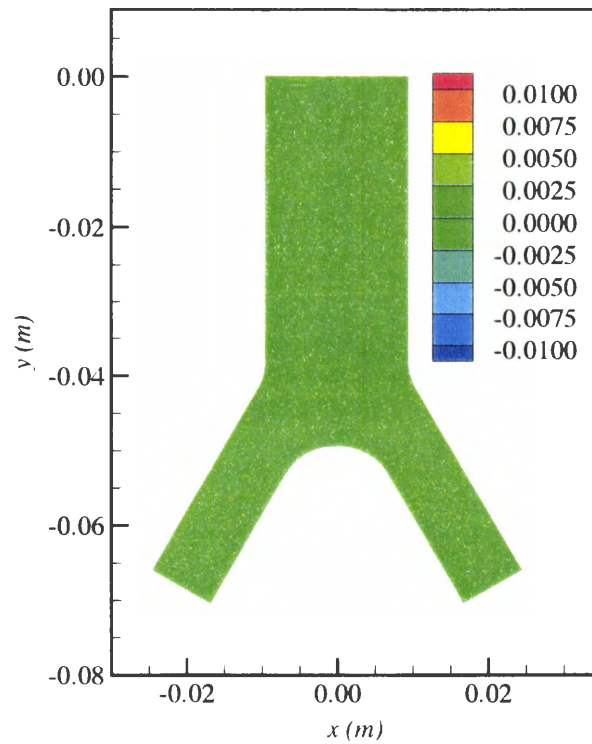


Figure 5.3 Time-averaged contours of velocity (m/s) normal to the $x - y$ centerplane in the full 3D bifurcation model.

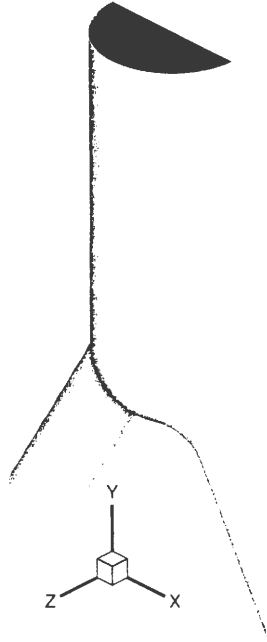


Figure 5.4 Geometry for the aorta-iliac bifurcation with symmetry in the $x - y$ centerplane. Created using GAMBIT.

all following simulations to reduce CPU expense and data storage requirements. The bifurcation geometry with symmetry imposed, shown in Fig. 5.4, also featured symmetry in the $x - y$ centerplanes for the stent volumes.

Finally, the surfaces of the stent geometries, shown by the small darkened tubes in Fig. 3.6, were specified as porous jump boundaries. Porous jumps are used to model thin membranes through which fluid pressure and velocity change. The membrane has a finite thickness over which the pressure change is defined by a combination of Darcy's Law and an additional inertial loss term [51]:

$$\Delta p = -\left(\frac{\mu}{\alpha}v + \frac{1}{2}C_2\rho v^2\right)\Delta m \quad (5.2)$$

where α is the permeability of the medium, C_2 is pressure-jump coefficient, and Δm is the thickness of the medium. In laminar flows through porous media, the pressure drop is generally proportional to velocity; C_2 can be set to zero and Eq. 5.2 reduces to:

$$\Delta p = -\left(\frac{\mu}{\alpha}v\right)\Delta m \quad (5.3)$$

FLUENT incorporates Eq. 5.3 on the faces of cells by using the velocity component normal to the medium face to calculate the pressure drop across the cell face, which in turn influences the pressure and velocity in cells surrounding the medium. Determination of α is an important step in ensuring the accuracy of the flow model. Using tabulated experimental data for fibrous metallic mats, α was defined as a function of the solid volume fraction and fiber diameter of the stent. Jackson and James [58] compiled a list of dimensionless permeabilities for laminar flows through fibrous porous media. The dimensionless permeability was defined as:

$$\frac{\alpha}{a^2} = f(B) \quad (5.4)$$

where a is the stent fiber diameter and B is the volume fraction of solid material in the porous medium. Jackson and James [58] presented $f(B)$ as a set of experimental data points and listed B values for many variations in fiber material, fiber diameter, flow rate, and working fluid. Typical B values for stents range between 0.2 and 0.4 and corresponded to a permeability on the order of 10^{-8} m^2 . Stent inlet and outlet boundaries were specified with a very large permeability ($\alpha = 10^{10} \text{ m}^2$) such that the flow did not experience a pressure drop of any significant degree as it crossed these boundaries.

All stent reconstruction simulations were initialized to quiescent flow conditions; pressure and all velocity components were initialized to zero.

5.2 Grid Resolution and Working Fluid

Stented bifurcation geometries were created with GAMBIT and meshed with approximately 700,000 cells. Stent reconstruction meshes were created using GAMBIT on Iowa State University's College-Level Unified Environment Network on a SunFire V480 with four 900 MHz UltraSparc III-Cu processors and 16 GB of memory [59]. The system required approximately 45 minutes to generate the 700,000-cell aneurysm mesh.

Table 5.1 Mesh convergence studies for coarse (3), medium (2), and fine (1) bifurcation meshes. Superscript notation refers to a comparison between two meshes. ϕ_A = velocity magnitude at $(x, y, z) = (0, -30.0, 0)$ mm. ϕ_B = velocity magnitude at $(x, y, z) = (15.6, -59.6, 0)$ mm.

Grid	N_{cells}	ϕ_A (Pa)	ϕ_B (m/s)
Coarse (3)	13508	0.1146	0.2918
Medium (2)	103138	0.1175	0.3065
Fine (1)	714503	0.1179	0.3106
Apparent order (p)		2.76	1.82
Approximate (a) relative error			
e_a^{32}		2.47%	4.79%
e_a^{21}		0.36%	1.34%
Extrapolated (ext) relative error			
e_{ext}^{32}		0.42%	1.86%
e_{ext}^{21}		0.06%	0.53%
Grid convergence index			
GCI_{medium}^{32}		0.53%	2.36%
GCI_{fine}^{21}		0.08%	0.66%

The mesh was validated using the same GCI method as used for the aneurysm mesh. Table 5.1 compares flow velocity upstream and downstream of a stent for three successively finer meshes and indicates that the 700,000-cell mesh was sufficient for relatively grid-independent solutions.

The working fluid in the stent reconstruction simulations was based on properties representative of human blood ($\rho = 1060 \text{ kg/m}^3$, $\mu = 4$ centipoise). The density, viscosity, and Newtonian assumption were consistent with aortic blood properties indicated in the reviewed literature [15].

5.3 Computational Performance and Post-Processing

Fluid dynamics simulations were performed on an Intel Xeon cluster at Iowa State University's High Performance Computing Center. The cluster features 44 nodes each with dual 2.8 GHz Intel Xeon processors and 2 GB of memory. Each processor has a 400 MHz front-side bus for a maximum memory bandwidth of 3.2 GB/s [60]. All

simulations in this research were performed by running FLUENT in parallel on one node of this cluster.

Because the computers used to run the simulations limited jobs to 144 CPU hours per job, a time step size of 0.002 s was used for all bifurcation simulations to allow for time-averaged data from a full 1-s pulse cycle to be contained within a single output data file. The stability of FLUENT's implicit solution method is independent of time step size and it can be arbitrarily selected. The cluster required approximately 120 hours of CPU time to reach converged solutions for the bifurcation simulations. Convergence within each time step was attained for all simulations when scaled residuals for pressure and velocity each dropped by at least three orders of magnitude.

The output data files for each simulation were re-loaded into FLUENT. Since FLUENT stores a very large amount of information in its data files, the output data was post-processed to include only the pressure, velocity, and wall shear stress in surfaces of interest. Post-processed data files were visualized using Tecplot version 10 (Tecplot Incorporated, Bellevue, WA)

5.4 Simulation Results

The results of the stent reconstruction simulations are presented in this section. Figure 5.5 shows a sketch of the stent reconstruction geometry with the five planes selected for data analysis. "Stent inlet" is an $x - z$ plane at $y = -30.5$ mm. It is located just above the stent inlets. "Thru stent inlet" is an $x - z$ plane at $y = -35.5$ mm that passes through the portions of the stents that protrude into the aorta. "Thru stent base" is an $x - z$ plane at $y = -47.5$ mm, located near the aortic bifurcation. "Thru stent outlet" is offset 5 mm upstream from the stent outlet plane. "Stent outlet" is aligned with and located near the stent outlet in the right iliac. These five planes will be referenced frequently in the following discussions.

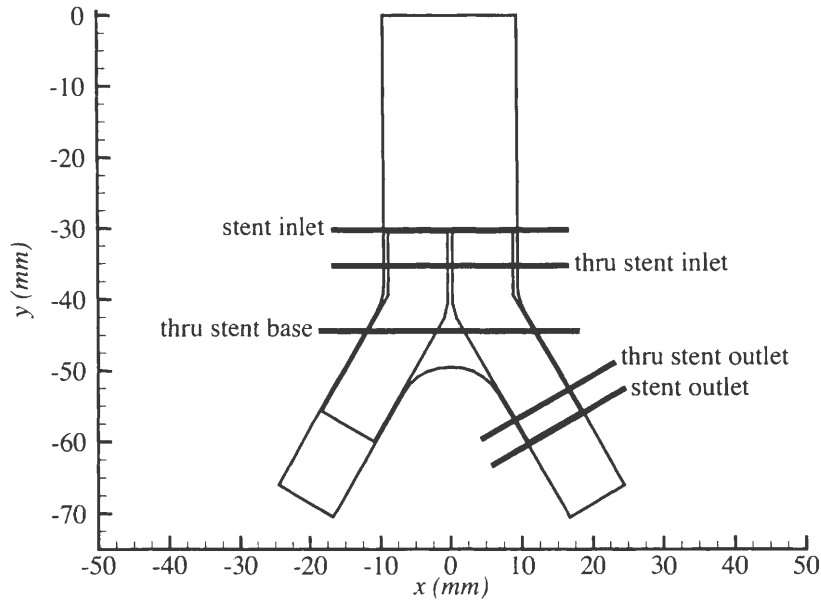


Figure 5.5 Sketch of the stent reconstruction geometry with five planes of interest labeled.

Two additional definitions are needed before proceeding further. “Spanwise vorticity” will refer to the z -component of vorticity (in the $x - y$ plane) and will be defined by:

$$\omega_z = \frac{\partial v}{\partial x} - \frac{\partial u}{\partial y} \quad (5.5)$$

“Streamwise vorticity” will refer to the y -component of vorticity (in the $x - z$ plane) and will be defined by:

$$\omega_y = \frac{\partial u}{\partial z} - \frac{\partial w}{\partial x} \quad (5.6)$$

5.4.1 Unstented simulation

The initial simulation featured an aorta-iliac geometry with no stents. This simulation was used to determine the general fluid mechanics present in the system. The unstented results were used as a baseline for comparison with further simulations.

The key flow phenomena of the unstented aorta-iliac system were variations in wall shear stress (WSS) and vorticity. The transient velocity inlet induced oscillations in

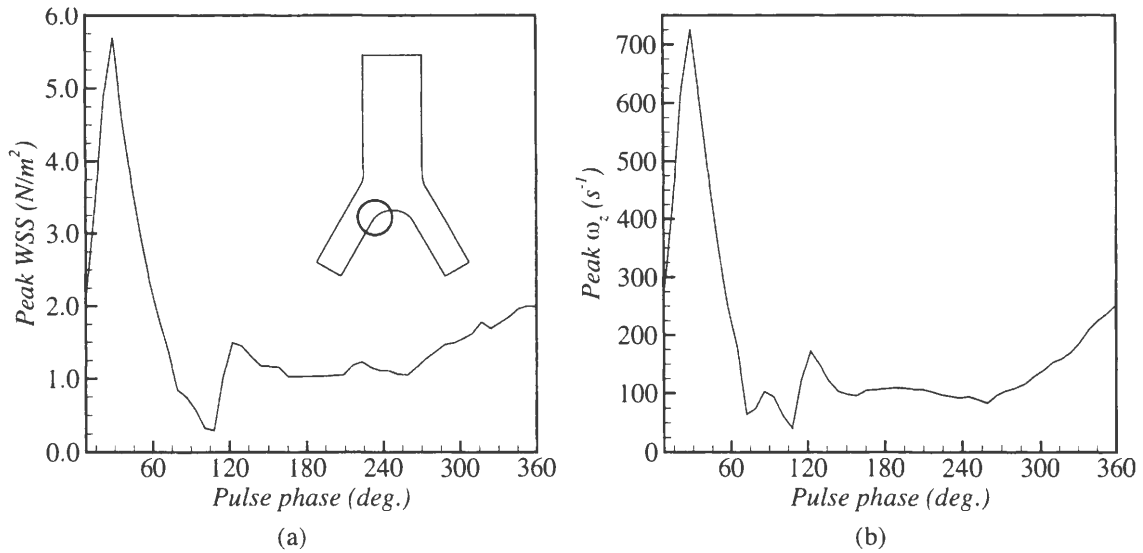


Figure 5.6 Peak values for (a) WSS and (b) spanwise vorticity, plotted versus the pulse phase. Peak values occurred along the artery wall near the bifurcation.

WSS and vorticity near the artery walls. Both maximum WSS and maximum spanwise vorticity were located near the artery wall where the aorta bifurcates into the two iliacs, medial to the iliac openings, in the $x - y$ centerplane ($z = 0$) irrespective of the pulse phase. This location is circled for one iliac in Fig. 5.6. In relation to the pulse phase cycle, maximum WSS ranged from a peak of 5.70 N/m^2 at 30° to a minimum of 0.30 N/m^2 at 150° . Maximum spanwise vorticity showed a similar relationship, with a peak of 726 s^{-1} at 30° and a minimum of 41 s^{-1} at 150° . Figure 5.6 shows maximum vorticity and WSS values plotted for each phase of the pulse cycle. Each plot followed a trend similar to the velocity inlet profile (Fig. 5.1).

Figure 5.7 shows contours of WSS and spanwise vorticity along the bifurcation wall near the peak inlet velocity phase of 30° . Note that both peak WSS and peak spanwise vorticity occurred at approximately the same location along the artery wall. Although only the 30° phase is shown, the peak values occurred at nearly the same location shown in Fig. 5.7 for all phases

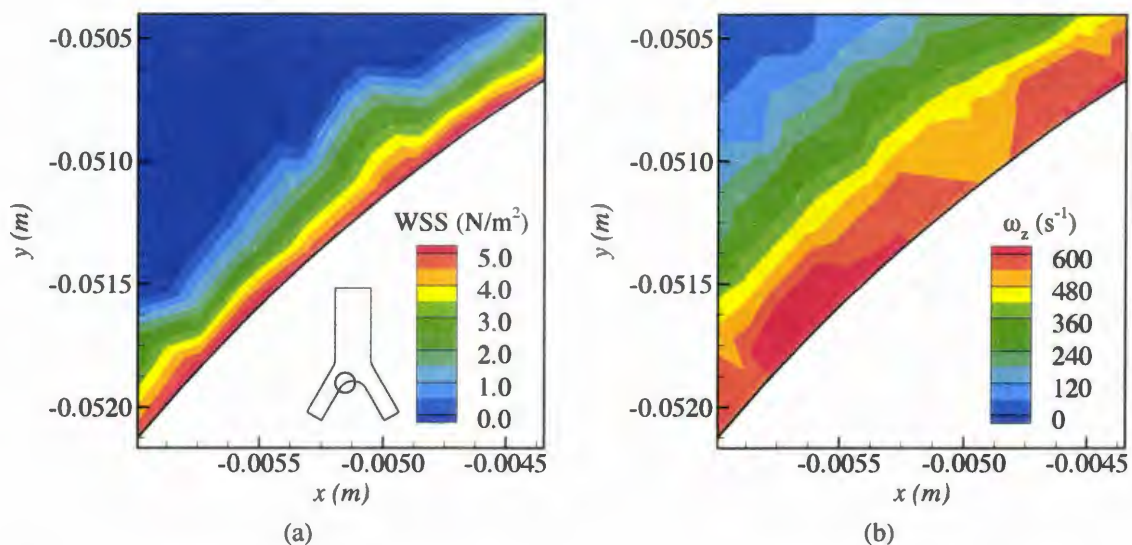


Figure 5.7 Contours of (a) WSS (N/m^2) and (b) spanwise vorticity (s^{-1}) near the bifurcation wall of the left iliac for a pulse phase of 30° .

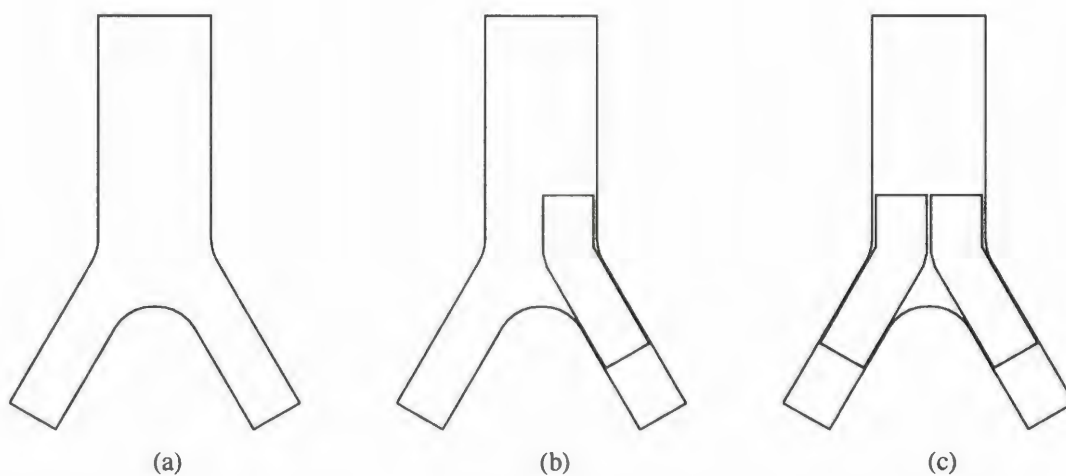


Figure 5.8 Sketches of the $x - y$ centerplanes for (a) no stents, (b) one stent, and (c) two stents.

5.4.2 Effects of stent presence

After the fundamental flow phenomena of an unstented aorta-iliac bifurcation were established, further simulations were conducted to determine how the presence of stents altered the flow. One simulation featured a stent inserted only in the right iliac while an additional simulation featured stents in both iliacs. Figure 5.8 shows a sketch of the unstented, one-stent, and two-stent cases.

It should be noted that many of the changes shown and discussed for the stent presence simulations were all taken from the pulse phase of 30° at which the inlet velocity was near its peak. It was during this phase of the pulse cycle that the most significant magnitudes of flow phenomena discrepancies appeared in comparison to the unstented case.

Data from the unstented, one-stent, and two-stent cases were analyzed in the five planes shown in Fig. 5.5 as well as the $x - y$ centerplane. The variables that best illustrated the differences in flow phenomena between the three cases were WSS, streamwise vorticity, and spanwise vorticity. Figure 5.9 displays the peak WSS in each of the six planes for the unstented, one-stent, and two-stent cases at four important pulse phases. As demonstrated by Fig. 5.9, changes in peak WSS due to stent presence were very small. Peak WSS in the stent inlet plane at 145° (Fig. 5.9a) increased by 5.96% between the unstented and two-stent cases, however the magnitude of the increase (0.0031 N/m^2) was very small. Changes in peak WSS at other planes and pulse phases were less than 1%. Peak WSS in the stent outlet plane (Fig. 5.9b) tended to decrease slightly (less than 1% change) at most pulse phases. The greatest change was seen in the $x - y$ centerplane at 90° (Fig. 5.9f), where peak WSS increased from 0.574 N/m^2 in the unstented case to 0.592 N/m^2 in both the one-stent and two-stent cases, an increase of 3.14%. In all three cases, the WSS peak was located near the bifurcation wall of the right iliac (see Fig. 5.7).

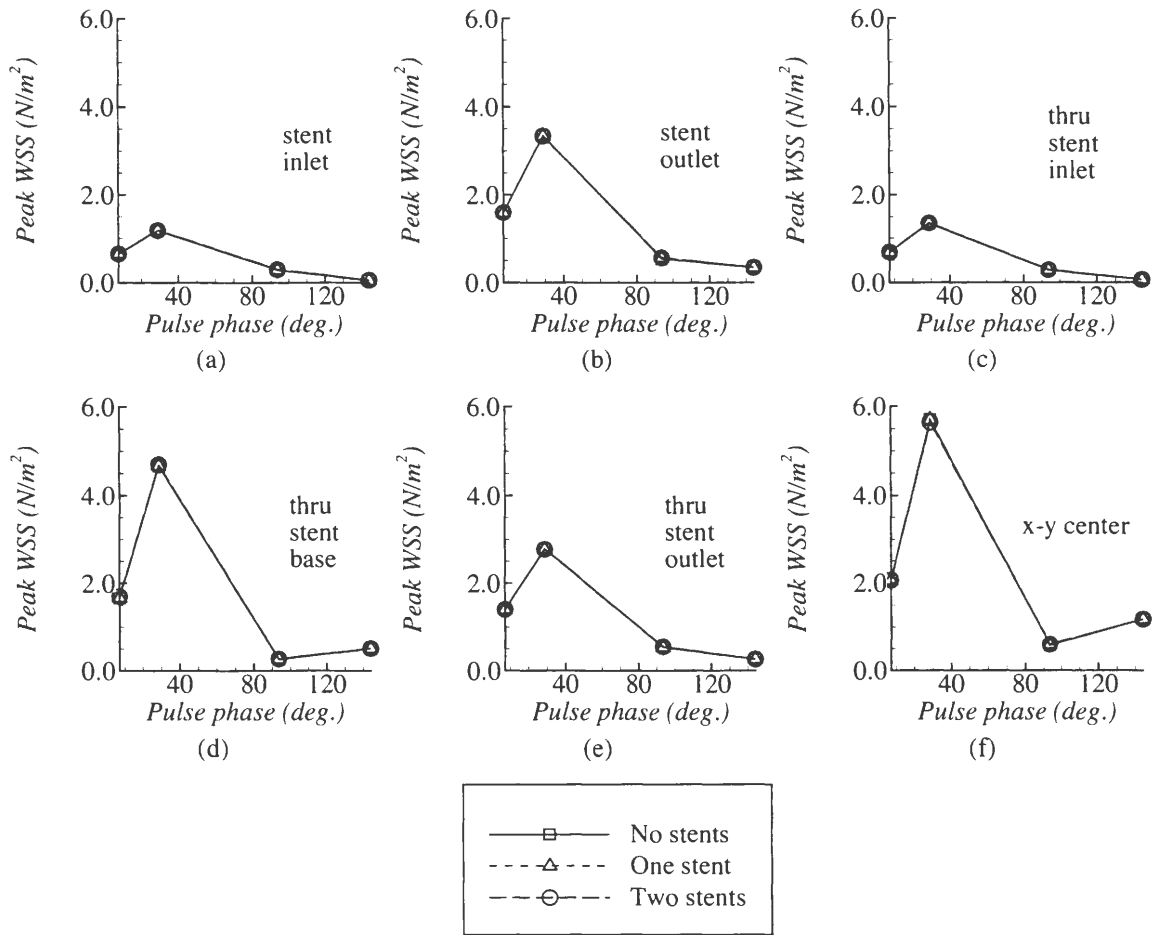


Figure 5.9 Peak WSS at four phase locations for the unstented, one-stent, and two-stent cases. Planes shown are (a) stent inlet, (b) stent outlet, (c) thru stent inlet, (d) thru stent base, (e) thru stent outlet, and (f) $x-y$ centerplane.

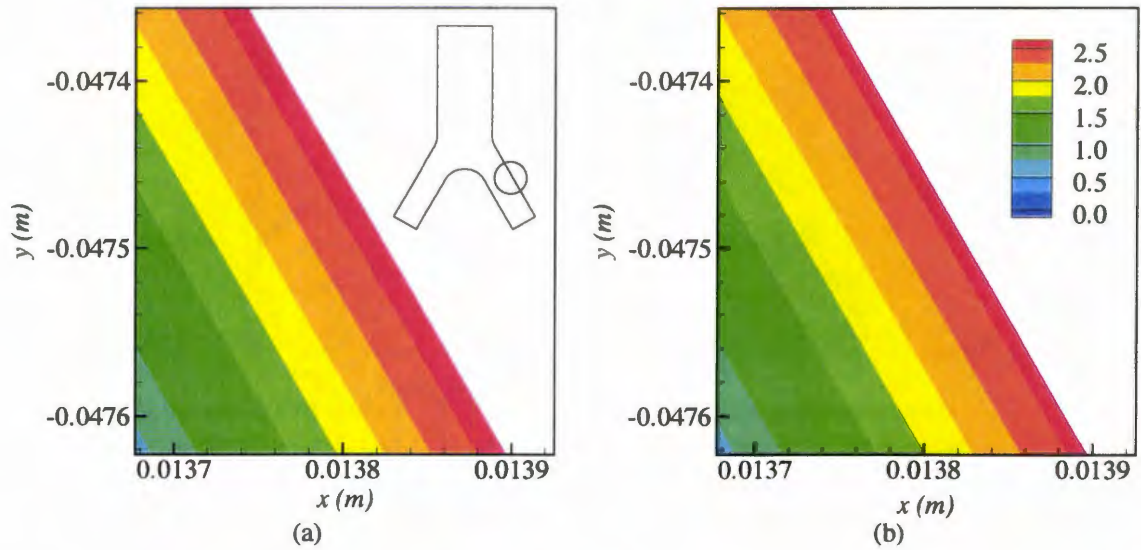


Figure 5.10 Contours of WSS (N/m^2) in the $x - y$ centerplane near the outer right iliac wall for (a) no stents and (b) two stents.

When in contact with the artery, stents are known to reduce WSS along the artery wall, a condition that promotes thrombus formation. Figure 5.10 displays contours of WSS along the right iliac wall in the $x - y$ centerplane for the unstented and two-stent cases. Note that the red region of maximum WSS is noticeably smaller in the two-stent simulation. Figure 5.10 demonstrates that the stent reconstruction simulations were successful in modeling the reduced wall shear condition observed in *in vivo* research [65].

Stent presence also had a small effect on spanwise vorticity. In most planes and pulse phases, changes in peak spanwise vorticity between the unstented and the one-stent and two-stent cases were less than 1%. In the $x - y$ centerplane, however, changes in spanwise vorticity were more significant. The greatest change in peak spanwise vorticity occurred in the $x - y$ centerplane near the 145° pulse phase. Peak negative spanwise vorticity decreased from 102.4 s^{-1} in the unstented case to 96.7 s^{-1} in the one-stent and two-stent cases, a decrease of 5.65%. At the 90° pulse phase, peak negative spanwise vorticity in the $x - y$ centerplane rose from 85.4 s^{-1} in the unstented case to 89.4 s^{-1} in the two-stent case, an increase of 4.68%. At other planes and pulse phases, changes in spanwise

Table 5.2 Summary of peak streamwise vorticity and changes in peak streamwise vorticity for unstented, one-stent, and two-stent simulations in the “thru stent inlet” plane at 30°. Percent changes are in relation to the unstented case.

Sim.	Peak CCW ω_y (s^{-1})	change	Peak CW ω_y (s^{-1})	change
Unstented	19.60	–	-16.25	–
One stent	19.68	0.41%	-17.88	10.03%
Two stents	21.31	8.72%	-17.97	10.58%

vorticity were typically under 2%.

Unlike the small changes seen in WSS and spanwise vorticity, stent presence introduced more significant changes in streamwise vorticity. Figures 5.11 and 5.12 display the peak negative (clockwise, CW) and positive (counter-clockwise, CCW) spanwise vorticity in each of the six planes for the unstented, one-stent, and two-stent cases at four important pulse phases. The most significant changes were found in the “thru stent inlet” plane (Figs. 5.11c and 5.12c) at a pulse phase of 30°. Table 5.2 summarizes the changes in peak streamwise vorticity at this plane and phase for each of the three stent presence cases. In the planes of the stent inlets and outlets, vortices initially formed during diastole (around 145°) and varied in magnitude over the rest of the pulse cycle.

Figure 5.13 compares contours of streamwise vorticity in the “thru stent inlet” plane for the unstented (Fig. 5.13a), one-stent (Fig. 5.13b), and two-stent (Fig. 5.13c) simulations. The first row shows the entire plane and stent cross-sections. Due to the symmetry boundary condition discussed in Sect. 5.1, the data in the first row of Fig. 5.13 were mirrored about the x -axis in order to depict the entire cross-section. The second row of Fig. 5.13 shows enlargements of the section near the right iliac to emphasize regions of high vorticity; this region is indicated by the small box on the right sides of frames in the first row. Similarly, the third row shows enlargements of the section near the left iliac; this region is indicated by the small box on the left sides of the frames in the first row. The presence of stents elevated both the magnitude of maximum vorticity and the size

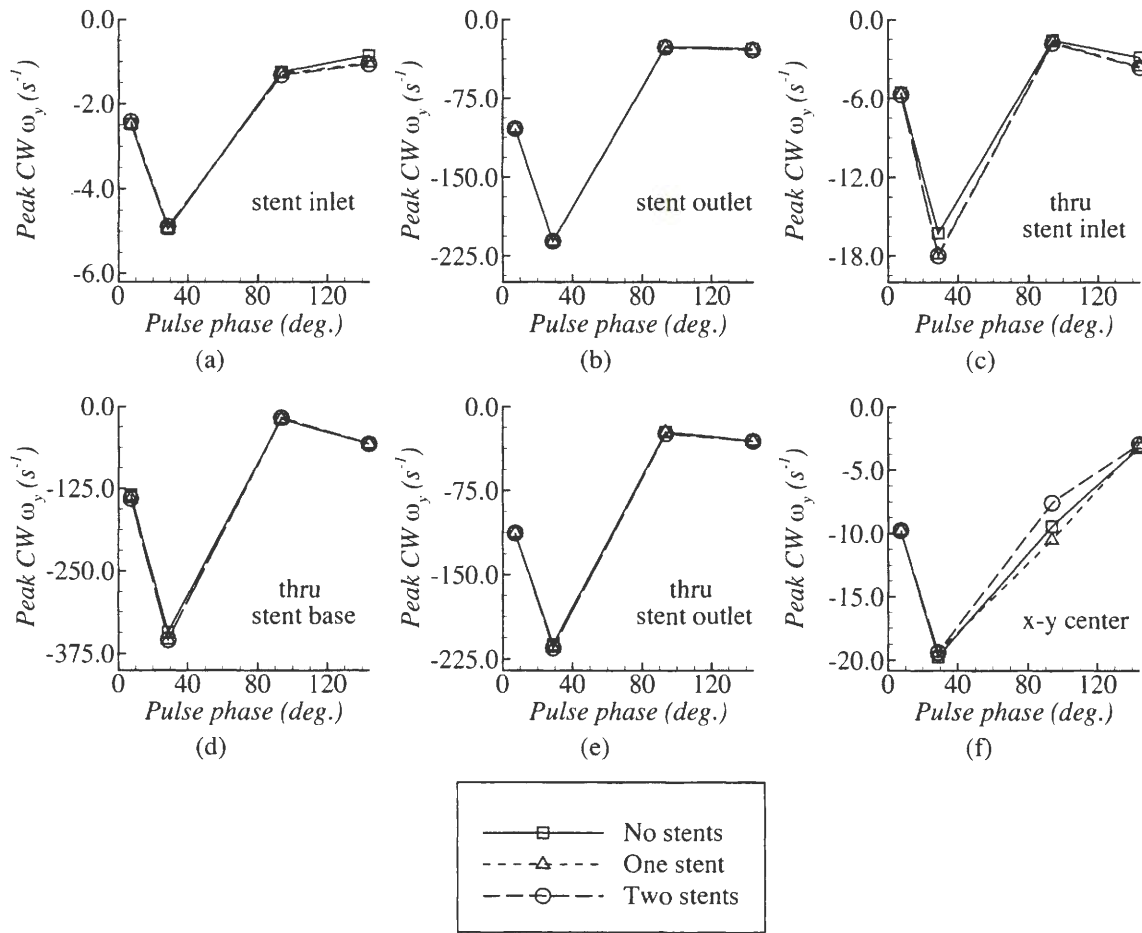


Figure 5.11 Peak negative streamwise vorticity in six planes of interest at four important phase locations for the unstented, one-stent, and two-stent simulations. Planes shown are (a) stent inlet, (b) stent outlet, (c) thru stent inlet, (d) thru stent base, (e) thru stent outlet, and (f) $x - y$ centerplane.

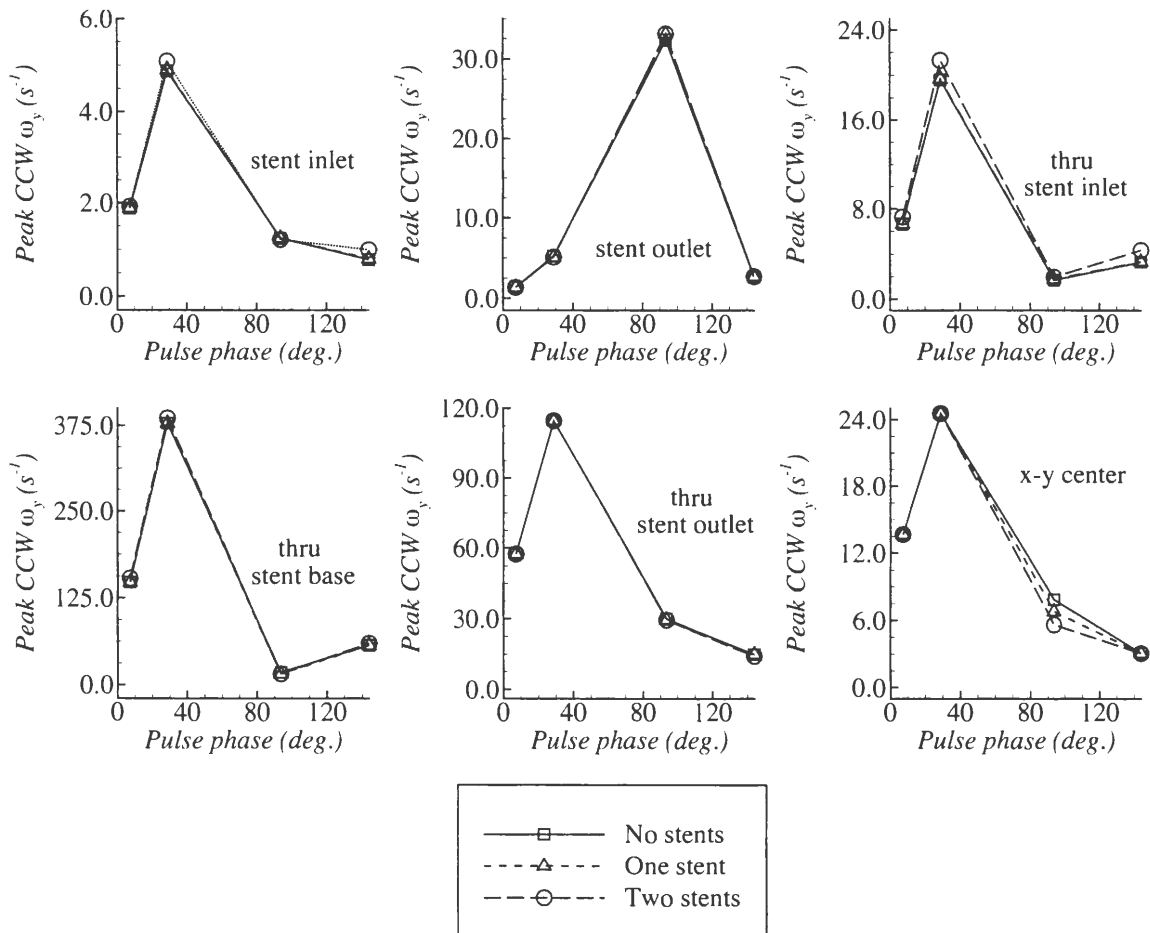


Figure 5.12 Peak positive streamwise vorticity in six planes of interest at four important phase locations for the unstented, one-stent, and two-stent simulations. Planes shown are (a) stent inlet, (b) stent outlet, (c) thru stent inlet, (d) thru stent base, (e) thru stent outlet, and (f) $x - y$ centerplane.

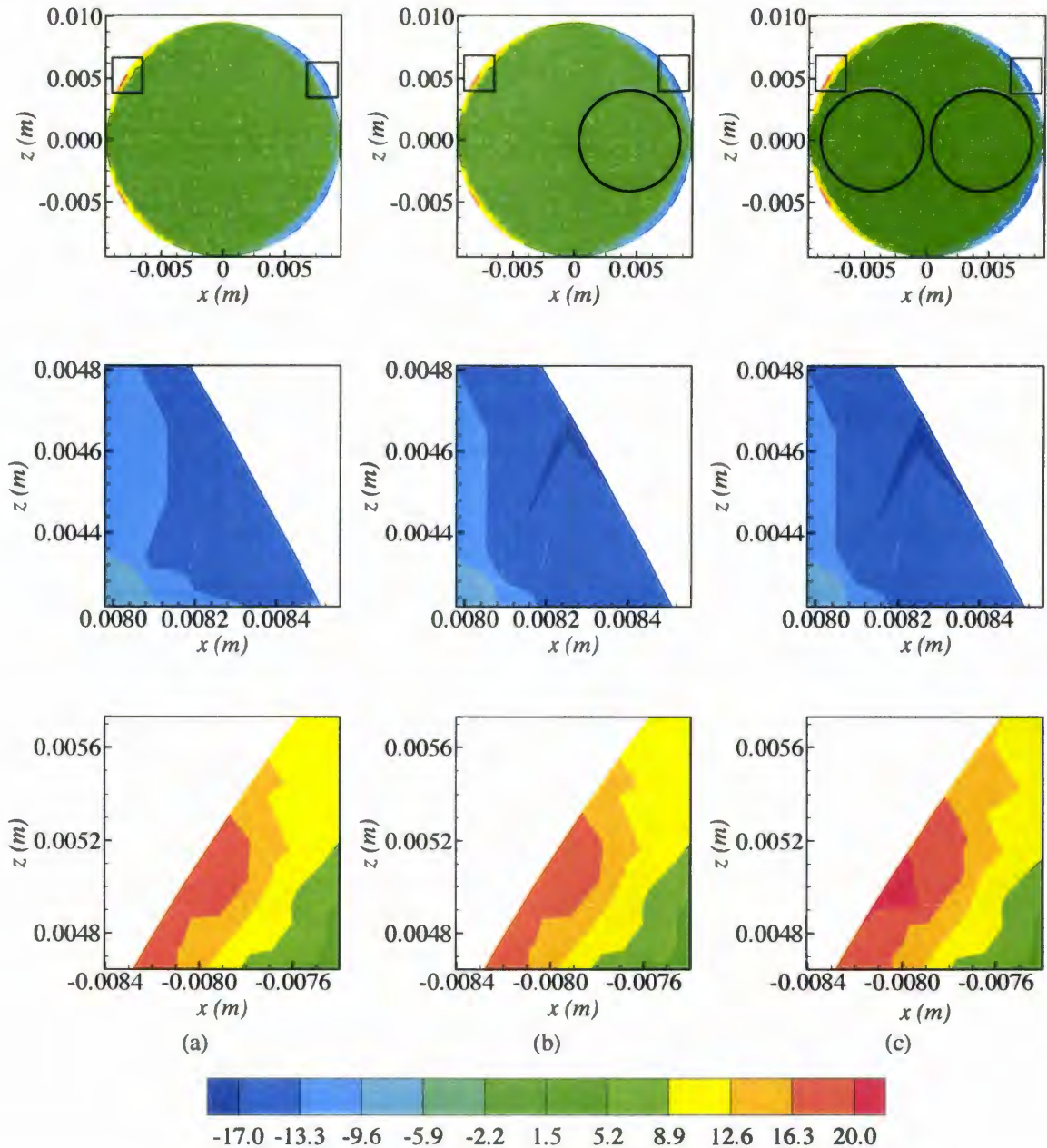


Figure 5.13 Contours of streamwise vorticity (s^{-1}) in the “thru stent inlets” plane at a pulse phase of 30° for (a) unstented, (b) one-stent, and (c) two-stent simulations.

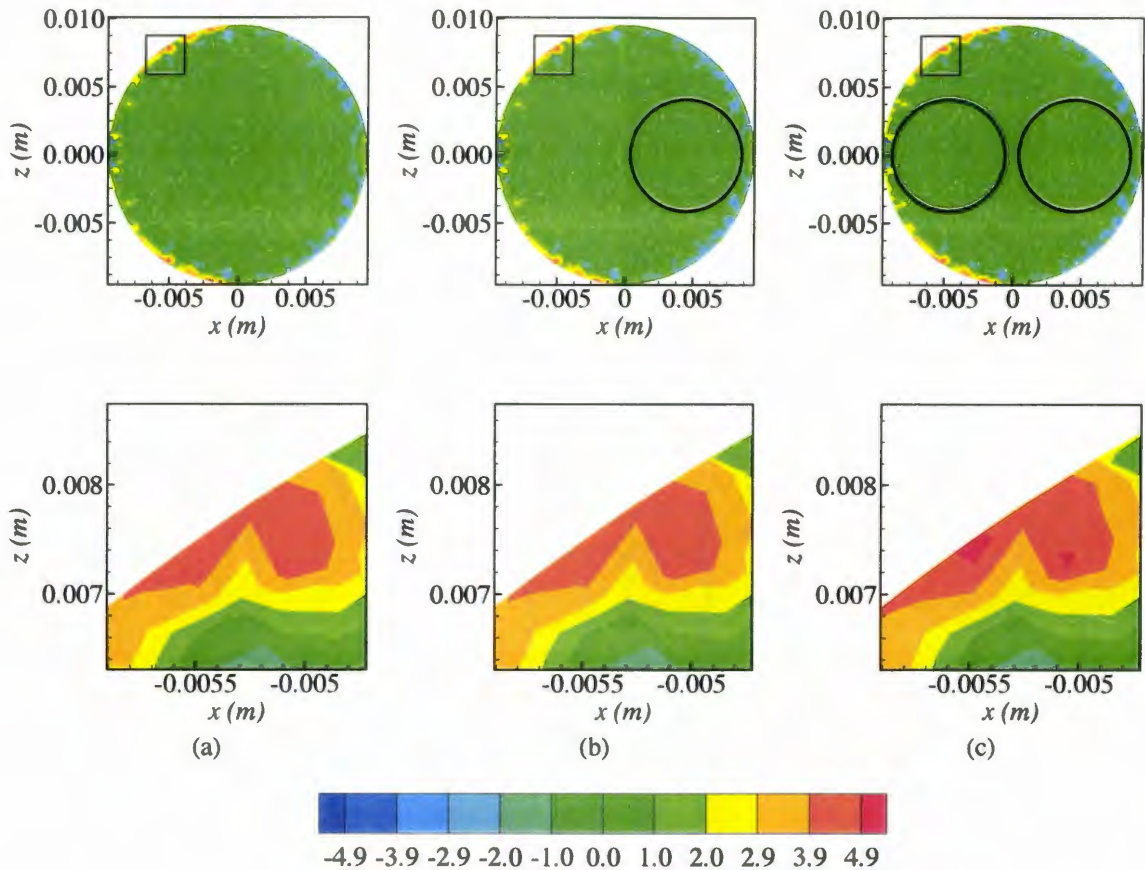


Figure 5.14 Contours of streamwise vorticity (s^{-1}) in the plane of the stent inlets at a pulse phase of 30° for (a) unstented, (b) one-stent, and (c) two-stent simulations.

of the region featuring high vorticity. Another notable feature in Fig. 5.13 is the lack of symmetry between the contours in the second and third rows for the no-stents and two-stent cases. While the magnitudes of streamwise vorticity in these frames were very similar, they were not identical as expected. The discrepancies between these frames were likely due to the unstructured grid required to mesh the 3D model.

Stents also introduced small changes in the maximum streamwise vorticity near stent inlets and outlets. Figures 5.14 and 5.15 display contours of streamwise vorticity in the planes of the stent inlets and outlets, respectively. In the plane of the stent inlets (shown in 5.14, located at $y = -30.5$ mm), maximum streamwise vorticity at 30° increased from

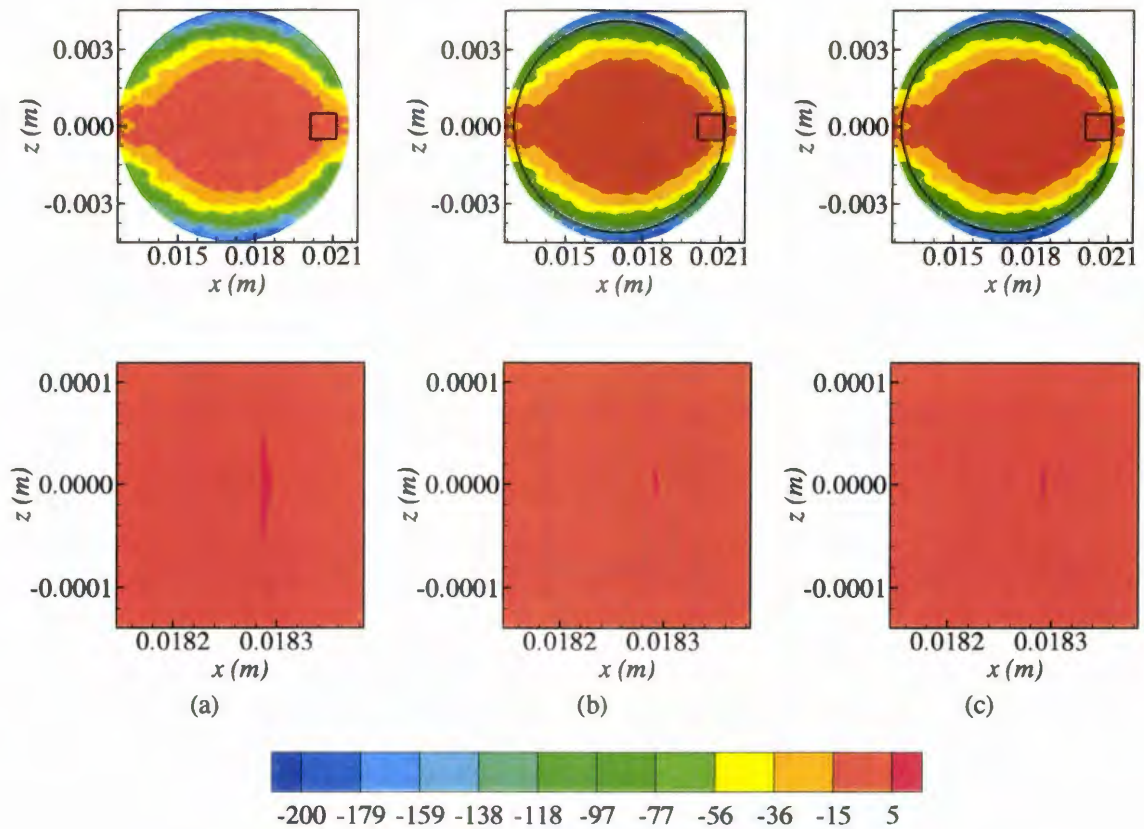


Figure 5.15 Contours of streamwise vorticity (s^{-1}) in the plane of a stent outlet at a pulse phase of 30° for (a) unstented, (b) one-stent, and (c) two-stent simulations.

4.88 s^{-1} in the unstented artery to 5.09 s^{-1} in the two-stent artery, an increase of 4.3%. The presence of one stent caused a very small (less than 1%) increase in maximum streamwise vorticity. In the plane of the stent outlets (5.15), both one-stented and two-stented arteries indicated a decrease in the maximum streamwise vorticity at 30° , from 5.25 s^{-1} in the unstented case to 5.11 s^{-1} in the stented cases, a change of 2.6%. As mentioned in the beginning of this subsection, the streamwise vorticity formed at the stent inlets and outlets during the diastole phase of the pulse cycle, near 145° .

Unfortunately, the implications of stent presence on vorticity in cardiovascular hemodynamics have not been well-documented. In general, stents have been shown to induce regions of elevated vorticity and flow separation near both the stent inlets and outlets

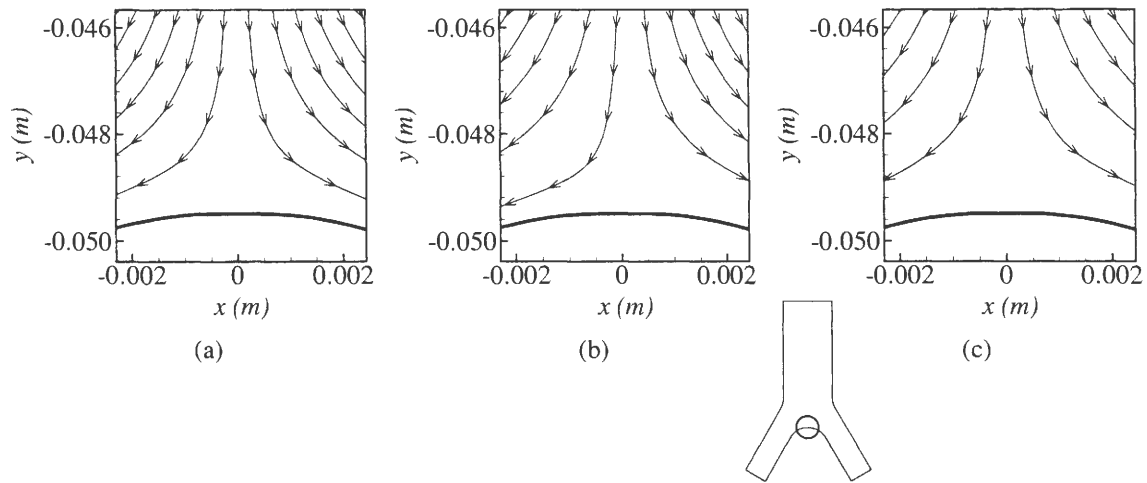


Figure 5.16 Velocity streamlines near the bifurcation wall for (a) unstented, (b) one-stent, and (c) two-stent simulations.

and form during diastole [41, 48]. The present results for streamwise vorticity appear to support the vorticity trends shown in these earlier studies, however the present results on spanwise vorticity are somewhat inconclusive.

Although many of the noted changes in WSS, streamwise vorticity, and spanwise vorticity introduced by the stents were small in magnitude, they may still be physiologically significant. A heart that pumps blood at a rate of 60 beats per minute will beat 3,600 times per hour and 86,400 times a day, meaning that any abnormalities will also appear 86,400 times a day. Therefore while a small change in a WSS peak at a particular instance in time may appear insignificant, it is important to understand that any change in a system with such frequent cycling can become significant over time.

Another phenomena introduced by the stents was an increase in aortic “dead space.” Dead space is the medical term used to describe the tendency for stents to discourage blood flow from reaching the artery wall near the bifurcation (at the distal end of the aorta). Over time, too much dead space will result in inadequate nutrient supply to the aortic bifurcation. Figure 5.16 shows velocity streamlines near the aortic bifurcation for simulations with no stents, one stent, and two stents. The region of dead space, taken

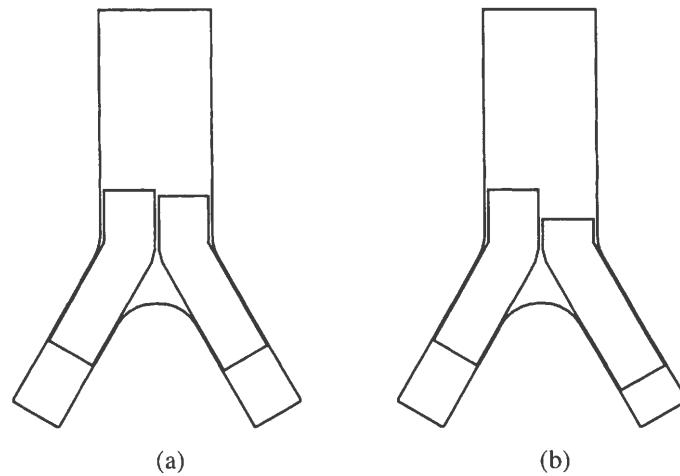


Figure 5.17 Sketches of the $x - y$ centerplanes for (a) small mismatch and (b) large mismatch.

here as the region untouched by a streamline, was increased by the presence of stents. Figure 5.16b clearly illustrates the effect of stent presence on flow near the bifurcation wall. Flow through the stented right iliac was further separated from the wall near the bifurcation and followed the curvature of the stent to a greater degree than flow through the unstented left iliac.

5.4.3 Effects of stent mismatch

Placing a stent in an artery is a delicate medical procedure. When placing a stent in each of the iliac arteries, aligning the stents so that they protrude equally into the aorta can be difficult even for an experienced surgeon. Simulations were conducted to determine the effects of stent mismatch, here defined as the level of mis-alignment of the stent protrusions into the aorta. One simulation featured a small mismatch where the stents were mis-aligned by only 1 mm, such that the right was inserted 1 mm further into its target iliac than the left stent into its target iliac as shown in Fig. 5.17a. A second simulation featured a large mismatch where the stents were mis-aligned by 5 mm, shown in Fig. 5.17b. Results were compared to the perfectly aligned two-stent case (Fig. 5.8c).

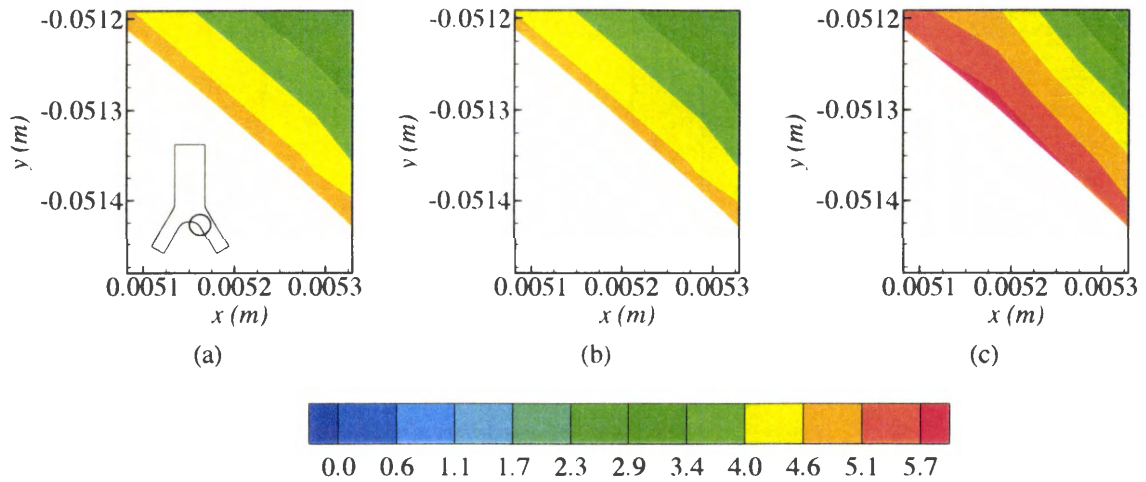


Figure 5.18 Contours of WSS (N/m^2) in the $x - y$ centerplane near the right bifurcation wall, at 30° , for (a) perfect alignment, (b) small mis-match, and (c) large mis-match. All three simulations featured two stents.

The most significant finding in the mismatch simulations was an elevation of WSS in the $x - y$ centerplane, along the wall closest to the bifurcation on the side of the right iliac, where the right stent was further inserted than the left stent. Figure 5.18 shows contours of WSS in the $x - y$ centerplane for the no mis-match, small mis-match, and large mis-match cases. Along this plane, peak WSS at 30° rose from $5.64 \text{ N}/\text{m}^2$ in the no mis-match case to $5.91 \text{ N}/\text{m}^2$ in the large mis-match case, an increase of 4.75%. The small mis-match case did not show a significant deviation in WSS from the no mis-match case. There was also no change in WSS along the wall closest to the bifurcation on the side of the left iliac, for either the small or large mis-match cases.

Figures 5.19 and 5.20 show contours of WSS and vorticity, respectively, in the stent inlet plane for the mis-match simulations. The small and large mis-match cases lowered maximum WSS at 30° from $1.18 \text{ N}/\text{m}^2$ in the no mis-match case to $1.15 \text{ N}/\text{m}^2$ and $1.13 \text{ N}/\text{m}^2$, respectively, corresponding to change of 3.25% and 4.50%. Maximum streamwise vorticity in the stent inlet plane increased from 5.09 s^{-1} in the no mis-match case to 5.78 s^{-1} in the small mis-match case (an increase of 13.67%) and 6.20 s^{-1} in the large

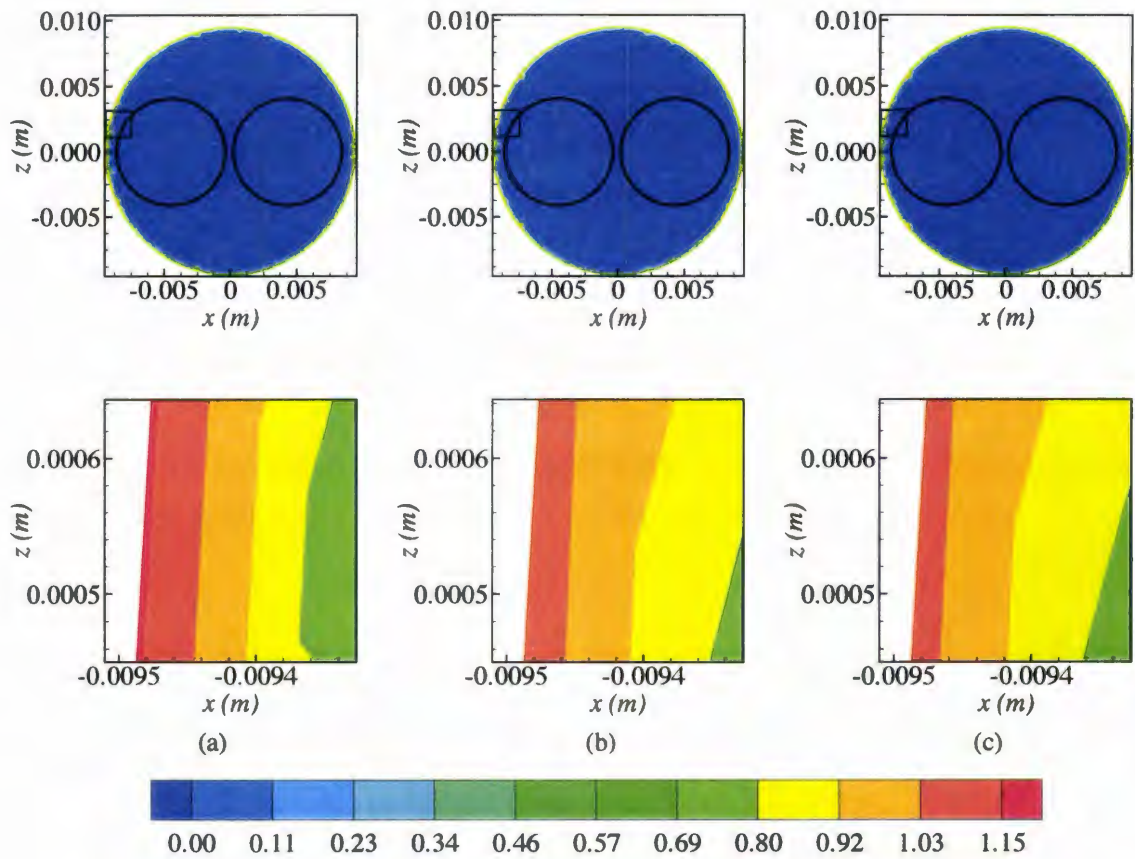


Figure 5.19 Contours of WSS (N/m^2) in the stent inlet plane ($y = -30.5$ mm) at 30° , for (a) no mis-match, (b) small mis-match, and (c) large mis-match.

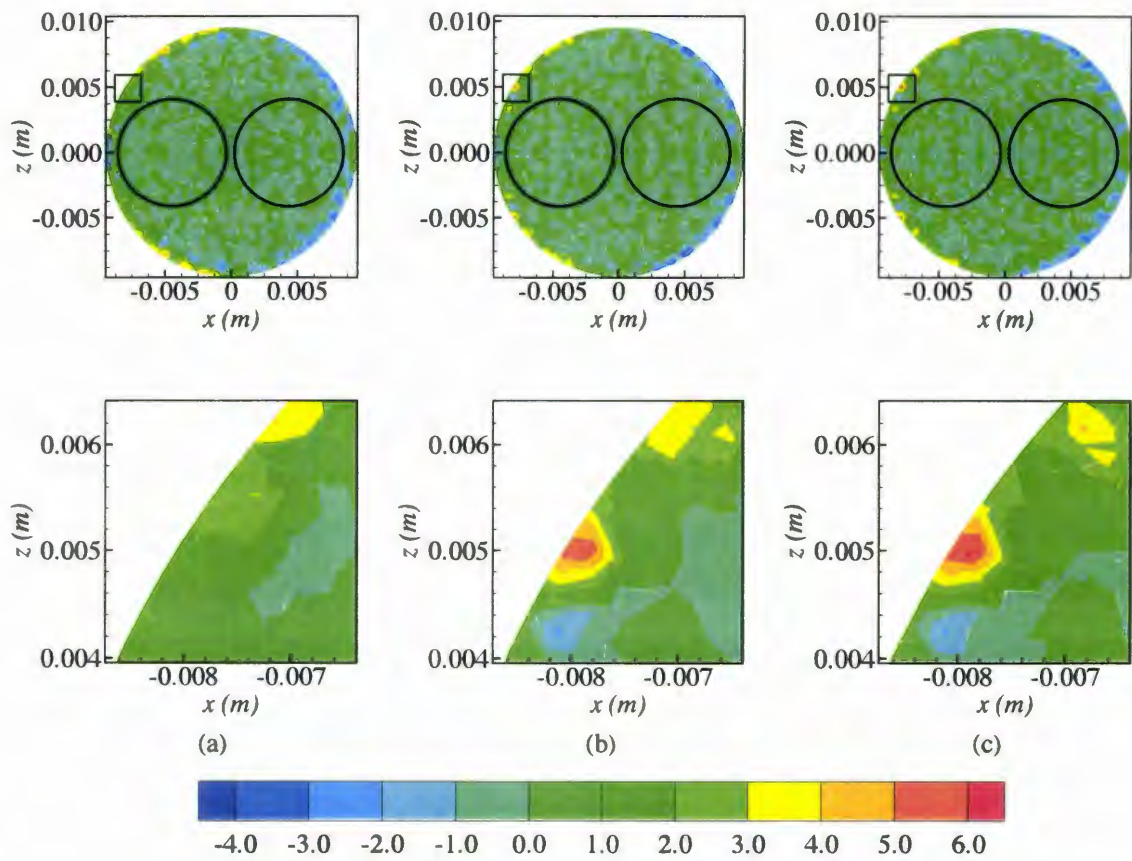


Figure 5.20 Contours of streamwise vorticity (s^{-1}) in the stent inlet plane ($y = -30.5$ mm) at 30° , for (a) no mis-match, (b) small mis-match, and (c) large mis-match.

mis-match case (an increase of 21.91%). In the stent outlet plane, the small and large mis-match cases lowered maximum WSS at 30° from 3.34 N/m² in the no mis-match case to 3.16 N/m² and 3.19 N/m², respectively, corresponding to changes of 5.39% and 4.49%. These changes were most likely due to the stent outlets being further downstream in the mis-matched cases than in the aligned case; in the unstented case, maximum WSS in cross-sectional planes of the iliacs decreased as the flow proceeded deeper into the iliacs. Unlike the data at the stent outlets, the data at the stent inlets were all acquired from the same plane location. Therefore, the deviations in maximum WSS and streamwise vorticity in the stent inlet plane ($y = -30.5$ mm) must be due to the level of stent mis-match.

5.4.4 Effects of low-permeability stents

The final stent reconstruction simulation featured the same geometry as the two-stent case, but with the permeability (α) of the stent walls lowered to 10^{-9} m². Recall that the original two-stent case had stent walls with $\alpha = 10^{-8}$ m². It is worthwhile to note that an actual stent with $\alpha = 10^{-9}$ m² would have extremely dense fiber spacing. It is unlikely that such a stent would ever be used in a real-world surgical treatment. Rather, the low-permeability simulation was conducted for comparative purposes to validate that the original stent with the higher permeability was representing realistic fluid mechanics.

Figure 5.21 compares velocity streamlines near the bifurcation wall between two-stent simulations with $\alpha = 10^{-8}$ m² (high permeability) and $\alpha = 10^{-9}$ m² (low permeability). The region of aortic dead space was greatly increased in the low permeability case. This result demonstrates that the fluid mechanics of the stented system were behaving realistically. A less permeable stent, represented by the case where $\alpha = 10^{-9}$ m², should have denser fiber spacing and should allow for less fluid to pass through the stent wall. Streamlines through a less permeable stent should therefore follow trajectories that

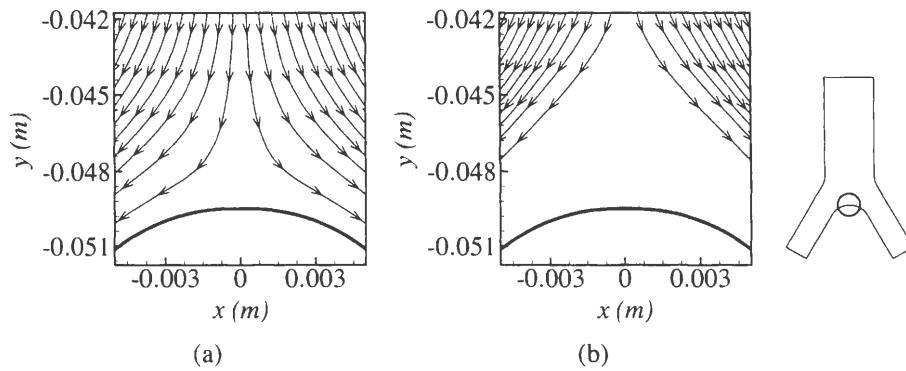


Figure 5.21 Velocity streamlines near the bifurcation wall for (a) two stents, $\alpha = 10^{-8} \text{ m}^2$, and (b) two stents, $\alpha = 10^{-9} \text{ m}^2$.

conform to the curvature of the stent, which is exactly the case shown in Fig. 5.21b.

Figure 5.22 shows contours of spanwise vorticity in the $x - y$ centerplane for the high and low permeability cases at 30° . The maximum vorticity in this plane decreased from 714 s^{-1} in the high-permeability case to 654 s^{-1} in the low-permeability case. However, the region of maximum vorticity extended much further along the inner left iliac wall in the low-permeability case. The inner right iliac wall showed a similar result.

The results shown in Figs. 5.21 and 5.22 demonstrate that utilizing stents with larger fiber spacing (lower permeability) produced flow phenomena more similar to the unstented case. These results are in agreement with the findings of Robaina et al. [43], who suggested that larger fiber spacings promote flow that is more similar to the physiological norm. The contours of Fig. 5.22 also support the findings of Berry et al. [41], who demonstrated that large fiber spacings produce continuous regions of flow separation along stented artery walls.

As a general summary, the low-permeability stent magnified the fluid mechanical disturbances introduced by the high-permeability stent. For example, in the plane of the stent inlets at 30° , the high-permeability stent increased maximum streamwise vorticity by 7.6% in comparison the unstented case; the low-permeability stent increased maximum streamwise vorticity by 55.9%. Table 5.3 lists the magnitudes of and changes

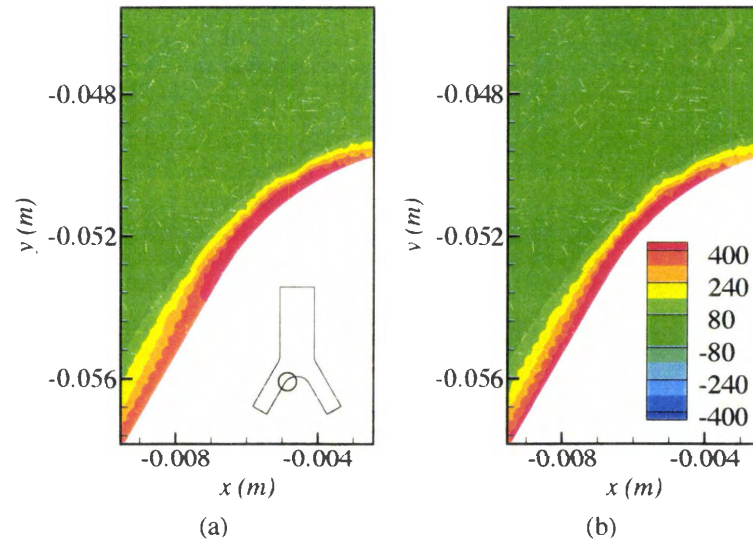


Figure 5.22 Contours of spanwise vorticity (s^{-1}) in the $x - y$ centerplane near the left bifurcation wall for (a) two stents, $\alpha = 10^{-8} \text{ m}^2$, and (b) two stents, $\alpha = 10^{-9} \text{ m}^2$. Pulse phase = 30° .

in WSS, spanwise vorticity, and streamwise vorticity for the unstented, one-stent, two-stent, and low-permeability simulations. These magnifications in changes introduced by the low-permeability stents lend support to the conclusion that the small changes in flow phenomena introduced by the more permeable stents were in fact due to the stent presence.

Table 5.3 Summary of peak WSS, spanwise vorticity, streamwise vorticity, and changes in these variables for unstented, one-stent, two-stent, and low-permeability simulations at a pulse phase of 30° and in the stent inlet plane, stent outlet plane, and the $x - y$ centerplane. Percent changes are in relation to the unstented case.

WSS (N/m²)	No stents	One stent	Two stents	Low perm.
Stent inlet	1.18	1.18 (0.51%)	1.18 (0.47%)	1.30 (10.05%)
Stent outlet	3.34	3.34 (-0.10%)	3.34 (-0.11%)	3.31 (-0.96%)
$x - y$ center	5.70	5.70 (-0.02%)	5.64 (-0.95%)	6.07 (6.57%)
ω_y (s⁻¹)	No stents	1 stent	2 stents	Low perm.
Stent inlet	-487	-487 (-0.08%)	-486 (-0.24%)	-470 (-3.52%)
Stent outlet	-1263	-1265 (0.10%)	-1265 (0.10%)	-1278 (1.18%)
$x - y$ center	727	727 (-0.01%)	713 (-1.80%)	654 (-9.95%)
ω_z (s⁻¹)	No stents	1 stent	2 stents	Low perm.
Stent inlet	4.88	4.90 (0.48%)	5.09 (4.27%)	7.61 (55.91%)
Stent outlet	5.25	5.11 (-2.63%)	5.11 (-2.65%)	4.26 (-18.90%)
$x - y$ center	-19.7	-19.4 (-1.73%)	-19.4 (-1.73%)	-24.4 (23.60%)

CHAPTER 6 CONCLUSIONS, IMPACT, LIMITATIONS, AND FUTURE WORK

The present research consisted of two major investigations using computational fluid dynamics to simulate the hemodynamics of arterial systems. In the first investigation, numerical simulations of flow in an intracranial side-wall aneurysm were performed. The resulting velocity vectors and vorticity contours compared very favorably with data from *in vitro* microPIV experiments on an equivalently-sized aneurysm geometry. However, there was evidence to suggest that the elastic walls present in the microPIV experiments and absent from the numerical simulations played a role in sustaining primary vortex development within the aneurysm, particularly during pulse phases of high velocity.

In the second investigation, numerical simulations of stent reconstruction of an aortic bifurcation were performed. The geometry consisted of the aorta and its two iliac branches. The effects of stent presence, stent alignment, and stent permeability were investigated. Stent presence lowered wall shear stress along stent artery walls and elevated streamwise vorticity near the stent inlets and outlets. When reconstruction featured two mis-aligned stents (stent inlets were not in the same plane in the aorta), wall shear stress decreased and streamwise vorticity increased, proportional to the degree of mis-alignment. Low permeability stents had the general effect of magnifying the flow abnormalities seen in the stent presence simulations.

6.1 Conclusions and Impact

Three major conclusions can be drawn from the results of the aneurysm and stent reconstruction simulations. First, the CFD simulations appeared to be capable of representing real blood flow in the cardiovascular system. The results of the aneurysm simulations matched very closely with the microPIV experiments that they were based upon. The aneurysm and stent reconstruction simulations also demonstrated many of the same flow phenomena seen in earlier *in vitro* and *in vivo* research on similar geometries. The impact of these results, perhaps in the distant rather than the near future, lies in the realm of predictive medicine. Doctors today have limited means of determining if patients who undergo surgeries such as ESO and stenting will encounter post-operative complications. With continued progress in computational power, biomedical imaging, and successful numerical methods, patient-specific numerical models will be able to predict the outcomes of surgeries by simulating post-operative conditions before actually performing the surgery. These models will ultimately lead to higher surgical success rates and improved quality of life for people with cardiovascular disease. The present research provides a basis for future efforts in this direction. Numerical simulations can also provide data for variables that can be difficult to capture *in vivo* or *in vitro*, such as pressure and wall shear, that will lead to a greater understanding of blood flow in the cardiovascular system.

Second, the method of representing the stent geometries with porous jump boundary conditions was successful in producing realistic fluid mechanics within the stented arteries. This method is a novel technique that has not been previously documented in numerical simulations of stent reconstruction. It provides a means of representing stent geometry (and realistic hemodynamics within the geometry) without the often tedious process of modeling each individual stent fiber. It should be noted, however, that the stent model in this research is not capable of capturing flow phenomena around individ-

ual stent fibers. If detailed flow fields very near the wall of a stented artery are desired, an alternative model will be needed.

Third, the level of stent alignment and the stent permeability play a dominant role in the fluid mechanics of two-stented aorta-iliac bifurcations. Both the large (5 mm) mismatch case and the low-permeability case produced significant deviations from the flow phenomena seen in the unstented case. Any biomedical implant, such as a stent, that greatly alters the physiological conditions within the body will be treated as an invader by the immune system, and will fail. Therefore, it is concluded from this research that to achieve optimal flow conditions in two-stent reconstruction of the aorta-iliac bifurcation, the stent protrusions should be matched as closely as possible, and the stent fiber spacing should be as large as possible. Further simulations considering a wider range of mismatches and permeabilities could test the validity of these conclusions.

6.2 Limitations and Future Work

The greatest limitation of the aneurysm simulations was the use of water as a working fluid. Water, rather than blood, was selected in order to match the fluid used in the microPIV experiments and allowed the simulations to closely match the experimental results. In order to more realistically model physiological blood flow, future simulations should consider using a working fluid representative of blood rather than water.

The stent reconstruction simulations were also limited by the simplicity of the working fluid. Blood was modeled as a single-phase fluid. In reality blood is a multi-phase fluid consisting of plasma and numerous types of cells in suspension. Preliminary stent reconstruction simulations modeled blood as a two-phase fluid consisting of 60% plasma and 40% red blood cells by volume. The resulting velocity field displayed subtle but significant differences in the iliac arteries in comparison to the single-phase simulations. Ultimately, the simulations were unable to model blood as a multi-phase fluid due to the

increased computational cost required; multi-phase simulations needed twice the CPU time and data storage of single-phase simulations. Future research efforts in stent reconstruction would be wise to consider a more realistic multi-phase model for blood, rather than the simplified single-phase model. Such work would require greater computational resources than those available for the present research.

Another limitation of the stent reconstruction simulations was the use of a plug velocity profile at the aorta inlet. Fully-developed velocity profiles in FLUENT require user-defined functions that specify the velocity as a function of both space and time. Although the spatial equations for fully-developed pipe flow were readily available, the transient profiles shown in Figs. 4.1 and 5.1 were not well-represented by polynomial functions. FLUENT also allows for the input of custom boundary conditions in tabular form. Efforts were made to create a transient paraboloid inlet profile using this method. Specifying the velocity at all inlet coordinates for all 500 time steps of one complete pulse cycle required a prohibitively large number of data points, and failing to update the inlet velocity at every time step introduced longer periods of the reversed flow discussed in Section 5.1. In light of these complications, a simple plug profile was specified at the aorta inlet. While blood flow in the aorta may not be entirely fully developed, it is most certainly not plug flow. Future simulations could be made more realistic by attempting to represent the transient profiles of Figs. 4.1 and 5.1 with more complex equations.

The stent reconstruction simulations were also limited by the specified pulse rate, which was set at 60 beats per minute for all simulations. A rate this low is probably not representative of people who suffer from cardiovascular diseases. Future simulations should consider using higher pulse rates and investigating how the systems' flow phenomena change.

Finally, both the aneurysm and stent reconstruction simulations were limited by the CPU time required to reach convergence. *In vitro* experiments of pulsatile blood flow often run hundreds of pulse cycles or time-average many pulse cycles in an effort to

reduce transient effects. While the aneurysm simulations were run for five pulse cycles before collecting data, the stent reconstruction simulations were only able to include data from the initial pulse cycle. Running one complete stent reconstruction pulse cycle required roughly two days of real time and approached the limit of CPU time allowed for single jobs on the Xeon cluster. Future research should consider running simulations for a larger number of pulse cycles to determine if a quasi-steady solution can be achieved.

APPENDIX A THE ALGEBRAIC MULTIGRID

FLUENT uses a multigrid scheme to accelerate the convergence of the solver by computing corrections on a series of coarse grid levels. This scheme can greatly reduce the iterations and CPU time required to reach convergence, particularly in models with large numbers of cells.

A.1 The Basic Multigrid Concept

Consider the set of discretized (or linearized) equations given by Eq. A.1:

$$A\phi_e + b = 0 \tag{A.1}$$

where ϕ_e is the exact solution. Before the solution has converged, there will be a defect d associated with the approximate solution ϕ :

$$A\phi + b = d \tag{A.2}$$

The solution seeks a correction ψ such that the exact solution is given by:

$$\phi_e = \phi + \psi \tag{A.3}$$

Substituting Eq. A.3 into Eq. A.1 gives:

$$A\psi + (A\phi + b) = 0 \tag{A.4}$$

Substituting Eq. A.2 into Eq. A.4:

$$A\psi + d = 0 \tag{A.5}$$

Equation A.5 gives the correction in terms of the original fine level operator A and the defect d . Assuming the local (high-frequency) errors have been sufficiently damped by the relaxation scheme on the fine level, the correction ψ will be smooth and therefore more effectively solved on the next coarser level.

A.2 Restriction and Prolongation

Solving for corrections on the coarse level requires transferring the defect down from the fine level (restriction), computing corrections, and then transferring the corrections back up from the coarse level (prolongation). The equation for coarse level corrections ψ^H is:

$$A^H \psi^H + R d = 0 \quad (\text{A.6})$$

where A^H is the coarse level operator and R is the restriction operator responsible for transferring the fine level defect down to the coarse level. The solution of Eq. A.6 is followed by an update to the fine level solution given by:

$$\phi^{new} = \phi + P \psi^H \quad (\text{A.7})$$

where P is the prolongation operator used to transfer the coarse level corrections up to the fine level.

A.3 Unstructured Multigrid

The primary difficulty with using multigrid schemes on unstructured grids is the creation and use of the coarse grid hierarchy. On a structured grid, the coarse grids can be formed simply by removing every other grid line from the fine grid. Prolongation and restriction operators are subsequently simple to formulate. FLUENT overcomes the difficulties of applying multigrid schemes on unstructured grids with an algebraic multigrid (AMG) scheme.

The AMG algorithm is referred to as an “algebraic” multigrid scheme because it generates coarse level equations without the use of any geometry of re-discretization on the coarse levels, a feature that makes AMG useful for calculations on unstructured meshes. The advantage of using AMG is that no coarse grids have to be constructed and stores, and no fluxes or source terms have to be evaluated on the coarse levels.

A.3.1 AMG restriction and prolongation operators

The restriction and prolongation operators used in AMG are based on the additive correction (AC) strategy described for structured grids by Hutchinson and Raithby [66]. Inter-level transfer is accomplished by piecewise constant interpolation and prolongation. The defect in any coarse level cell is given by the sum of defects from the fine level cell it contains, while fine level corrections are obtained by injection of coarse level values. In this manner, the prolongation operator is given by the transpose of the restriction operator:

$$P = R^T \tag{A.8}$$

The restriction operator is defined by a coarsening (or grouping) of fine-level cells into coarse-level cells. Each fine-level cell is grouped with one or more of its “strongest” neighbor cells, with a preference given to currently ungrouped neighbor cells. The algorithm attempts to collect cells into groups of fixed size, typically two or four, but any number of cells can be specified. In the context of grouping, “strongest” refers to the neighbor cell j of the current cell i for which the coefficient A_{ij} is largest. For sets of coupled equations, A_{ij} is a block matrix and the measure of its magnitude is taken to be the magnitude of its first element. In addition, the set of coupled equations for a given cell are treated together, and not divided between different coarse cells, to give the same coarsening for each equation in the system.

A.3.2 AMG coarse level operator

The coarse-level operator A^H is constructed using a Galerkin approach and requires that the defect associated with the corrected fine-level solution vanishes when transferred back to the coarse level:

$$Rd^{new} = 0 \quad (\text{A.9})$$

Upon substituting Eqs. A.2 and A.7 for d^{new} and ϕ^{new} :

$$R \left[A \left(\phi + P\psi^H \right) + b \right] = 0 \quad (\text{A.10})$$

Rearranging Eq. A.10 and substituting Eq. A.2 again:

$$RAP\psi^H + Rd = 0 \quad (\text{A.11})$$

Comparing of Eq. A.11 with Eq. A.6 gives the following expression for the coarse level operator:

$$A^H = RAP \quad (\text{A.12})$$

The construction of coarse level operators thus reduces to a summation of diagonal and corresponding off-diagonal blocks for all fine level cells within a group to form the diagonal block of that group's coarse cell.

A.3.3 Residual reduction rate criteria

The AMG procedure invokes calculations on the next coarser grid level when the error reduction rate on the current level is insufficient, as defined by:

$$R_i > \beta R_{i-1} \quad (\text{A.13})$$

Here R_i is the absolute sum of residuals computed on the current grid level after the i th relaxation on this level. If the residual present in the iteration solution after i relaxations is greater than a fraction β (between 0 and 1) of the residual present after

the $(i-1)$ relaxation, the next coarser grid level should be visited. Thus β is referred to as the residual reduction tolerance. It determines when to move from one grid to the next. The value of β therefore determines the frequency at which coarser grid levels are visited. FLUENT's default β is 0.7. A larger β will result in less frequent visits, and a smaller β will result in more frequent visits.

A.3.4 Termination criteria

Provided that the residual reduction rate is sufficiently rapid, the correction equations will converge on the current grid level and the result will be applied to the next finer grid level.

The correction equations on the current grid level are considered sufficiently converged when the error in the correction solution is reduced a fraction α (between 0 and 1) of the original error on this grid level:

$$R_i < \alpha R_0 \tag{A.14}$$

Here R_i is the residual on the current grid level after the i th iteration on this level, and R_0 is the residual initially obtained on this grid level at the current global iteration. The parameter α , referred to as the termination criterion, has a default value of 0.1. Equation A.14 is also used to terminate calculations on the finest grid level during multigrid procedures. Thus, relaxations are continued on each grid level (including the finest grid level) until the criterion of Eq. A.14 is met, or until a maximum number of relaxations has been completed.

APPENDIX B MICROPIV EXPERIMENTS OF ANEURYSM FLOW

The data collected in this research's simulations of flow in an intra-cranial side-wall aneurysm of the carotid artery were compared to data from an *in vitro* experiment on flow of an aneurysm of equivalent size. This chapter details the microscopic particle image velocimetry (microPIV) system used to acquire the experimental data.

B.1 Introduction to MicroPIV

MicroPIV is a recently-developed method of studying fluid flow on the microscale. Briefly, flow in a microsystem is kept objective over an inverted epi-fluorescent. Light from a laser enters a microscope from behind and is expanded and focused on a small region of the flow. Images of the flow are then taken with a CCD camera. The working fluid contains small tracer particles that are illuminated by the laser light. When the CCD camera takes two pictures in close temporal proximity, the instantaneous velocity of the fluid local to a tracer particle can be calculated based on tracer particle positions.

Next the experimental setups of the microPIV system, including the circulatory system, test section, and camera system, are described. Additional details on the microPIV system and its use in an experimental model of aneurysm flow can be found in Saurabh Pande's M.S. thesis [67].

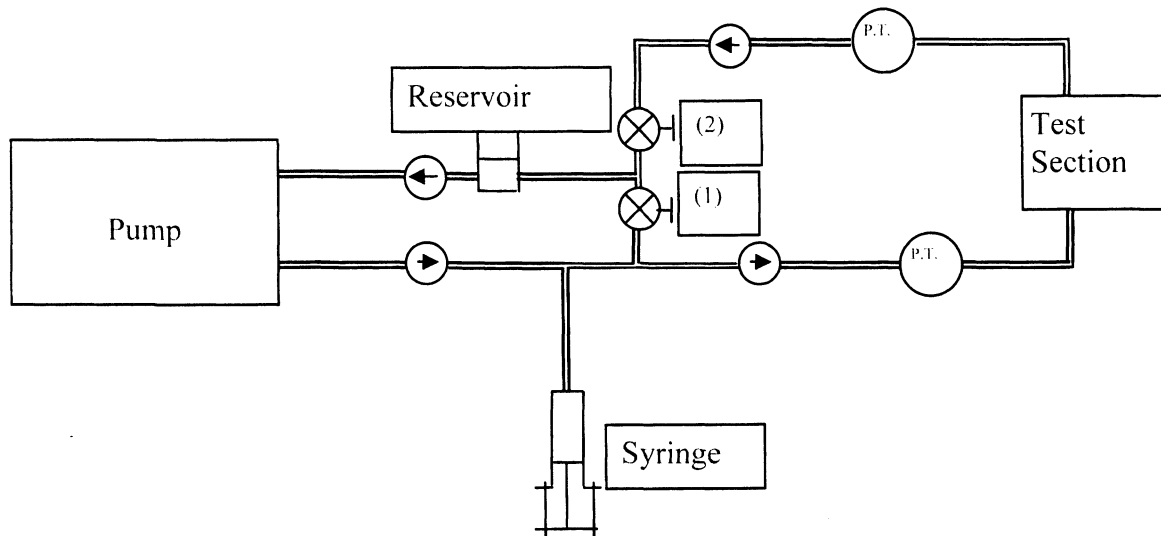


Figure B.1 Schematic of the *in vitro* circulatory system for the microPIV experiments.

B.2 Experimental Setup

B.2.1 Circulatory system

Experiments were performed for flow in an actual-sized flexible-wall model of a human carotid artery with a side-wall aneurysm. The artery diameter was approximately 5 mm and the aneurysm diameter varied between 7 and 8 mm. A pumping device supplied approximately the same pressure waveform found in an actual aneurysm. The u -velocity waveform approximately 10 mm upstream of the aneurysm sac was given in Fig. 4.1. The reciprocating pump consisted of 3 elements: an actuator, an electronic control module, and a command system. The pump was connected to a closed loop of tubes and valves that modeled the circulatory system near a carotid artery. The loop consisted of two parallel flow circuits. The first circuit contained the aneurysm test section, and the second circuit acted as a bypass that added flow control to modulate the waveform within the test section. Figure B.1 shows a schematic of the experimental circulatory system [67]. Figure B.2 shows the experimental test section containing the aneurysm.

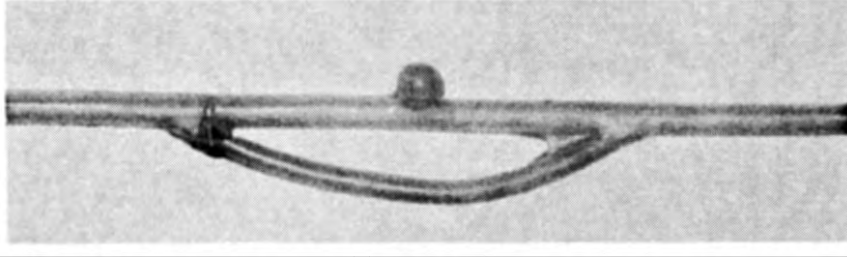


Figure B.2 Experimental test section and aneurysm for the microPIV experiments.

B.2.2 Working fluid

The working fluid used in the experiments was a mixture of deionized water and $7\text{-}\mu\text{m}$ tracing particles with a mixture concentration of 3.12 particles per mL of water. At such low particle concentrations, the volume fraction of particles in the water was less than 2% and the working fluid could be considered a single-phase Newtonian fluid.

B.2.3 MicroPIV camera system

The microPIV camera system is shown in Fig. B.3. The aneurysm model was immersed in a water/glycerin mixture in a clear-bottomed container to reduce refraction. The container was placed on the stage of an inverted microscope (Nikon model T-300 Inverted Microscope). Light from a laser (New Wave Research Gemini Nd:YAG PIV laser) was expanded before entering the microscope through an aperture in the back. The laser light was then directed towards the aneurysm by a dichroic mirror and passed through a microscopic objective that illuminated the tracer particles.

The laser was capable of producing up to 120 mJ per laser pulse, however less than 3 mJ per pulse was needed for the microPIV experiments. An optical attenuator was used to reduce the laser energy to approximately 3 mJ per pulse.

The tracer particles were excited by the laser light and emitted light at a peak excitation wavelength of 612 nm. A beamsplitter ensured that only the emitted particle light reached the CCD camera. Two images per realization were captured and analyzed

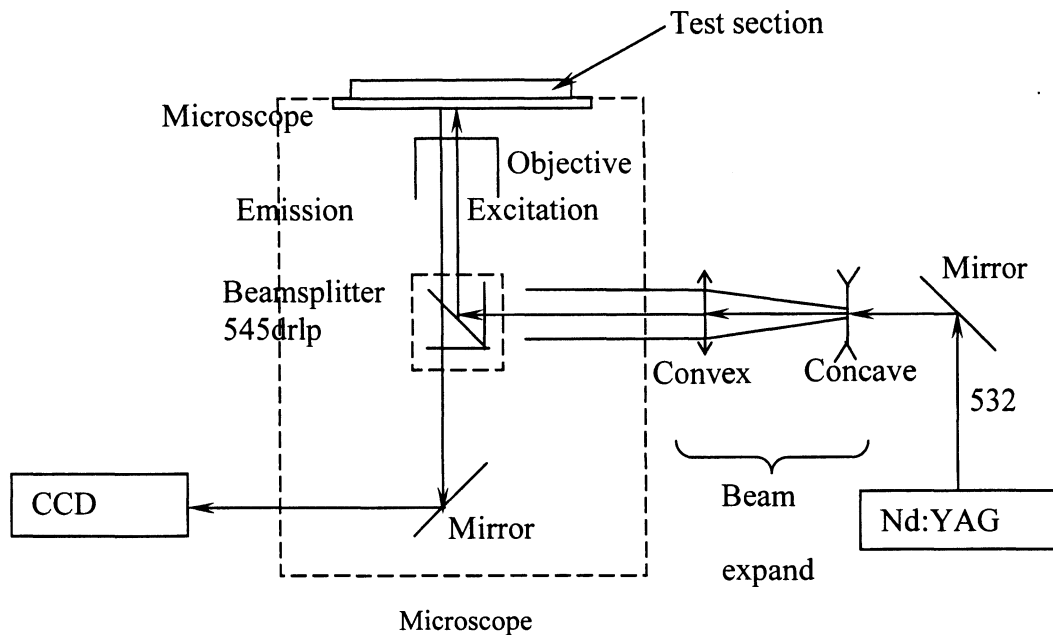


Figure B.3 Schematic of the laser and optics for the microPIV system.

using a cross-correlation technique to produce instantaneous velocity fields. The camera was a Flowmaster 3S PIV Camera (LaVision, Inc.) with a resolution of 1280 x 1024 pixels square and pixel size of $6.7 \times 6.7 \mu\text{m}^2$.

The microPIV measurement depth, or depth of correlation, can be determined using an equation derived by Olsen and Adrian [68]:

$$Z_{corr} = \left[\frac{1 - \sqrt{\epsilon}}{\sqrt{\epsilon}} \left(f\#^2 d_p^2 + \frac{5.95 (M + 1)^2 \lambda^2 f\#^4}{M^2} \right) \right]^{1/2} \quad (\text{B.1})$$

where $\epsilon = 0.01$, $f\#$ is the focal number of the lens, d_p is the tracer particle diameter, M is the magnification, and λ is the wavelength of light emitted by the tracer particles. An alternative equation for Z_{corr} derived by Meinhart, Werely, and Gray [69] yields a similar result. In the microPIV experiments, a 20X 0.45 NA objective was used and yielded a depth of correlation $Z_{corr} = 8.3 \mu\text{m}$. The interrogation windows measured 0.0565 mm^2 . Adjacent interrogation windows overlapped by 50% for a spatial resolution of 0.119 mm and allowed for 34 vectors to be measured across the width of the microchannel.

Achieving this resolution required a volumetric particle concentration of 0.0567%.

The timing between laser pulses was set so that the particles moved approximately one quarter of an interrogation window between pulses. Since the interrogation windows measured 64 camera pixels square, particles moved approximately 16 pixels between pulses. The particle image size projected onto the CCD sensor was approximately 4 pixels. Assuming that the measured velocity was accurate to within a tenth of a particle image diameter, the experimental uncertainty in the microPIV setup was less than 2.5%.

REFERENCES

- [1] American Heart Association (n.d.). *Cardiovascular disease statistics*. Retrieved March 29, 2005, from <http://www.americanheart.org/presenter.jhtml?identifier=4478>
- [2] Reyes R, Carreira JM, Gude F, Gorriz E, Gallardo L, Pardo MD, & Hermida M (2004). Long-term follow-up of iliac wallstents. *CardioVascular and Interventional Radiology*, *27*(6), 624–631.
- [3] Becquemin JP, Allaire E, Qvarfordt P, Desgranges P, Kobeiter H, & Melliere D (1999). Surgical transluminal iliac angioplasty with selective stenting: long-term results assessed by means of duplex stenting. *Journal of Vascular Surgery*, *29*(3), 422–429.
- [4] Toogood GJ, Torrie EP, Magee TR, & Galland RB (1998). Early experiences with stenting for iliac occlusive disease. *European Journal of Vascular and Endovascular Surgery*, *15*(2), 165–168.
- [5] Sutton CS, Tominaga R, Harasaki H, Emoto H, Oku T, Kambic HE, Skibinski C, Beck G, & Hollman J (1990). Vascular stenting in normal and atherosclerotic rabbits. Studies of the intravascular endoprosthesis of titanium-nickel-alloy. *Circulation*, *81*(2), 667–683.

- [6] Kuntz RE, Safian RD, Levine MJ, Reis GJ, Diver DJ, & Baim DS (1992). Novel approach to the analysis of restenosis after the use of three new coronary devices. *Journal of the American College of Cardiology*, 19(7), 1493–1499.
- [7] Foley JB, Penn IM, Brown RI, Murray-Parsons N, White J, Galligan L, & MacDonald C (1993). Safety, success, and restenosis after elective coronary implantation of the Palmaz-Schatz stent in 100 patients at a single center. *American Heart Journal*, 125(3), 686–694.
- [8] Erbel R, Haude M, Hopp HW, Franzen D, Rupprecht HJ, Heublein B, Fischer K, de Jaegere P, Serruys P, Rutsch W, & Probst P (1998). Coronary-artery stenting compared with balloon angioplasty for restenosis after initial balloon angioplasty. *The New England Journal of Medicine*, 339(23), 1672–1678.
- [9] Ellis SG, Bajzer CT, Bhatt DL, Brener SJ, Whitlow PL, Lincoff AM, Moliterno DJ, Raymond RE, Tuzcu EM, Franco I, Dushman-Ellis S, Lander KJ, Schneider JP, & Topol EJ (2004). Real-world bare metal stenting: identification of patients at low or very low risk of 9-month coronary revascularization. *Catheterization and Cardiovascular Interventions*, 63(2), 135–140.
- [10] Raisuke I, Yuji I, Akiyoshi M, Hiroyoshi N, & Kazuhiro H (2004). Predictors of restenosis after implantation of 2.5 mm stents in small coronary arteries. *Circulation Journal*, 68(3), 236–240.
- [11] Pogady P, Mustafa H, Wies W, Lungenschmid K, Wurm G, Tomancok B, Holl K, & Fischer J (1998). Microsurgical management of a complicated aneurysmal endovascular embolisation with GDC coil: a case report. *Neurosurgical Review*, 23(2-3), 206–209.

- [12] Thomas JE, Armonda RA, & Rosenwasser RH (2000). Endosaccular thrombosis of cerebral aneurysms: strategy, indications, and technique. *Neurosurgery Clinics North America*, 11(1), 101–121.
- [13] Luo CB, Wei CJ, Chang FC, Teng MM, Lirng JF, & Chang CY (2003). Stent-assisted embolization of internal carotid artery aneurysms. *Journal of the Chinese Medical Association*, 66(8), 460–466.
- [14] Ahn JY, Chang SS, Lee BH, Kim SH, Yoon PH, Joo JY, & Kim JK (2005). Treatment of spontaneous arterial dissections with stent placement for preservation of the parent artery. *Acta Neurochirurgica*. Published January 13, 2005, retrieved from <http://www.springerlink.com/link.asp?id=lr4l7kwawb4rj21u>
- [15] Ku DN (1997). Blood flow in arteries. *Annual Review in Fluid Mechanics*, 29, 399–434.
- [16] Dutta A & Tarbell JM (1996). Influence of non-Newtonian behavior of blood on flow in an elastic artery model. *Journal of Biomechanical Engineering*, 118(1), 111–119.
- [17] Taylor CA, Cheng CP, Espinosa LA, Tang BT, Parker D, & Herfkens RJ (2002). In vivo quantification of blood flow and wall shear stress in the human abdominal aorta during lower limb exercise. *Annals of Biomedical Engineering*, 30(3), 402–408.
- [18] Bonert M, Leask RL, Butany J, Ethier CR, Myers JG, Johnston KW, & Ojha M (2003). The relationship between wall shear stress distributions and intimal thickening in the human abdominal aorta. *BioMedical Engineering OnLine*. Published November 26, 2003, retrieved from <http://www.biomedical-engineering-online.com/content/2/1/18>.

- [19] Lee D & Chen JY (2002). Numerical simulation of steady flow fields in a model of abdominal aorta with its peripheral branches. *Journal of Biomechanics*, 35(8), 1115–1122.
- [20] Ku DN, Glagov S, Moore JE, & Zarins CK (1989) Flow patterns in the abdominal aorta under simulated postprandial and exercise conditions: an experimental study. *Journal of Vascular Surgery*, 9, 309–316.
- [21] Moore JE, Ku DN, Zarins CK, & Glagov S (1992). Pulsatile flow visualization in the abdominal aorta under differing physiological conditions: implications for increased susceptibility to atherosclerosis. *Journal of Biomechanical Engineering*, 114(3), 391–397.
- [22] Buchanan JR, Kleinstreuer C, & Comer JK (2000). Rheological effects on pulsatile hemodynamics in a stenosed tube. *Computers and Fluids*, 29(6), 695–724.
- [23] Marques PF, Oliveira MC, Franca AS, & Pinotti M (2003). Modeling and simulation of pulsatile blood flow with a physiologic wave pattern. *Artificial Organs*, 27(5), 478–485.
- [24] Henkes H, Fischer S, Weber W, Miloslavski E, Felber S, Brew S, & Kuehne D (2004). Endovascular coil occlusion of 1811 intracranial aneurysms: early angiographic and clinical results. *Neurosurgery*, 54(2), 268–280.
- [25] Kwon OK, Kim SH, Kwon BJ, Kang HS, Kim JH, Oh CW, & Han MH (2005). Endovascular treatment of wide-necked aneurysms by using two micro-catheters: techniques and outcomes in 25 patients. *American Journal of Neuroradiology*, 26(4), 894–900.

- [26] Hans FJ, Moller-Hartmann W, Brunn A, Schmitz-Rode T, Thron A, & Krings T (2005). Treatment of wide-necked aneurysms with balloon-expanded polyurethane stentgrafts: experience in an animal model. *Acta Neurochirurgica*. Published March 17, 2005, retrieved from <http://www.springerlink.com/app/home/contribution.asp?wasp=2bcd951d10a34752ae3ef2a2b299e4d4&referrer=parent&backto=issue,26,61;journal,1,89;linkingpublicationresults,1:102025,1>
- [27] Ohyama T, Nishide T, Iwata H, & Taki W (2004). Development of gold stents for the treatment of intracranial aneurysms: an experimental study in a canine model. *American Journal of Neuroradiology*, *25(1)*, 53-59.
- [28] Lopes D & Sani S (2005). Histological postmortem study of an internal carotid artery aneurysm treated with the Neuroform stent. *Neurosurgery*, *56(2)*, E416.
- [29] Vanninen R, Manninen H, & Ronkainen A (2003). Broad-based intracranial aneurysms: thrombosis induced by stent placement. *American Journal of Neuroradiology*, *24(2)*, 263-266.
- [30] Hademenos GJ & Massoud TF (1997). Biophysical mechanisms of stroke. *Stroke*, *28(10)*, 2067-2077.
- [31] Gobin YP, Counord JL, Flaud P, & Duffaux J (1994). In vitro study of haemodynamics in a giant saccular aneurysm model: influence of flow dynamics in the parent vessel and effects of coil embolisation. *Neuroradiology*, *36(7)*, 530-536.
- [32] Bluestein D, Niu L, Schoephoerster RT, & Dewanjee MK (1996). Steady flow in an aneurysm model: correlation between fluid dynamics and blood platelet deposition. *Journal of Biomechanical Engineering*, *118(3)*, 280-286.

- [33] Fatourae N & Amini AA (2000). Recovery of flow patterns in an abdominal aortic aneurysm from phase contrast MRI. *IEEE Workshop on Mathematical Methods in Biomedical Imaging Analysis*, June 11–12, 2000, Hilton Head, South Carolina.
- [34] Steinman DA, Milner JS, Norley CJ, Lownie SP, & Holdsworth DW (2003). Image-based computational simulation of flow dynamics in a giant intracranial aneurysm. *American Journal of Neuroradiology*, *24*(4), 559–566.
- [35] West NE, Ruygrok PN, Disco CM, Webster MW, Lindeboom WK, O’Neill WW, Mercado NF, & Serruys PW (2004). Clinical and angiographic predictors of restenosis after stent deployment in diabetic patients. *Circulation*, *109*(7), 867–873.
- [36] Mauri L, O’Malley AJ, Cutlip DE, Ho KK, Popma JJ, Chauhan MS, Baim DS, Cohen DJ, & Kuntz RE (2004). Effects of stent length and lesion length on coronary restenosis. *American Journal of Cardiology*, *93*(11), 1340–1346.
- [37] Elezi S, Kastrati H, Neumann FJ, Hadamitzky M, Dirschinger J, & Schomig A (1998). Vessel size and long-term outcome after coronary stent placement. *Circulation*, *98*(18), 1875–1880.
- [38] Moses JW, Leon MB, Popma JJ, Fitzgerald PJ, Holmes DR, O’Shaughnessy C, Caputo PP, Kereiakes DJ, Williams DO, Teirstein PS, Jaeger JL, & Kuntz RE (2003). Sirolimus-eluting stents versus standard stents in patients with stenosis in a native coronary artery. *The New England Journal of Medicine*, *349*(14), 1315–1323.
- [39] Sindermann JR, Verin V, Hopewell JW, Rodemann HP, & Hendry JH (2004). Biological aspects of radiation and drug-eluting stents for the prevention of restenosis. *Cardiovascular Research*, *63*(1), 22–30.
- [40] Berry JL, Moore JE, Newman VS, & Routh WD (1997). In vitro flow visualization in stented arterial segments. *Journal of Vascular Investigation*, *3*(2), 63–68.

- [41] Berry JL, Santamarina A, Moore JE, Roychowdhury S, & Routh WD (2000). Experimental and computational evaluation of coronary stents. *Annals of Biomedical Engineering*, 28(4), 386–398.
- [42] Rogers C & Edelman ER (1995). Endovascular stent design dictates experimental restenosis and thrombosis. *Circulation*, 91(12), 2995–3001.
- [43] Robaina S, Jayachandran B, He Y, Frank A, Moreno MR, Schoepfoerster RT, & Moore JE (2003). Platelet adhesion to simulated stented surfaces. *Journal of Endovascular Therapy*, 10(5), 978–986.
- [44] Walsh PW, Chin-Quee S, & Moore JE (2003). Flow changes in the aorta associated with the deployment of a AAA stent graft. *Medical Engineering and Physics*, 25(4), 299–307.
- [45] Frank AO, Walsh PW, & Moore JE (2002). Computational fluid dynamics and stent design. *Artificial Organs*, 26(7), 614–621.
- [46] Jou LD (2001). Three dimensional simulation of flow over stented vessel. *Proceedings of the 2001 ASME Summer Bioengineering Conference*, June 27–July 1, 2001, Snowbird, Utah.
- [47] Berry JL, Manoach E, Mekkaoui C, Rolland PH, Moore JE, & Rachev A (2002). Hemodynamics and wall mechanics of a compliance matching stent: in vitro and in vivo analysis. *Journal of Vascular Interventional Radiology*, 13(1), 97–105.
- [48] Schachter LG & Barakat AI (2001). Computational study of arterial flow disturbance induced by intravascular stents. *Proceedings of the 2001 ASME Summer Bioengineering Conference*, June 27–July 1, 2001, Snowbird, Utah.

- [49] LaDisa JF, Olson LE, Guler I, Hettrick DA, Audi SH, Kersten JR, Warltier DC, & Pagel PS (2004). Stent design properties and deployment ratio influence indexes of wall shear stress: a three-dimensional computational fluid dynamics investigation within a normal artery. *Journal of Applied Physiology*, *97*(1), 424–430.
- [50] Fluent Incorporated (2001). *GAMBIT 2.0.4 User's Guide*. Fluent Inc., Lebanon, New Hampshire.
- [51] Fluent Incorporated (2003). *FLUENT 6.1 User's Guide*. Fluent Inc., Lebanon, New Hampshire.
- [52] Holmes DG & Connell SG (1989). Solution to the 2D Navier-Stokes equations on unstructured adaptive grids. *AIAA 9th Computational Fluid Dynamics Conference*, June 13–14, 1989, Buffalo, New York.
- [53] Rhie CM & Chow WL (1983). Numerical study of the turbulent flow past an airfoil with trailing edge separation. *AIAA Journal*, *21*(11), 1525–1532.
- [54] Patankar SV (1980). *Numerical Heat Transfer and Fluid Flow*. Washington, District of Columbia: Hemisphere.
- [55] Issa RI (1986). Solution of implicitly discretized fluid flow equations by operator splitting. *Journal of Computational Physics*, *62*, 40–65.
- [56] Celik I, Chen JC, Roache PJ, & Scheurer G (1993). Quantification of uncertainty in computational fluid dynamics. *ASME Fluids Engineering Division Summer Meeting*, June 20–24, 1993, Washington, District of Columbia.
- [57] Celik I & Karatekin O (1997). Numerical experiments on application of Richardson extrapolation on nonuniform grids. *Journal of Fluids Engineering*, *119*(3), 584–590.

- [58] Jackson DW & James DF (1986). The permeability of fibrous porous media. *Canadian Journal of Chemical Engineering*, 64(3), 364–374.
- [59] College-Level Unified Environment, College of Engineering, Iowa State University (n.d.). *Remote access to UNIX*. Retrieved May 13, 2005, from <http://clue.eng.iastate.edu/docs/remote/unix.shtml>
- [60] High Performance Computing Center, Iowa State University (n.d.). *High performance computing facilities for students*. Retrieved May 13, 2005, from <http://andrew.ait.iastate.edu/HPC/hpc-class/background.html>
- [61] Wille SO (1981). Pulsatile pressure and flow in an arterial aneurysm simulated in a mathematical model. *Journal of Biomedical Engineering*, 3(2), 153–158.
- [62] Fukushima T, Matsuzawa T, & Homma T (1989). Visualization and finite element analysis of pulsatile flow in abdominal aortic aneurysm. *Biorheology*, 26(2), 109–130.
- [63] Finol EA & Amon CH (2001). Blood flow in abdominal aortic aneurysms: pulsatile flow hemodynamics. *Journal of Biomechanical Engineering*, 123(5), 474–484.
- [64] Chitanvis SM, Hademenos G, & Powers WJ (1995). Hemodynamic assessment of the development and rupture of intracranial aneurysms using computational simulations. *Neurology Research*, 17(6), 426–434.
- [65] Carlier SG, van Damme LC, Blommerde CP, Wentzel JJ, van Langehove G, Verheyen S, Kockx MM, Knaapen MW, Cheng C, Giljzen F, Duncker DJ, Stergiopoulos N, Slager CJ, Serruys PW, & Krams R (2003). Augmentation of wall shear stress inhibits neointimal hyperplasia after stent implantation: inhibition through reduction of inflammation? *Circulation*, 107(21), 2741–2746.

- [66] Hutchinson BR & Raithby GD (1986). A multigrid method based on the additive correction strategy. *Numerical Heat Transfer*, 9, 511–537.
- [67] Pande S (2004). Study of non-intrusive surgical techniques for cerebral aneurysms. Master's thesis, Iowa State University, Ames, Iowa.
- [68] Olsen MG & Adrian RJ (2000). Out-of-focus effects on particle image visibility and correlation in microscopic particle image velocimetry. *Experiments in Fluids*, 29(7), S166–S174.
- [69] Meinhart CD, Werely ST, & Gray MHB (2000). Volume illumination for two-dimensional particle image velocimetry. *Measurement Science and Technology*, 11(6), 809–814.